

AD-756 080

THEORETICAL STUDIES OF HIGH-POWER
INFRARED WINDOW MATERIALS

Marshall S. Sparks

Xonics, Incorporated

Prepared for:

Defense Supply Service
Advanced Research Projects Agency

December 1972

DISTRIBUTED BY:

NTIS

National Technical Information Service
U. S. DEPARTMENT OF COMMERCE
5285 Port Royal Road, Springfield Va. 22151

(Handwritten signature)

AD756080

THEORETICAL STUDIES OF HIGH-POWER INFRARED WINDOW MATERIALS

M. Sparks, Principal Investigator, (213) 787-7380

Xonics, Incorporated
Van Nuys, California 91406

Final Technical Report
December, 1972

Contract No. DARCS-72-C-0129
Effective Date of Contract: 7 December 1971
Contract Expiration Date: 6 December 1972

DDC
RECEIVED
MAR 6 1973

Prepared for
Defense Supply Service - Washington D. C.

Sponsored by Advanced Research Projects Agency
ARPA Order No. 1967 Program Code No. 2D10

"This research was supported by the Advanced Research Projects Agency of the Department of Defense and was monitored by the Defense Supply Service-Washington D.C. under Contract No. DARCS-72-C-0129. The views and conclusions expressed in this document are those of the authors and should not be interpreted as necessarily representing the official policies, either expressed or implied, of the Advanced Research Projects Agency or the U. S. Government."

Unclassified

Security Classification

DOCUMENT CONTROL DATA - R & D

(Security classification of title, body of abstract and indexing annotation must be entered when the overall report is classified)

1. ORIGINATING ACTIVITY (Corporate author) Xenics, Incorporated 6837 Hayvenhurst Avenue Van Nuys, California 91406		2a. REPORT SECURITY CLASSIFICATION Unclassified	
		2b. GROUP N/A	
3. REPORT TITLE THEORETICAL STUDIES OF HIGH-POWER INFRARED WINDOW MATERIALS			
4. DESCRIPTIVE NOTES (Type of report and inclusive dates) Final Technical Report, 7 December 1971 to 6 December 1972			
5. AUTHOR(S) (First name, middle initial, last name) Marshall S. Sparks			
6. REPORT DATE December 1972		7a. TOTAL NO. OF PAGES 167	7b. NO. OF REFS 46
8a. CONTRACT OR GRANT NO. DAHC15-72-C-0129		9a. ORIGINATOR'S REPORT NUMBER(S)	
b. PROJECT NO.			
c.		9b. OTHER REPORT NO(S) (Any other numbers that may be assigned this report)	
d.			
11. SUPPLEMENTARY NOTES Sponsored by Advanced Research Projects, ARPA No. 1969		12. SPONSORING MILITARY ACTIVITY Defense Supply Service - Washington Room 1D245, The Pentagon Washington, D. C. 20310	
13. ABSTRACT <p>The recently observed exponential frequency dependence of the infrared absorption coefficient β in NaCl- and CaF₂-structure crystals is explained in terms of multiphonon absorption processes. A calculation gives the correct frequency dependence and approximate magnitude of β and predicts the temperature dependence, which should be observable. Use of the central-limit theorem reduces the mathematical complexity of the analysis sufficiently to yield a simple closed-form approximation to β. In the exponential region, the difference processes, in which some thermally excited phonons are annihilated, are negligible with respect to the summation processes. Terms higher than second order in the perturbation expansion are found to be negligible for small n (small number of phonons created). An explanation involving finite phonon lifetimes is proposed to explain the fact that the alkali halides show less structure in the β-ω curves than do the semiconductor crystals. Preliminary results on a new approach, using an anharmonic Einstein model, also exhibit the exponential frequency behavior. In addition, $\beta \sim \omega^{-2}$ is predicted for "square-well" type impurities.</p> <p>Small amounts of macroscopic inclusions in or on the surface of a nonabsorbing host crystal, in some cases a fractional volume of $\sim 10^{-7}$ to 10^{-8}, can give rise to a value of the optical absorption coefficient β of 10^{-4} cm^{-1} (a typical value of current interest). For various types of inclusions, the frequency dependence ranges from increasing as ω^2, to independent of ω, to exponentially decreasing with ω. The temperature dependence ranges from independent of T to increasing as T^p in the high-temperature limit, where $p \approx 2 - 4$ typically. Simple expressions for the absorption cross section are derived for various cases of practical interest. The cross sections are used to derive expressions for β for the four cases of large inclusions of strong and weak absorbers and of small inclusions of dielectric and metallic particles.</p>			

DD FORM 1473
1 NOV 65

1a

Unclassified

Security Classification

14 KEY WORDS	LINK A		LINK B		LINK C	
	ROLE	WT	ROLE	WT	ROLE	WT
High-Power Laser Windows Optical Absorption Coefficient β Multiphonon Absorption Theory <ul style="list-style-type: none">- anharmonic coefficients- dipole-moment expansion- density of states- alkali halides- alkaline earth fluorides Pressure Deformation Optical Absorption by Inclusions <ul style="list-style-type: none">- Mie theory- local heating- local failure- extrinsic absorption coefficient Materials: KBr CaF ₂ InAs KCl CdTe Ge NaCl ZnSe Si LiF GaAs Diamond BaF ₂ AlSb Ba Ti O ₃ SrF ₂ ZnS						
ABSTRACT (Continued) A result of general interest in the theory of scattering is that the absorption cross section of large spheres is equal to $(1 - R_{\perp})\pi a^2$, where R_{\perp} is the reflection coefficient for normal incidence, rather than $(1 - \langle R \rangle)\pi a^2$, where $\langle R \rangle$ is the geometric-optics average reflection over the illuminated hemisphere. Material failure resulting from local heating of macroscopic inclusions is a far greater problem in high-intensity, short-pulse systems than in low-intensity long-pulse or cw systems having equal average intensity. Microsecond pulses with energy densities as low as $\sim 5 \text{ J/cm}^2$ (excluding Bloembergen field enhancement) can cause material failure. Experimental curves of β vs ω , collected from the literature, are presented for a number of materials. Results on multiphonon calculations, the need for emissivity measurements, effects of pressure on the operation of infrared windows, effects of interband and deep-level transitions on infrared absorption, and a discussion of the previously observed T^2 linewidth dependence for NaCl, which were presented in the two previous technical progress reports, are summarized briefly in the Introduction.						

THEORETICAL STUDIES OF HIGH-POWER
INFRARED WINDOW MATERIALS

M. Sparks, Principal Investigator, 213/787-7380

Xonics, Incorporated
Van Nuys, California 91406

Final Technical Report

December, 1972

Contract No. DAHC15-72-C-0129

Effective Date of Contract: 7 December 1971

Contract Expiration Date: 6 December 1972

Prepared for
Defense Supply Service - Washington, D. C.

Sponsored by Advanced Research Projects Agency
ARPA Order No. 1969; Program Code No. 2D10

"This research was supported by the Advanced Research Projects Agency of the Department of Defense and was monitored by the Defense Supply Service-Washington, D. C. under Contract No. DAHC15-72-C-0129. The views and conclusions contained in this document are those of the authors and should not be interpreted as necessarily representing the official policies, either expressed or implied, of the Advanced Research Projects Agency or the U. S. Government."

16
APPROVED FOR PUBLIC RELEASE
DISTRIBUTION UNLIMITED

1 - MAR 1973

TABLE OF CONTENTS

	<u>Page</u>
Preface	vi
Summary	1
A. Introduction	3
B. Theory of Multiphonon Infrared Absorption	7
I. Introduction	8
II. Analysis of Absorption Coefficient β_n	14
III. Closed-Form Approximation to β_2	24
IV. Closed-Form Approximation to β_n	40
V. The Central-Limit Approximation	52
VI. Effect of Confluence Processes on β_n	59
VII. Effects of Terms Other Than $v^{(n+1)}$ in \mathcal{K}_n	64
VIII. Higher-Order Processes In The n-Phonon Region	72
IX. Anharmonic-Einstein-Oscillator Model	87
C. Theory of Infrared Absorption and Material Failure in Crystals Containing Inclusions	90
I. Introduction	91
II. Analysis of Absorption Cross Sections	93
III. Absorption Coefficients for Various Types of Inclusions	102
IV. Examples	108
V. Material Failure From Local Heating	111
VI. Conclusions	129
D. Collection of Experimental Results For $\beta(\omega)$	131
E. References to Previous Multiphonon Calculations	155
References	158

LIST OF ILLUSTRATIONS

<u>Section</u>	<u>Figure</u>	<u>Title</u>	<u>Page</u>
B	1	Comparison of experimental and theoretical results	9
	2	Various n-phonon processes	11
	3	Splitting process and confluence processes	13
	4	Densities of states for LA and LO phonons in NaCl	28
	5	Rough estimate of the relaxation frequency Γ_{2LL} of the fundamental mode decaying into LO and LA modes.	
	6	Approximate dispersion relations and the resulting densities of states $g(\omega)$	32
	7	Relaxation frequency Γ_{2LL} from the spherical-Brillouin-zone approximation	37
	8	Schematic illustration of regions for which the two-phonon-summation process with $\omega = \omega_{LA} + \omega_{LO}$ can conserve energy	39
	9	Debye approximation to the density of states	47
	10	The function $f(\omega)$ and successive convolutions	53
	11	Rectangular function $F(\omega)$ considered as the sum of two equal rectangular functions $F_L(\omega)$ and $F_R(\omega)$	56
	12	Phonon relaxation processes	73
	13	Various time orderings of the process shown in Fig. 12(c)	74
	14	Two-vertex, n-phonon process and (n-1)-vertex, n-phonon process	75
	15	Various time orderings of the process shown in Fig. 14(b) for $n = 4$	76

LIST OF ILLUSTRATIONS (Cont'd)

<u>Section</u>	<u>Figure</u>	<u>Title</u>	<u>Page</u>
C	1	Schematic illustration of a monotonically increasing cross section	100
	2	Example of a cross section with a maximum value greater than πa^2	101
	3	Schematic illustration of the temperature at the center of a uniformly heated spherical inclusion for three limiting values of K_H/K_I	117
	4	Schematic illustration of the temperature at the surface of spherical inclusion with uniform heat generation within skin depth $\delta \ll a$ at the surface	124
D	1	Experimental frequency dependence of the infrared absorption coefficient β for KBr	132
	2	Experimental frequency dependence of the infrared absorption coefficient β for KCl	133
	3	Experimental frequency dependence of the infrared absorption coefficient β for NaCl	134
	4	Experimental frequency dependence of the infrared absorption coefficient β for LiF	135
	5	Experimental frequency dependence of the infrared absorption coefficient β for BaF ₂	136
	6	Experimental frequency dependence of the infrared absorption coefficient β for SrF ₂	137
	7	Experimental frequency dependence of the infrared absorption coefficient β for CaF ₂	138
	8	Experimental frequency dependence of the infrared absorption coefficient β for CdTe	139
	9	Experimental frequency dependence of the infrared absorption coefficient β for ZnSe	140
	10	Experimental frequency dependence of the infrared absorption coefficient β for GaAs	141

LIST OF ILLUSTRATIONS (Cont'd)

<u>Section</u>	<u>Figure</u>	<u>Title</u>	<u>Page</u>
D	11	Experimental frequency dependence of the infrared absorption coefficient β for AlSb	142
	12	Experimental frequency dependence of the infrared absorption coefficient β for ZnS	143
	13	Experimental frequency dependence of the infrared absorption coefficient β for InAs	144
	14	Experimental frequency dependence of the infrared absorption coefficient β for Ge	145
	15	Experimental frequency dependence of the infrared absorption coefficient β for Si	146
	16	Experimental frequency dependence of the infrared absorption coefficient β for diamond	147
	17	Experimental frequency dependence of the infrared absorption coefficient β for Ba Ti O ₃	148
	18	Comparison of the absorption of alkali halides, from Figs. 1-4	149
	19	Comparison of the absorption of the alkaline earth fluorides, from the curves in Figs. 5, 6, and 7	150
	20	Comparison of the absorption of zincblende structure semiconductors, from the curves in Figs. 8-10	151
	21	Comparison of the absorption of zincblende structure semiconductors, from the curves in Figs. 11-13	152
	22	Comparison of the absorption of type IV elemental semiconductors, from the curves in Figs. 14-17	153
	23	Comparison of the absorption of one material from each group represented in Figs. 18-22	154

PREFACE

This Final Technical Report describes the work performed on Contract DAHC15-72-C-0129 on Theoretical Studies of High-Power Infrared Window Materials during the period from July 1, 1972 to November 30, 1972. Two previous technical progress reports were prepared under this contract. Other publications are listed in the Introduction (Sec. A).

The work on Theoretical Studies of High-Power Infrared Window Materials will continue under Contract DAHC15-73-C-0127.

Computer analyses, which have been delayed by the change from 6600 to 7600 computers at the laboratory of Dr. Arnold Karo (consultant from Livermore) are now under way. The results will be presented in a future report.

The following consultants are participating in the program at present: Dr. Arnold M. Karo, Lawrence Livermore Laboratory, Dr. Alexei A. Maradudin, University of California, Irvine, Dr. Douglas L. Mills, University of California, Irvine, and Dr. Lu J. Sham, University of California, San Diego.

SUMMARY

The recently observed exponential frequency dependence of the infrared absorption coefficient β in NaCl- and CaF_2 -structure crystals is explained in terms of multiphonon absorption processes. A calculation gives the correct frequency dependence and approximate magnitude of β and predicts the temperature dependence, which should be observable. Use of the central-limit theorem reduces the mathematical complexity of the analysis sufficiently to yield a simple closed-form approximation to β . In the exponential region, the difference processes, in which some thermally excited phonons are annihilated, are negligible with respect to the summation processes. Terms higher than second order in the perturbation expansion are found to be negligible for small n (small number of phonons created). An explanation involving finite phonon lifetimes is proposed to explain the fact that the alkali halides show less structure in the β - ω curves than do the semiconductor crystals. Preliminary results on a new approach, using an anharmonic Einstein model, also exhibit the exponential frequency behavior. In addition, $\beta \sim \omega^{-2}$ is predicted for "square-well" type impurities.

Small amounts of macroscopic inclusions in or on the surface of a non-absorbing host crystal, in some cases a fractional volume of $\sim 10^{-7}$ to 10^{-8} , can give rise to a value of the optical absorption coefficient β of 10^{-4} cm^{-1} (a typical value of current interest). For various types of inclusions, the frequency dependence ranges from increasing as ω^2 , to independent of ω , to exponentially decreasing with ω . The temperature dependence ranges from

independent of T to increasing as T^p in the high-temperature limit, where $p \cong 2-4$ typically. Simple expressions for the absorption cross section are derived for various cases of practical interest. The cross sections are used to derive expressions for β for the four cases of large inclusions of strong and weak absorbers and of small inclusions of dielectric and metallic particles.

A result of general interest in the theory of scattering is that the absorption cross section of large spheres is equal to $(1 - R_{\perp})\pi a^2$, where R_{\perp} is the reflection coefficient for normal incidence, rather than $(1 - \langle R \rangle)\pi a^2$, where $\langle R \rangle$ is the geometric-optics average reflection over the illuminated hemisphere. Material failure resulting from local heating of macroscopic inclusions is a far greater problem in high-intensity, short-pulse systems than in low-intensity long-pulse or cw systems having equal average intensity. Microsecond pulses with energy densities as low as $\sim 5 \text{ J/cm}^2$ (excluding Bloembergen field enhancement) can cause material failure.

Experimental curves of β vs ω , collected from the literature, are presented for a number of materials. Results on multiphonon calculations, the need for emissivity measurements, effects of pressure on the operation of infrared windows, effects of interband and deep-level transitions on infrared absorption, and a discussion of the previously observed T^2 linewidth dependence for NaCl, which were presented in the two previous technical progress reports, are summarized briefly in the Introduction.

A. INTRODUCTION

In the first technical progress report¹ the program was outlined, the problems and objectives were defined, and the relevance to other Department of Defense programs was discussed. A highly simplified discussion of the theory of infrared absorption was given as an introduction for investigators in related fields. Preliminary calculations of the values of the absorption coefficient β for the two-phonon and the general n-phonon summation intrinsic processes provided an overview of the theoretical problem and established the method of calculation and the types of approximations necessary to render the mathematics tractable. Methods of estimating the values of the anharmonic coefficients, the higher-order terms in the dipole-moment expansion, and the joint densities of states were established. The exponential decay of β as a function of frequency was explained in terms of multiphonon absorption processes. It was suggested that two-phonon summation processes in materials having the NaCl structure are small unless one phonon is optical and the other is acoustical. The latter result afforded a tentative explanation of the previously observed T^2 dependence of the resonance linewidth of NaCl and the small number of two-phonon summation peaks in various alkali halides.

It was pointed out that currently known transmission and calorimetric measurements cannot be used to obtain values of β in a crucial range of frequencies, and that emissivity measurements should be capable of providing the needed values of β in the full range of interest. Pursuit of such experimental programs would contribute substantially to the information presently needed for Department of Defense laser programs. Two effects of pressure on the operation

of windows were considered. First, the deformation resulting from a static pressure differential between the two faces of the window can distort the laser beam or fracture the window. Second, the window-material figures of merit for thermally induced optical distortion that were previously developed are changed when the thickness required to withstand the pressure is taken into consideration.

It was pointed out that several references on inter-valence-band transitions and transitions involving deep levels in the band gap for semiconductor materials suggested that at impurity concentrations so low that the usual free-carrier absorption is not detectable, transitions of holes between two different valence bands apparently can give rise to broad absorption bands that can be strong ($\beta = 0.3 \text{ cm}^{-1}$ in one case,² for example) in the $2\text{-}6\mu\text{m}$ region. Transitions of electrons between different regions of the conduction band where the densities of states are high also should give rise to observable values of β .

In the second technical progress report,³ the results of a Green's function analysis and additional ordinary perturbation-theory analyses of the n-phonon summation process were presented. A detailed analysis of the multiphonon absorption was presented and applied to several alkali halides. It was suggested that a possible explanation of the fact that the $\beta - \omega$ curves of the alkali halides and alkaline-earth fluorides show less structure than those of the semiconductor materials is that the greater anharmonicity of the NaCl-structure crystals could give rise to such short lifetimes of the zone-boundary phonons that the peaks are broadened to the point of essentially complete overlap.

The contributions to the n-phonon absorption coefficient β_n from higher-order processes with n phonons in the final state were calculated for a number of processes and classes of processes. Terms containing self-energy diagrams within the final-state- or fundamental-phonon lines simply renormalize the phonons. Diagrams having one intermediate phonon and one 3-phonon vertex give the leading contributions to β of the higher-order processes considered. In NaCl at 300 K, the contributions to β_3 from the higher-order process was an order of magnitude smaller than that of the single-vertex contribution. It was also shown that higher-order processes will dominate the single-vertex diagram at some larger value of n. A complete report of pressure-induced optical distortion and the effects of pressure on the figures of merit of candidate materials was given.

In the present report, new results on the multiphonon infrared absorption are reported (Sec. B), a theory of infrared absorption by macroscopic inclusions in crystals is presented (Sec. C), experimental curves of β vs ω , collected from the literature, are included (Sec. D), and a list of references to previous multiphonon calculations is given in Sec. E.

In addition to this final technical report, the following publications and conference presentations were prepared under the contract:

Sec. A

M. Sparks, "Recent Developments in High-Power Infrared Window Research," 4th ASTM Damage in Laser Materials Symposium, Boulder, Colorado, June 14-15, 1972.

M. Sparks and M. Cottis, "Pressure-Induced Optical Distortion in Infrared Windows," Conference on High Power Infrared Laser Window Materials, Hyannis, Massachusetts, Oct. 30-Nov. 1, 1972; proceedings to be published by Air Force Cambridge Research Laboratories, Cambridge, Massachusetts.

M. Sparks and L. J. Sham, "Theory of Multiphonon Infrared Absorption," Conference on High Power Infrared Laser Window Materials, Hyannis, Massachusetts, Oct. 30-Nov. 1, 1972; proceedings to be published by Air Force Cambridge Research Laboratories, Cambridge, Massachusetts.

M. Sparks and M. Cottis, "Pressure-Induced Optical Distortion in Laser Windows," to be published J. Appl. Phys. January 1973.

M. Sparks and L. J. Sham, "Exponential Frequency Dependence of Multiphonon-Summaion Infrared Absorption," Solid State Commun. 11, 1451 (1972).

M. Sparks, "Theory of Infrared Absorption by Macroscopic Inclusion in Crystals," to be published.

A. Karo, M. Sparks, and L. J. Sham, "Numerical Analysis of Infrared Multiphonon Absorption," in preparation.

Section letters, which are displayed at the top of each page, are not displayed in equation numbers, figure numbers, and table numbers. Important results are denoted by underscored equation numbers.

B. THEORY OF MULTIPHONON INFRARED ABSORPTION

The recently observed exponential frequency dependence of the infrared absorption coefficient β in NaCl- and CaF_2 -structure crystals is explained in terms of multiphonon absorption processes. A calculation gives the correct frequency dependence and approximate magnitude of β and predicts the temperature dependence, which should be observable. In the exponential region, the difference processes, in which some thermally excited phonons are annihilated, are negligible with respect to the summation processes. The higher-order terms in the perturbation expansion are negligible for small n (small number of phonons created). An explanation involving finite phonon lifetimes is proposed to explain the fact that the alkali halides show less structure in the β - ω curves than do the semiconductor crystals. Use of the central-limit theorem reduces the mathematical complexity of the analysis sufficiently to yield a simple closed-form approximation to β . Previously obtained results that were given in the two preceding reports were outlined briefly in Sec. A.

I. Introduction

The availability of high-power infrared lasers has stimulated renewed interest in infrared absorption. The intensity I of infrared radiation propagating through a solid typically decays according to the Beer law, $I = I_0 \exp(-\beta z)$, where β is the optical absorption coefficient. Materials with very small values of β , say $\beta \leq 10^{-4} \text{ cm}^{-1}$, are needed in high-power infrared laser systems for such transparent optical components as windows. Prior to the availability of high-power lasers, there was considerable interest in relating the positions of the multiphonon peaks, chiefly in the two-phonon-summation region^{3a} (where $\beta \gg 1 \text{ cm}^{-1}$), to the phonon dispersion relations. Current interest is in the higher-order phonon regions where $\beta \ll 1 \text{ cm}^{-1}$ and in the numerical value of β , not simply the positions of the multiphonon peaks.

An interesting recent result^{2,4} is the observation of optical absorption coefficients that vary exponentially with frequency

$$\beta \sim \exp(-A\omega) \quad (1.1)$$

for $\beta \lesssim 10 \text{ cm}^{-1}$ in LiF, NaCl, KCl, KBr, MgF_2 , CaF_2 , BaF_2 , SrF_2 , Al_2O_3 , and BaTiO_3 . For example, β decreases exponentially with frequency for over four orders of magnitude change in the value of β for NaCl as ω/ω_f increases from 2.2 to 5.8, where ω_f is the fundamental-mode frequency (i. e., the frequency of the transverse optical phonon with $k \cong 0$). See the points and crosses in Fig. 1.

The exponential behavior naturally suggests the form $\beta \sim \exp(-\hbar\omega/k_B T)$, where ω is the photon frequency and the other symbols have their standard meanings. However, the room-temperature values of A in (1.1) differ by

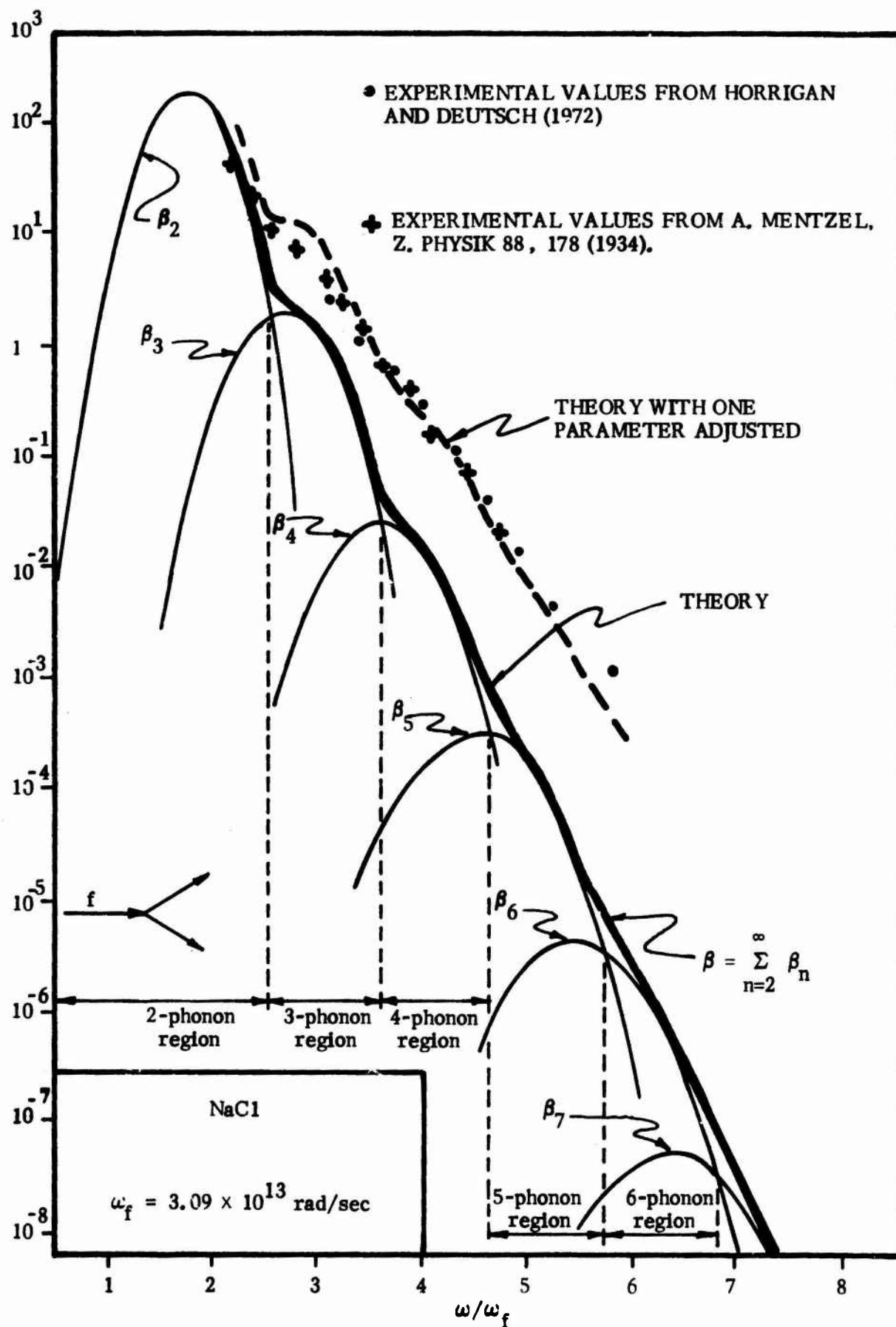


Fig. 1. Comparison of experimental and theoretical results.

factors of $\sim 2-4$ from the value of $\hbar/300k_B$. Furthermore, the temperature dependence of β ,⁵ although not well established at present, apparently is less strong than $\exp(-\hbar\omega/k_B T)$.

Of the many intrinsic and extrinsic sources of absorption, the simple n-phonon summation contributions to β give rise to a frequency dependence of β that is very nearly exponential over a large range of β , including the experimental range. In the n-phonon summation process, shown in Fig. 2(a), a photon is annihilated, a virtual fundamental phonon is created, the fundamental phonon is annihilated, and n phonons are created. Classically, the electromagnetic field drives the fundamental mode (off resonance, in general), whose relaxation frequency is determined by the process of splitting into n other lattice-vibrational modes.

By energy conservation, $\hbar\omega$ is equal to the sum of the energies of the n final-state phonons. Thus, the n-phonon summation process cannot contribute to β when ω is greater than n times the greatest phonon frequency ω_{top} . Furthermore, for $\omega \ll n\omega_{\text{top}}$, the contribution β_n of the n-phonon summation process to β is small because energy conservation forces the wavevectors of the final-state phonons to be small, and the factors k^2 in the densities of states are small. Thus, β_n has a peak at a frequency below $n\omega_{\text{top}}$. As n increases, the peak shifts to higher frequencies and decreases in magnitude (since the higher-order processes contribute less to the value of β). This behavior of the β_n is illustrated by the light curves in Fig. 1 and is discussed in detail in Sec. IV. The heavy curve, which is the sum of the individual β_n , shows the near-exponential behavior of β .

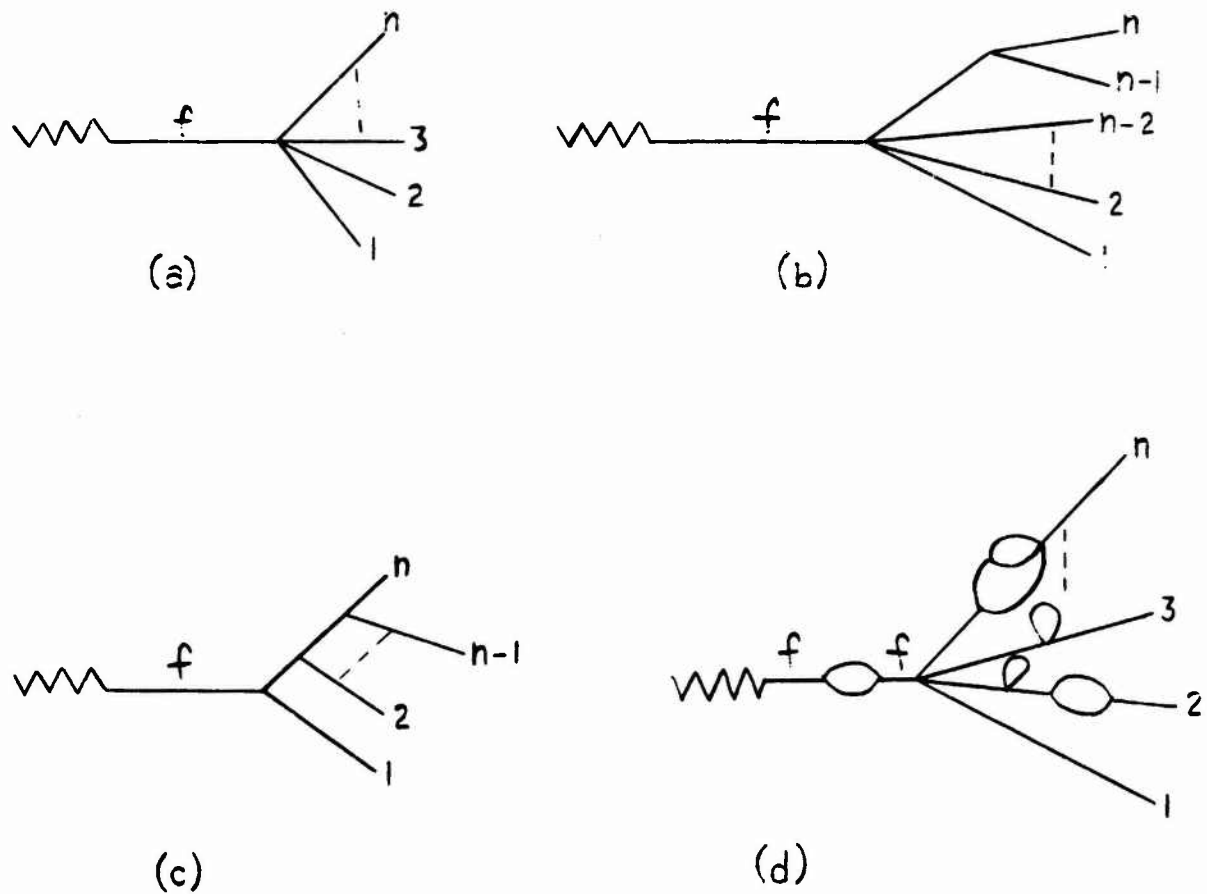


Fig. 2. Various n -phonon processes: (a) single-vertex process; (b) two-vertex process; (c) $(n-1)$ -vertex process; (d) process with self-energy contributions to several phonons. Wavy lines are photons and straight lines are phonons.

It will be shown (Sec. VI) that for $\omega \gtrsim \omega_{\text{top}}$ at room temperature, the contribution to β from the confluence processes (Fig. 3b and c) is negligible with respect to that from the splitting process (Fig. 3a). Assumptions and approximations made in the analysis are discussed in Sec. II.

In Sec. II, a general expression for the n^{th} order absorption coefficient β_n is derived. In Sec. III this expression is evaluated approximately for $n = 2$ to obtain a closed-form approximation for β_2 resulting from the splitting of the fundamental phonon into one longitudinal optical and one longitudinal acoustical mode. In Sec. IV, the central-limit theorem is used to reduce the problem of evaluating a multiple integral over phonon coordinates $Q_1 \cdots Q_n$ to that of evaluating integrals over a single phonon coordinate Q . Further approximations are made in order to obtain numerical values for β_n . In Sec. V the central-limit approximation is discussed. In Sec. VI the effect of the confluence processes on β is shown to be negligible. In Sec. VII, the effect of terms other than the $(n+1)$ -order interaction $V^{(n+1)}$ and \mathcal{H}_n are discussed. In Sec. VIII, terms higher than second order in the perturbation expansion are shown to be negligible for small n . Preliminary results of applying the Liouville equation for the classical distribution function of an array of anharmonic Einstein oscillators to the infrared absorption problem are given in Sec. IX.

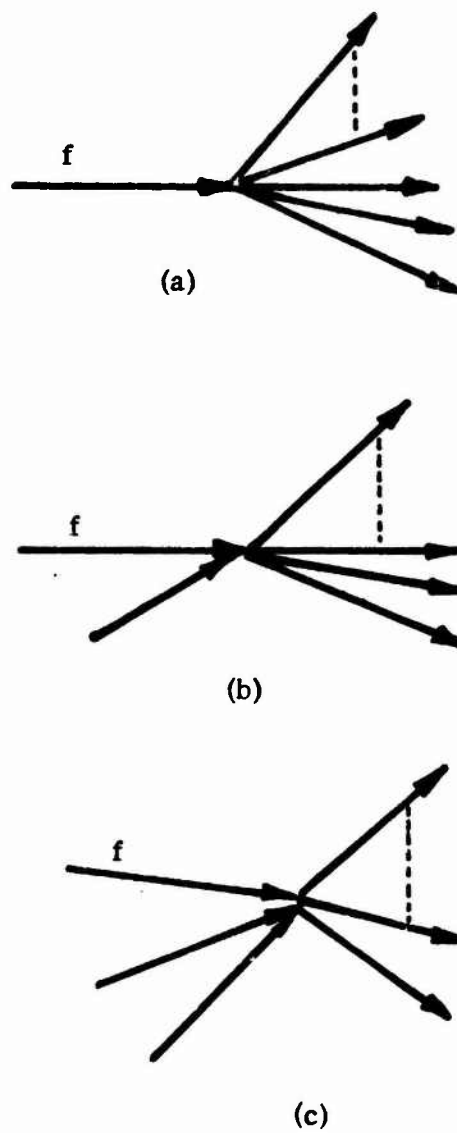


Fig. 3. Splitting process (a) and confluence processes (b) and (c).

II. Analysis of Absorption Coefficient β_n

Consider the anharmonic-potential induced n -phonon summation process (Fig. 2a). It is not difficult to show, by a Green's function analysis of the dielectric constant for example, that the value β_n of β in the n -phonon region for materials with the NaCl or ZnS structure is ⁵ [with $2\Gamma(qjj', \Omega)$ in Cowley's notation written as Γ_n]

$$\beta_n = \frac{4\pi N e^{*2}}{c m_r n_r \Omega} \frac{\omega \omega_f \Gamma_n}{(\omega^2 - \omega_f^2)^2 + (\omega_f \Gamma_n)^2}, \quad (2.1)$$

where N is the number of unit cells, Ω is the volume of the crystal, e^* is the Born effective charge, c is the velocity of light, m_r is the reduced mass of the two ion types, n_r is the index of refraction, ω_f is the fundamental mode frequency, and Γ_n is the energy relaxation frequency of the fundamental mode. The real part of the self energy is not included in (2.1) as it is not of interest here; the experimentally determined phonon frequencies will be used.

In the analysis of Γ_n , the following assumptions and approximations are made:

- 1) Standard second-order perturbation theory is used.
- 2) The anharmonic-potential interaction, and not the Lax-Burstein-Born higher-order-moment mechanism,⁷ is considered.
- 3) In the anharmonic interaction, only the short-range repulsive force of nearest neighbors is included.
- 4) The central-force approximation is made.

5) Only NaCl-structure materials are considered. Materials having the cubic ZnS structure will be considered in a future report.

6) The finite lifetimes of the interacting phonons are neglected except in plausibility arguments concerning the sharpness of multiphonon absorption peaks.

7) The central-limit theorem is used to reduce the multiple sum over phonon coordinates $Q_1 \cdots Q_n$ to single sums over the coordinates Q of one phonon. In the present analysis, considerable care is required in applying this approximation, as discussed in Secs. V and VI.

8) In Secs. III and IV, approximations to the density of phonon states $g(\omega)$, the occupation numbers n_Q , and certain angle factors U are made.

The value of Γ_n can be calculated from the standard perturbation-theory expression for the n -Boson-summation relaxation frequency⁸

$$\Gamma_n = \frac{2\pi}{\hbar^2} n! \sum_{Q_1 \cdots Q_n} \left| V_{f, Q_1 \cdots Q_n} \right|^2 \Delta(\underline{K}_n) \delta(\tilde{\omega}_n) \tilde{n}_n, \quad (2.2)$$

where $\underline{K}_n \equiv \underline{k}_1 + \underline{k}_2 + \cdots + \underline{k}_n + \underline{K}_j$, \underline{k}_i is the wavevector of the i^{th} phonon, \underline{K}_j is a reciprocal lattice vector, Δ is the Kronecker delta, $\tilde{\omega}_n \equiv \omega - \omega_{Q_1} - \cdots - \omega_{Q_n}$, Q_i is defined as the set of numbers \underline{k}_i and b_i , where b_i is the branch of the dispersion relation, $\tilde{n}_n = (n_1+1)(n_2+1) \cdots (n_n+1) / (n_\omega+1)$, $n_i \equiv n(Q_i) = [\exp(\omega_{Q_i}/\omega_T) - 1]^{-1}$, $n_\omega = [\exp(\omega/\omega_T) - 1]^{-1}$, $\omega_T \equiv k_B T / \hbar = 3.928 \times 10^{13}$ rad/sec at 300 K, and the V 's are the coefficients in the scattering Hamiltonian

$$\mathcal{H}_n = \sum_{Q_1 \cdots Q_n} V_{f, Q_1 \cdots Q_n} \Delta(\underline{K}) a_f a_{Q_1}^\dagger \cdots a_{Q_n}^\dagger + \text{cc} . \quad (2.3)$$

In (2.3), f denotes the fundamental mode, cc denotes hermitian conjugate, and the a^\dagger and a are phonon creation and annihilation operators normalized to unit commutators.

For the Hamiltonian, up to n^{th} order phonon processes, take the central-force potential

$$\mathcal{H} = \frac{1}{(n+1)!} V^{(n+1)} \sum_{\ell=1}^N \sum_{m=1}^{N-1} (R_{\ell m} - \delta_{\ell m})^{n+1} + \sum_{p=2}^n \frac{1}{p!} V^{(p)} \sum_{\ell m} (R_{\ell m} - \delta_{\ell m})^p, \quad (2.4)$$

where $R_{\ell m}$ is the length of the vector from ion m to ion ℓ , $V^{(n+1)} \equiv d^{(n+1)}V(R_{\ell m})/dR_{\ell m}^{(n+1)}$ evaluated at equilibrium ($R_{\ell m} = \delta_{\ell m}$), ℓ labels the cell (lighter ions, for example) and m labels the neighboring ions. No factor of $1/2$ to avoid double counting is needed for this labeling. The vector amplitude $R_{\ell m}$, whose equilibrium value is $\delta_{\ell m}$, can be expanded in terms of displacements \underline{u}_ℓ and \underline{u}_m as

$$R_{\ell m} \equiv |\underline{R}_\ell - \underline{R}_m| = |\underline{R}_{\ell 0} - \underline{R}_{m0} + \underline{u}_\ell - \underline{u}_m| \equiv |\underline{\delta}_{\ell m} + \underline{u}_{\ell m}|,$$

where $\underline{R}_{\ell 0}$ and \underline{R}_{m0} are the equilibrium values of the positions \underline{R}_ℓ and \underline{R}_m of the ℓ^{th} and m^{th} ions and

$$\underline{\delta}_{\ell m} \equiv \underline{\delta}_m \equiv \underline{R}_{\ell 0} - \underline{R}_{m0},$$

$$\underline{u}_i \equiv \underline{u}(\underline{R}_{i0}), \quad i = \ell, m, \quad \underline{u}_{\ell m} \equiv \underline{u}_\ell - \underline{u}_m.$$

The amplitude $R_{\ell m}$ can be written as

$$\begin{aligned} R_{\ell m} &= [(\underline{\delta}_m + \underline{u}_{\ell m}) \cdot (\underline{\delta}_m + \underline{u}_{\ell m})]^{1/2} \\ &= \delta_m + \hat{\delta}_m \cdot \underline{u}_{\ell m} + \dots \end{aligned} \quad (2.5)$$

Thus

$$R_{\ell m} - \delta_m = \hat{\delta}_m \cdot \underline{u}_{\ell m} + \dots \quad (2.6)$$

Dropping the $p = 1 \dots n$ terms in (2.4) and the higher-order terms in (2.6) and substituting (2.6) into (2.4) gives

$$\mathcal{K}_n = \frac{1}{(n+1)!} V^{(n+1)} \sum_{\ell m} (\hat{\delta}_m \cdot \underline{u}_{\ell m})^{n+1} \quad (2.7)$$

When all terms from (2.4) and (2.6) are retained, the angle factor $\hat{\delta}_m \cdot \underline{u}_{\ell m}$ in (2.7) [and α_n in (2.16)] is changed, as discussed in Sec. VII.

The usual expansion of the displacement is⁹

$$\underline{u}_\tau(\underline{R}_{i0}) = \sum_Q \left(\frac{\hbar}{2Nm_\tau \omega_Q} \right)^{1/2} \underline{u}_{\tau Q} A_Q e^{i\mathbf{k} \cdot \underline{R}_{i0}}, \quad (2.8)$$

where

$$A_Q \equiv A_{\underline{k}b} = a_{\underline{k}b} + a_{-\underline{k}b}^\dagger$$

and $\tau = 1$ or 2 denotes the type of ion (Na or Cl, for example). The polarization vectors $\underline{u}_{\tau Q}$ obey the orthonormalization relations

$$\sum_\tau \underline{u}_{\tau kb}^* \cdot \underline{u}_{\tau kb'} = \delta_{bb'} \quad (2.9a)$$

$$\sum_b (\underline{u}_{\tau Q}^* \cdot \hat{\mathbf{x}}_i) (\underline{u}_{\tau' Q} \cdot \hat{\mathbf{x}}_j) = \delta_{ij} \delta_{\tau\tau'}, \quad (2.9b)$$

where $\hat{\mathbf{x}}_i$ is a unit vector along a unit-cube axis. These are simply the orthonormality relations for the rows and columns of the six-by-six diagonalizing

matrix (for the eigenfrequency problem) whose columns are the six vectors $(\underline{u}_{>Q}, \underline{u}_{<Q})$, where $\tau = >$ and $\tau = <$ denote the greater and lesser masses, respectively.

In Ref. 9, (2.8) was written [with $\kappa \equiv \tau$, $j \equiv b$, $(b, k) \equiv Q$, and $\underline{u}(\ell\kappa) \equiv \underline{u}_\tau(\underline{R}_{\ell 0})$] as

$$\underline{u}_\tau(\underline{R}_{\ell 0}) = \sum_Q \left(\frac{\hbar}{2Nm_\tau\omega_Q} \right)^{1/2} \underline{e}(\tau | \underline{k}b) A_Q e^{i\underline{k} \cdot \underline{R}_{\ell 0}}.$$

In this expression, the equilibrium ion position $\underline{R}_{\ell 0}$ appears in the exponent, in contrast to (2.8) where $\underline{R}_{i0} = \underline{R}_{\ell 0} + \underline{B}_i$ (with \underline{B}_i as one of the two basis vectors specifying the ion positions in a cell) appears in the exponent. The relation between these two expressions is

$$\underline{u}_{\tau Q} = \underline{e}(\tau | \underline{k}b), \quad \text{for small mass,}$$

$$\underline{u}_{\tau Q} = \underline{e}(\tau | \underline{k}b) e^{i\underline{k} \cdot \underline{B}}, \quad \text{for large mass,}$$

where it is assumed that the small masses are at the lattice sites ($\underline{B}_1 = 0$) and the large masses have $\underline{B}_2 \equiv \underline{B} = a_{nn}(\hat{x} + \hat{y} + \hat{z})$ for the NaCl structure. Here $\hat{}$ denotes a unit vector and a_{nn} is the near neighbor equilibrium spacing.

For the fundamental mode

$$\underline{u}_{\tau f} = (-1)^\tau \left(\frac{m_r}{m_\tau} \right)^{1/2} \hat{u}_f, \quad (2.10a)$$

where m_r is the reduced mass ($m_r^{-1} \equiv m_{<}^{-1} + m_{>}^{-1}$). In the limit $kL \ll 1$, where L is of the order of the unit cell length,

$$\tilde{u}_{\tau kb} = (-1)^\tau \left(\frac{m_r}{m_\tau} \right)^{1/2} \hat{u}_{\tau kb}, \quad (\text{optical}) \quad (2.10b)$$

$$\tilde{u}_{\tau kb} = \left(\frac{m_\tau}{m_< + m_>} \right)^{1/2} \hat{u}_{\tau kb}, \quad (\text{acoustical}) \quad (2.10c)$$

Notice that (2.10a) and (2.8) with $A_f \neq 0$ and all other $A_Q = 0$ (only fundamental phonons present) give the well known relations¹⁰

$$\tilde{u}_\tau(\tilde{R}_i) - \tilde{u}_\tau(\tilde{R}_i + \tilde{\delta}_m) \sim 1/\sqrt{m_r}$$

$$u_\tau(\tilde{R}_i)/u_{\tau'}(\tilde{R}_i + \tilde{\delta}_m) \sim -m_{\tau'}/m_\tau$$

for $\tau \neq \tau'$.

Substituting (2.8)-(2.10a) into (2.7) and using

$$\sum_{\ell=1}^N \exp[i(\tilde{k}_1 + \dots + \tilde{k}_n) \cdot \tilde{R}_{\ell 0}] = N \Delta(\tilde{K}_r)$$

and

$$\begin{aligned} \tilde{u}_{\ell m} &\equiv \tilde{u}_\ell - \tilde{u}_m \equiv \tilde{u}_{<}(\tilde{R}_\ell) - \tilde{u}_{>}(\tilde{R}_{\ell 0} + \tilde{\delta}_m) \\ &= \sum_Q \left(\frac{\hbar}{2Nm_<\omega_Q} \right)^{1/2} \tilde{U}_m(Q) A_Q e^{i\tilde{k} \cdot \tilde{R}_{\ell 0}}, \end{aligned}$$

where

$$\tilde{U}_m(Q) = \tilde{u}_{<Q} - \sqrt{\frac{m_<}{m_>}} \tilde{u}_{>Q} e^{i\tilde{k} \cdot \tilde{\delta}_m}, \quad (2.11)$$

gives (2.3) with

$$V_{fQ_1 \cdots Q_n} = \frac{\left(\frac{1}{2}\hbar\right)^{\frac{1}{2}(n+1)} V^{(n+1)}_{(n+1)}}{(n+1)! N^{\frac{1}{2}(n-1)}} \frac{1}{(m_r \omega)^{1/2}} \frac{1}{m_{<}^{n/2}} \frac{1}{(\omega_{Q_1} \cdots \omega_{Q_n})^{1/2}} \\ \times \sum_m (\hat{\delta}_m \cdot \hat{u}_f) U_m(Q_1) \cdots U_m(Q_n), \quad (2.12)$$

where $U_m(Q) \equiv \hat{\delta}_m \cdot \underline{U}_m(Q)$. In general,

$$\hat{\delta}_m \cdot \underline{U}_m(Q) \equiv U_{m'}(Q), \quad U_m(Q) \equiv U_m(Q) \quad (2.12a)$$

The factor $(n+1)$ in (2.12) arises from the $n+1$ ways of choosing a_f from the A_{Q_i} in (2.7) and (2.8). Note that for the fundamental mode, (2.11) and (2.10a) give

$$\underline{U}_m(f) = \left(\frac{m_{<}}{m_r} \right)^{1/2} \hat{u}_f. \quad (2.12b)$$

The following model potential¹⁰ is used: $V = E \exp(-R_{\ell m}/\rho a_{nn})$ for nearest neighbors and zero otherwise. Here a_{nn} is the equilibrium near-neighbor distance. The Coulomb potential is added to this repulsive potential in order to determine the values of ρ and of $E = 3 \exp(1/\rho) B a_{nn}^3 \rho^2 / (1 - 2\rho)$, where B is the bulk modulus, but is not included in the anharmonic potential. This is a reasonable approximation for $2 \leq n \leq 20$, since the higher-order derivatives of the rapidly varying repulsive potential are much greater than those of the slowly varying Coulomb potential. This is easily seen for a repulsive potential $\sim 1/R_{ij}^{10}$ and a Coulomb potential $\sim 1/R_{ij}$, for which the n^{th} derivatives contain factors of magnitude $(2)(3) \cdots (n+1)$ and $(10)(11) \cdots (n+9)$, respectively.

The value of $V^{(n+1)}$ for this model potential is

$$V^{(n+1)} = \pm \frac{3B a_{nn}^2 \rho}{(1-2\rho)} \frac{1}{a_{nn}^n \rho^n} . \quad (2.13)$$

From (2.12b)

$$U_m(f) = (m_{<}/m_r)^{1/2} \hat{\delta}_m \cdot \hat{u}_f . \quad (2.14)$$

Substituting (2.13) and (2.14) into (2.12) gives

$$V_{fQ_1 \dots Q_n} = \pm \frac{3\rho}{(1-2\rho)} \alpha_n \frac{B a_{nn}^3}{n! N^{\frac{1}{2}} (n-1)} \frac{1}{(\omega_{Q_1} \dots \omega_{Q_n})^{1/2}} \\ \times \left(\frac{\hbar}{2 m_r \omega a_{nn}^2} \right)^{1/2} \left[\frac{\hbar}{2 \rho^2 m_{<} a_{nn}^2} \right]^{n/2} , \quad (2.15)$$

where

$$\alpha_n \equiv \sum_{m=1}^6 (\hat{\delta}_m \cdot \hat{u}_f) U_m(Q_1) \dots U_m(Q_n) . \quad (2.16)$$

Substituting (2.15) into (2.2) gives

$$\Gamma_n = \gamma_n \Sigma_n , \quad (2.17)$$

where

$$\gamma_n = \frac{9\pi\rho^2}{(1-2\rho)^2} \frac{1}{n!} \left(\frac{B a_{nn}^3}{\hbar} \right)^2 \left(\frac{\hbar}{m_r \omega a_{nn}^2} \right) \left(\frac{\hbar}{2\rho^2 m_{<} a_{nn}^2} \right)^n \\ \times [1 - \exp(-\hbar\omega/k_B T)]$$

and

$$\Sigma_n \equiv \frac{1}{N} \sum_{Q_1} \frac{n(\omega_{Q_1})+1}{\omega_{Q_1}} \cdots \frac{1}{N} \sum_{Q_n} \frac{n(\omega_{Q_n})+1}{\omega_{Q_n}} \\ \times \left| \alpha_n \right|^2 N \Delta(K_n) \delta(\omega - \omega_{Q_1} - \cdots - \omega_{Q_n}) \quad (2.18)$$

Substituting (2.17) into (2.1) gives, for $\omega^2 \gg \omega_f^2 + \Gamma_n^2$,

$$\beta_n = \sqrt{\frac{\pi}{2}} D_\rho K \omega_{mx}^5 \frac{1}{n_\omega+1} \frac{1}{\omega_{n!}^4} (\omega_{mx} D_e)^n \Sigma_n, \quad (2.19)$$

where

$$(n_\omega+1)^{-1} = 1 - \exp(-\hbar\omega/k_B T)$$

$$D_\rho \equiv \frac{1}{\sqrt{2\pi}} \left(\frac{6\pi\rho}{1-2\rho} \right)^2, \quad D_e \equiv \frac{\hbar}{2\rho^2 a_{nn}^2 m_{<} \omega_{mx}},$$

$$K \equiv \frac{B^2 e^{*2} a_{nn} \omega_f}{\hbar c m_r^2 n_r \omega_{mx}^5},$$

and ω_{mx} , which cancels out of (2.19), was introduced for later convenience.

From (2.18) and (2.16),

$$\begin{aligned} \Sigma_n = & \sum_{m=1}^6 \sum_{m'=1}^6 (\hat{\delta}_m \cdot \hat{u}_f)(\hat{\delta}_{m'} \cdot \hat{u}_f) \frac{1}{N} \sum_{Q_1} \frac{n(\omega_{Q_1})+1}{\omega_{Q_1}} U_m(Q_1) U_{m'}(Q_1)^* \\ & \times \cdots \times \frac{1}{N} \sum_{Q_n} \frac{n(\omega_{Q_n})+1}{\omega_{Q_n}} U_m(Q_n) U_{m'}(Q_n)^* \\ & \times N \Delta(\tilde{K}_n) \delta(\omega - \omega_{Q_1} - \cdots - \omega_{Q_n}) . \end{aligned} \quad (2.20)$$

It can be shown that β_n is independent of the direction of \hat{u}_f for the NaCl structure. The proof involves using

$$U_m(b_i, -\tilde{k}_i) = U_m(b_i, \tilde{k}_i)^* \quad (2.21)$$

and

$$U_m(Q_i) = -U_{-m}(Q_i)^* , \quad (2.22)$$

where $U_{-m}(Q_i)$ is obtained from (2.11) and (2.12a) by replacing $\hat{\delta}_m$ by $-\hat{\delta}_m$.

These results (2.21) and (2.22), which follow directly from (2.11) and (2.12a), are used in (2.20), the dummy indices in the sums over the components of the wavevectors are relabeled, and the invariance of ω_{Q_i} to the symmetry operations of the cubic crystal are used to complete the proof.

Since the value of β_n is independent of direction of \hat{u}_f , we choose

$$\hat{u}_f = \hat{x}_1 , \quad (2.23)$$

where \hat{x}_1 is a unit vector along a unit-cube axis. Then, only the two terms with

$\tilde{\delta}_m = \pm a_{nn} \hat{x}_1$ in (2.16) are nonvanishing:

$$\alpha_n = U_x(Q_1) \cdots U_x(Q_n) - U_{-x}(Q_1) \cdots U_{-x}(Q_n) . \quad (2.24)$$

III. Closed-Form Approximation to β_2

For $n = 2$, (2.24) gives

$$\alpha_2 = \left\{ \begin{aligned} & \left(u_{<Q_1x} - \sqrt{\frac{m_{<}}{m_{>}}} u_{>Q_1x} e^{i a_{nn} k_{1x}} \right) \\ & \times \left(u_{<Q_2x} - \sqrt{\frac{m_{<}}{m_{>}}} u_{>Q_2x} e^{-i a_{nn} k_{1x}} \right) \\ & - \left(u_{<Q_1x} - \sqrt{\frac{m_{<}}{m_{>}}} u_{>Q_1x} e^{-i a_{nn} k_{1x}} \right) \\ & \times \left(u_{<Q_2x} - \sqrt{\frac{m_{<}}{m_{>}}} u_{>Q_2x} e^{i a_{nn} k_{1x}} \right) \end{aligned} \right\}, \quad (3.1)$$

where subscript x denotes the x_1 component, and wavevector conservation,

$k_{2x} = -k_{1x}$, has been used. Combining terms in (3.1) and using

$$\tilde{u}_{\tau - kb} = \tilde{u}_{\tau kb}$$

gives

$$\alpha_2 = 2i \sqrt{\frac{m_{<}}{m_{>}}} \left(u_{<k_1 b_1 x} u_{>k_1 b_2 x} - u_{>k_1 b_1 x} u_{<k_1 b_2 x} \right) \sin k_{1x} a_{nn}. \quad (3.2)$$

From (2.18) with $n = 2$

$$\Sigma_2 = \frac{1}{N} \sum_{k_1 b_1 b_2} \frac{n(\omega_{k_1 b_1}) + 1}{\omega_{k_1 b_1}} \frac{n(\omega_{k_1 b_2}) + 1}{\omega_{k_1 b_2}} \\ \times \left| \alpha_2 \right|^2 \delta(\omega - \omega_{k_1 b_1} - \omega_{k_1 b_2}). \quad (3.3)$$

The value of α_2 tends to be small in a number of cases. First, for both phonons (Q_1 and Q_2) on the same branch, i.e., $b_1 = b_2$, (3.2) gives the well known selection rule^{7,11} $\alpha_2 = 0$; i.e.,

$$\beta_2 = 0, \quad \text{for } b_1 = b_2. \quad (3.4)$$

For $k_1 a_{nn} \ll 1$, $|\sin k_{1x} a_{nn}|^2 \approx (k_{1x} a_{nn})^2 \ll 1$, and the contribution to β_2 is small.

For the one-dimensional diatomic chain (Ref. 10, p. 176, for example) and for the three-dimensional NaCl structure for \underline{k} along $[111]$, the optical and acoustical modes at the zone boundary correspond to standing waves with only the lighter and heavier masses, respectively, vibrating:

$$u_{T<Q} = 0, \quad u_{T>Q} = \hat{u}_{T>Q}, \quad \begin{array}{l} \text{acoustical,} \\ \text{zone edge} \end{array} \quad (3.5)$$

$$u_{T<Q} = \hat{u}_{T<Q}, \quad u_{T>Q} = 0, \quad \begin{array}{l} \text{optical,} \\ \text{zone edge} \end{array}. \quad (3.6)$$

If both modes in (3.2) obey either (3.5) or (3.6), then $\alpha_2 = 0$. Even though (3.5) and (3.6) are not satisfied exactly for other points in the zone, this result suggests that the quasi-selection rule that β_2 is small unless one output phonon is optical and the other acoustical may hold for NaCl-structure crystals. The validity of this proposed quasi-selection rule, which has several important consequences,³ will be examined in detail in a later report.

The sum Σ_2 in (3.3) can be approximated as follows. Consider the term $b_1 = \text{LO}$ and $b_2 = \text{LA}$ and the term $b_1 = \text{LA}$ and $b_2 = \text{LO}$, where LO and LA

denote longitudinal optical and longitudinal acoustical, respectively. Since (3.3) is unchanged if b_1 and b_2 are interchanged, these two terms give the same contribution to Σ_2 .

A factor of $1/3$ will be included in the value of $|\alpha_2|^2$ to account for several regions in k space in which $|\alpha_2|^2$ is small. These regions are as follows: The factor $\sin k_{1x} a_{nn}$ in (3.2) makes the contribution to Σ_2 from the volume in k space near the plane $k_{1x} = 0$ small. Similarly, $|\alpha_2|^2$ is small for all directions when $ka_{nn} \ll 1$. At the zone edges along $[100]$ axes, $ka_{nn} = \pi$, and the factor $\sin k_{1x} a_{nn}$ in (3.2) is equal to zero.

In the rest of k space, the value of $|\alpha_2|^2$ will be approximated by the value

$$|\alpha_2|_{111, ZB}^2 = \frac{4}{9} \frac{m_{<}}{m_{>}} \quad (3.7)$$

at the zone boundary along a $[111]$ axis. [Note that at this symmetry point, which is commonly denoted L , (3.5) and (3.6) give

$$u_{>LO} = u_{<LA} = 0, \quad u_{<LO} = u_{>LA} = 1. \quad (3.8)$$

Since the x component of a unit vector along the $[111]$ axis is $1/\sqrt{3}$, the value of the square of the u factor in parentheses in (3.2) is $1/9$.] With the factor-of-3 reduction in $|\alpha_2|^2$ discussed in the preceding paragraph, and a factor of two included for the two choices of b_1 and b_2 discussed above,

$$|\alpha_2|^2 = \frac{8}{27} \frac{m_{<}}{m_{>}}. \quad (3.9)$$

The density of longitudinal acoustical states is rather sharply peaked at¹²

$$\omega_{LA} \equiv 2.7 \times 10^{13} \text{ rad/sec.} \quad (3.10)$$

(See Fig. 4.) Thus, $\omega_{\mathbf{k}_1 LA}$ will be set equal to the constant ω_{LA} . With these approximations, (3.3) and (3.9) give

$$\Sigma_{2LL} = \frac{8}{27} \frac{m_{<}}{m_{>}} \frac{n(\omega_{LA})+1}{\omega_{LA}} \frac{1}{N} \sum_{\mathbf{k}_1} \frac{n(\omega_1)+1}{\omega_1} \delta[\omega_1 - (\omega - \omega_{LA})] \quad (3.11)$$

for the contribution to Σ_2 from the LO and LA modes. Since the summand now is a function of ω_1 only, the sum on \mathbf{k}_1 can be replaced by an integral over ω_1

$$\frac{1}{N} \sum_{\mathbf{k}_1} f(\omega_1) \cong \int_0^\infty d\omega_1 g_0(\omega_1) f(\omega_1),$$

where the density of optical states $g_0(\omega)$ is normalized to unity

$$\int_0^\infty d\omega g_0(\omega) = 1. \quad (3.12)$$

Evaluating the trivial integral in (3.11) gives

$$\Sigma_{2LL} = \frac{8}{27} \frac{m_{<}}{m_{>}} g_0(\omega - \omega_{LA}) \frac{n(\omega_{LA})+1}{\omega_{LA}} \frac{n(\omega - \omega_{LA})+1}{\omega - \omega_{LA}}. \quad (3.13)$$

A rough sketch of Γ_{2LL} from (3.13) and (2.17) is shown in Fig. 5 as a dashed curve. It will be argued below that the effect of replacing the delta function

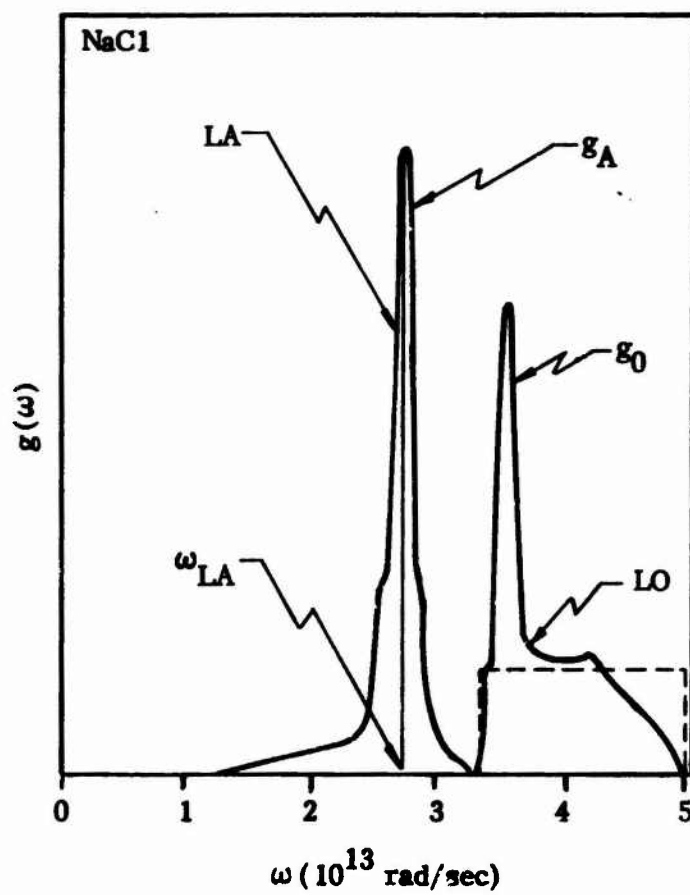


Fig. 4. Densities of states for LA and LO phonons in NaCl after Raunio and Rolandson (Ref. 12).

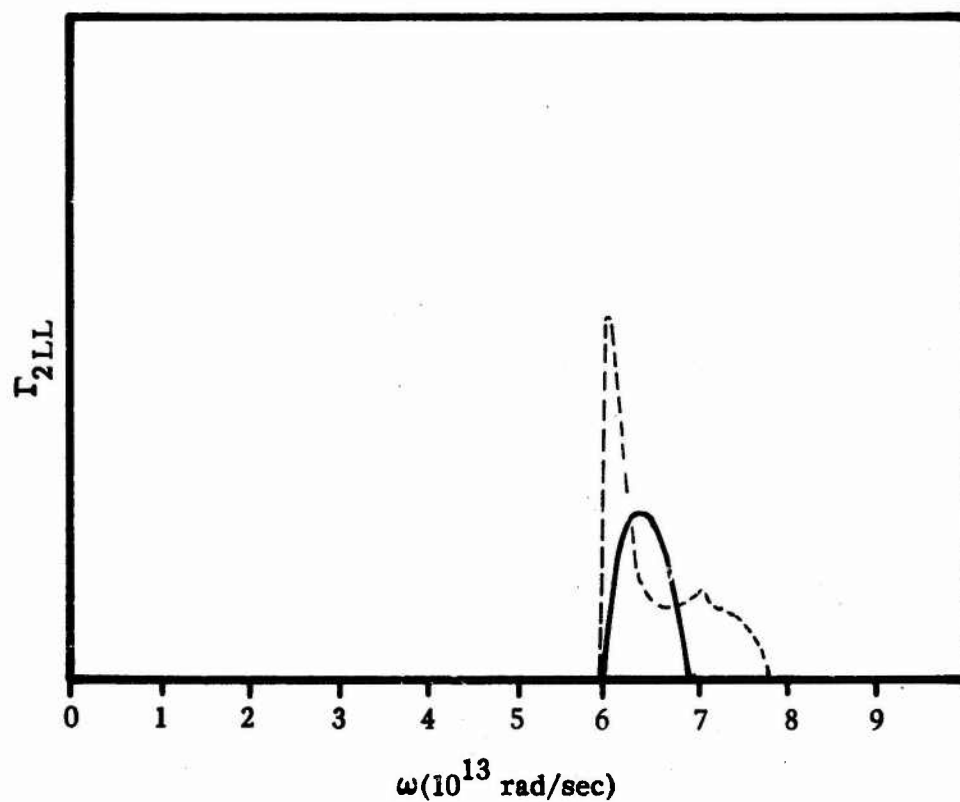


Fig. 5. Rough estimate of the relaxation frequency Γ_{2LL} of the fundamental mode decaying into LO and LA modes (heavy curve). The effect on Γ_{2LL} of relaxing the approximation $g_{LA}(\omega) = \delta(\omega - \omega_{LA})$ and of allowing the LA and LO phonons to have finite lifetimes is illustrated schematically as the solid curve.

distribution of LA modes by an $(\omega - \omega_0)^2$ distribution is to make Γ_{2LL} higher and narrower. Furthermore, the finite lifetimes of the LA and LO output phonons are expected to eliminate sharp peaks in Γ_{2LL} . Thus, Γ_{2LL} can be approximated by the solid curve in Fig. 5.

The numerical value of Γ_{2LL} at the peak of the solid curve in Fig. 5 can be obtained by numerical integration of (3.12), using the functional form in the figure and the normalization (3.12). The result is

$$g_0(\omega - \omega_{LA})_{mx} = 1.7 \times 10^{-13} \text{ sec/rad} = \frac{8.3}{\omega_{LO}}, \quad (3.14)$$

where $\omega_{LO} = 4.9 \times 10^{13}$ rad/sec. The peak in the solid curve in Fig. 5 occurs at $\omega = \omega_{LA} + \omega_{gp} = 6.3 \times 10^{13}$ rad/sec. This defines ω_{gp} . From (3.14), (3.13), and (2.17),

$$(\Sigma_{2LL})_{mx} = \frac{2.46}{\omega_{LO}} \frac{m_{<}}{m_{>}} \frac{n(\omega_{LA})+1}{\omega_{LA}} \frac{n(\omega_{gp})+1}{\omega_{gp}}$$

and

$$(\Gamma_{2LL})_{mx} \equiv \gamma_2 (\Sigma_{2LL})_{mx} \cong \frac{2.7\pi}{(1-2\rho^2)\rho^2} \left\{ 1 - \exp[-(\omega_{LA} + \omega_{gp})/\omega_T] \right\}$$

$$\times \frac{\hbar B^2 [n(\omega_{LA})+1][n(\omega_{gp})+1]}{m_r m_{<} m_{>} (\omega_{LA} + \omega_{gp}) \omega_{LO} \omega_{LA} \omega_{gp}}$$

$$= 1.0 \times 10^{12} \text{ rad/sec}, \quad \text{at 300 K} \quad (3.15)$$

for the value of Γ_{2LL} at the peak at $\omega \cong 6.3 \times 10^{13}$ rad/sec. In units of 10^{13} rad/sec

$$\omega_{LA} = 2.7 ,$$

$$\omega_{LO} = 4.9 ,$$

$$\omega_{gp} = 3.6 ,$$

$$\omega_{LO} + \omega_{gp} = 6.3 ,$$

$$\omega_T = 3.93 ,$$

$$\text{at } T = 300 \text{ K} .$$

Substituting $(\Gamma_{2LL})_{mx} = 1.0 \times 10^{12}$ rad/sec from (3.15) into (2.1) gives

$$(\beta_2)_{LLmx} = 19 \text{ cm}^{-1} \quad (3.16)$$

A comparison of this result with the numerical results currently underway and a comparison of the numerical results with experimental results will be given in a future report.

A second approximation to the value of Σ_{2LL} can be obtained by approximating the Brillouin zone by a sphere of radius k_{mx} and selecting linear dispersion relations for the LO and LA branches to match the densities of states.

For the LA branch, take

$$\omega_{kLA} = v_A (k - k_{mx}) + \omega_A , \quad v_A \equiv (\omega_A - \bar{\omega}_A) / k_{mx} . \quad (3.17)$$

See Fig. 6a. Then using

$$\sum_k f(k) = \frac{3N}{k_{mx}} \int_0^{k_{mx}} dk k^2 f(k) \quad (3.18)$$

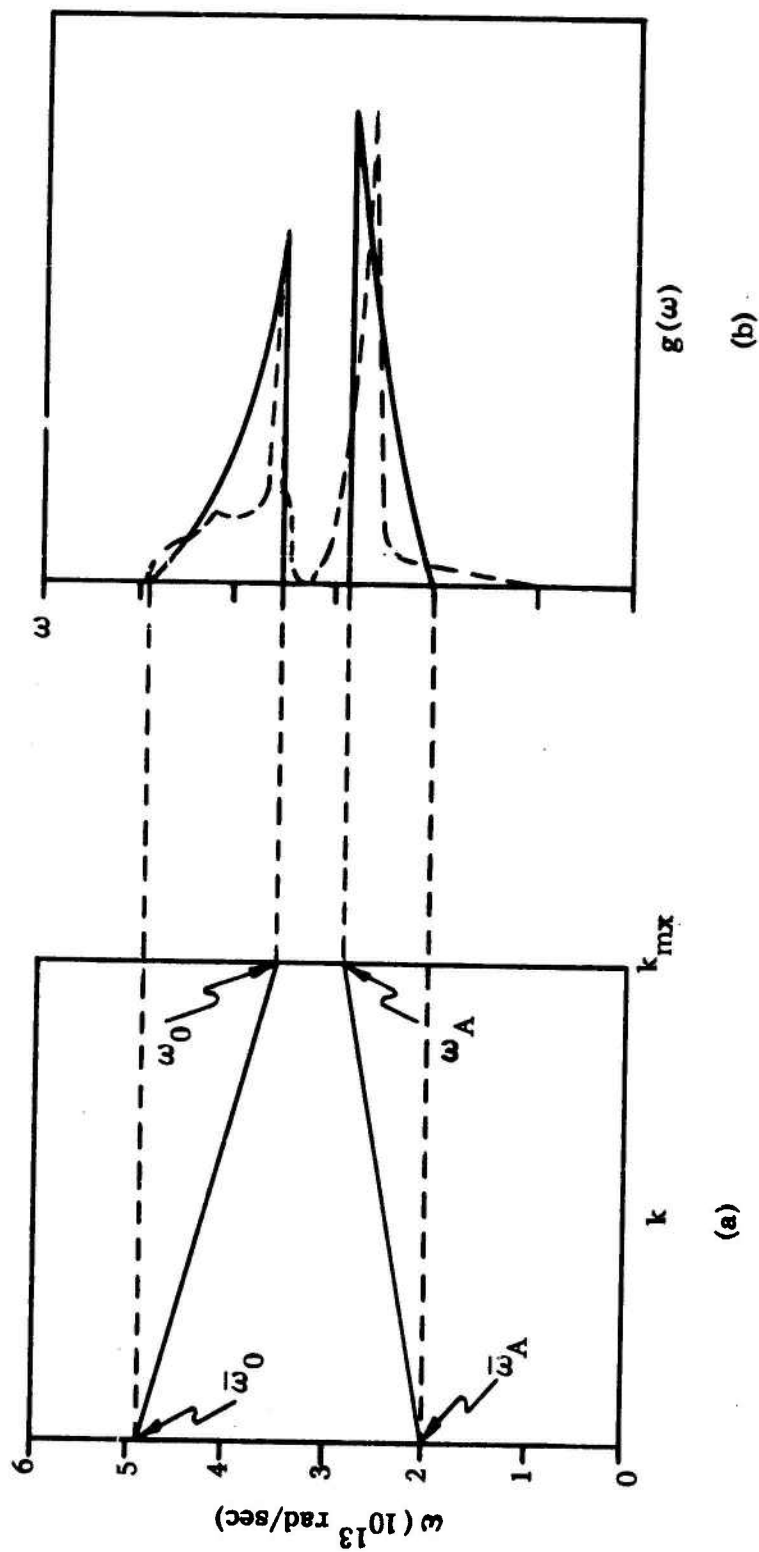


Fig. 6. Approximate dispersion relations (a) and the resulting density of states $g(\omega)$ sketched as solid line in (b). The density of states from Fig. 4 is repeated as the dashed lines.

in

$$g_{LA}(\omega) = \sum_{\vec{k}} \delta(\omega_{\vec{k}_{LA}} - \omega)$$

gives

$$g_{LA}(\omega) = \frac{3N}{k_{mx}^3} \int_0^{k_{mx}} dk k^2 \delta(\omega_{\vec{k}_{LA}} - \omega) . \quad (3.19)$$

Using (3.17), the delta function can be written as

$$\delta(\omega_{\vec{k}_{LA}} - \omega) = \delta[v_A(k - k_{mx}) + \omega_A - \omega] = \frac{1}{v_A} \delta(k - k_A) ,$$

where

$$k_A \equiv k_{mx} - \frac{\omega_A - \omega}{v_A} = \frac{\omega - \bar{\omega}_A}{\omega_A - \bar{\omega}_A} k_{mx} .$$

Using these last two results and evaluating the integral in (3.19) gives

$$\begin{aligned} g_{LA}(\omega) &= \frac{3N(\omega - \bar{\omega}_A)^2}{(\omega_A - \bar{\omega}_A)^3} , & \text{for } \bar{\omega}_A < \omega < \omega_A \\ &= 0 , & \text{otherwise .} \end{aligned} \quad (3.20)$$

For the LO branch, take

$$\omega_{\vec{k}_{LO}} = -v_0(k - k_{mx}) + \omega_0 , \quad v_0 \equiv (\bar{\omega}_0 - \omega_0)/k_{mx} . \quad (3.21)$$

See Fig. 6a. The same type of analysis as above gives

$$\begin{aligned} g_{LO}(\omega) &= \frac{3N(\bar{\omega}_0 - \omega)^2}{(\bar{\omega}_0 - \omega_0)^3} & \text{for } \omega_0 < \omega < \bar{\omega}_0 \\ &= 0 , & \text{otherwise.} \end{aligned} \quad (3.22)$$

The densities of states in (3.20) and (3.22) are sketched in Fig. 6b. Formally inserting a sine factor [see (3.2)] in (3.9) gives

$$|\alpha_2|^2 = \frac{8}{27} \frac{m_{Na}}{m_{Cl}} \sin^2 k_1 a_{nn}.$$

With (3.3), this gives

$$\begin{aligned} \Sigma_{2LL} = & \frac{8}{27} \frac{m_{Na}}{m_{Cl}} \frac{3}{k_{mx}} \int_0^{k_{mx}} dk k^2 \frac{n(\omega_{kLA})+1}{\omega_{kLA}} \\ & \times \frac{n(\omega_{kLO})+1}{\omega_{kLO}} \delta(k - k_L) \sin^2 k_1 a_{nn}, \end{aligned} \quad (3.23)$$

where ω_{kLA} and ω_{kLO} are given by (3.17) and (3.21), respectively, and

$$k_L = \frac{\bar{\omega}_0 + \bar{\omega}_A - \omega}{\bar{\omega}_0 + \bar{\omega}_A - \omega_0 - \omega_A} k_{mx}.$$

Evaluating the integral in (3.23) gives

$$\begin{aligned} \Sigma_{2LL} = & \frac{8}{9} \frac{m_{Na}}{m_{Cl}} \frac{(\bar{\omega}_0 + \bar{\omega}_A - \omega)^2}{(\bar{\omega}_0 + \bar{\omega}_A - \omega_0 - \omega_A)^3} \frac{n(\omega_{k_L LA})+1}{\omega_{k_L LA}} \\ & \times \frac{n(\omega_{k_L LO})+1}{\omega_{k_L LO}} \sin^2 k_L a_{nn}, \quad \text{for } \omega_0 + \omega_A < \omega < \bar{\omega}_0 + \bar{\omega}_A \\ = & 0 \quad \text{otherwise.} \end{aligned} \quad (3.24)$$

Here $\omega_{k_L LA}$ and $\omega_{k_L LO}$ are the values of ω_{kLA} and ω_{kLO} from (3.17) and (3.21) with $k = k_L$.

The maximum value of (3.24), which occurs at $\omega = \omega_0 + \omega_A$ (i. e., $k_L = k_{mx}$), is

$$\Sigma_{mx} = \frac{8}{9} \frac{m_{<}}{m_{>}} \frac{1}{(\bar{\omega}_0 + \bar{\omega}_A - \omega_0 - \omega_A)} \frac{n(\omega_A) + 1}{\omega_A} \times \frac{n(\omega_0) + 1}{\omega_0} , \quad (3.25)$$

where $\sin k_{mx} a_{nn}$ was set equal to one formally. In units of 10^{13} rad/sec,

$$\bar{\omega}_0 = \bar{\omega}_{LO} = 4.9 ,$$

$$\omega_0 = \omega_{gp} = 3.5 ,$$

$$\bar{\omega}_A = 2.0 ,$$

$$\omega_A = 2.8 ,$$

$$\bar{\omega}_0 + \bar{\omega}_A = 6.9 ,$$

$$\omega_0 + \omega_A = 6.3 .$$

Thus

$$\bar{\omega}_0 + \bar{\omega}_A - \omega_0 - \omega_A = 0.6 \times 10^{13} \text{ rad/sec} = \omega_{LO}/8.2 .$$

and (3.25) can be written as

$$\Sigma_{mx} = \frac{7.3}{\omega_{LO}} \frac{m_{<}}{m_{>}} \frac{n(\omega_A) + 1}{\omega_A} \frac{n(\omega_0) + 1}{\omega_0} . \quad (3.26)$$

In comparing (3.26) with the previous result (3.14), the unmodified curve (dashed) in Fig. 5 should be used. Thus, (3.14) should be multiplied by a factor of 1.9, which is the ratio of the peaks of the two curves in Fig. 5. Then, with $\omega_0 = \omega_{gp}$ and $\omega_A = 2.8 \times 10^{13}$ rad/sec and $\omega_{LA} = 2.7 \times 10^{13}$ rad/sec, the value of Σ_{mx} in (3.26) is approximately a factor of 1.5 times larger than the corresponding value in (3.14), which is good agreement.

In the second model [spherical Brillouin zone and $\omega = f(|k|)$], setting $\bar{\omega}_A = \omega_A = \omega_{LA}$ corresponds to using the delta function approximation to the density of LA states $g_{LA}(\omega)$. For this second model, it will now be shown that the effect of replacing the delta-function approximation to $g_{LA}(\omega)$ by the quadratic density (3.20) (with $\bar{\omega}_A \neq \omega_A$) is to reduce the region over which Γ_{2LL} is nonzero and increase the maximum value of Γ_{2LL} .

Setting $\bar{\omega}_A = \omega_A = \omega_{LA}$ (i.e. $\bar{\omega}_0 - \bar{\omega}_A - \omega_0 - \omega_A = \bar{\omega}_0 - \omega_0 = \omega_{LO}/3.5$) in (3.25) gives

$$\Sigma_{mx} = \frac{3.1}{\omega_{LO}} \frac{m_{<}}{m_{>}} \frac{n(\omega_{LA})+1}{\omega_{LA}} \frac{n(\omega_{gp})+1}{\omega_{gp}} \quad (3.27)$$

as the maximum value of (3.24) in the delta-function approximation. The delta-function approximation to (3.24) is sketched as the dashed curve in Fig. 7. The corresponding curve for the density $g_{LA}(\omega)$ in (3.20) is shown as the solid curve.

This result that the delta-function approximation to Γ_{2LL} is nonzero over a larger region is surprising in view of the result in Sec. IV that Γ_{2LL} is a convolution of the two densities g_{LA} and g_{LO} (weighted appropriately). Recall that the

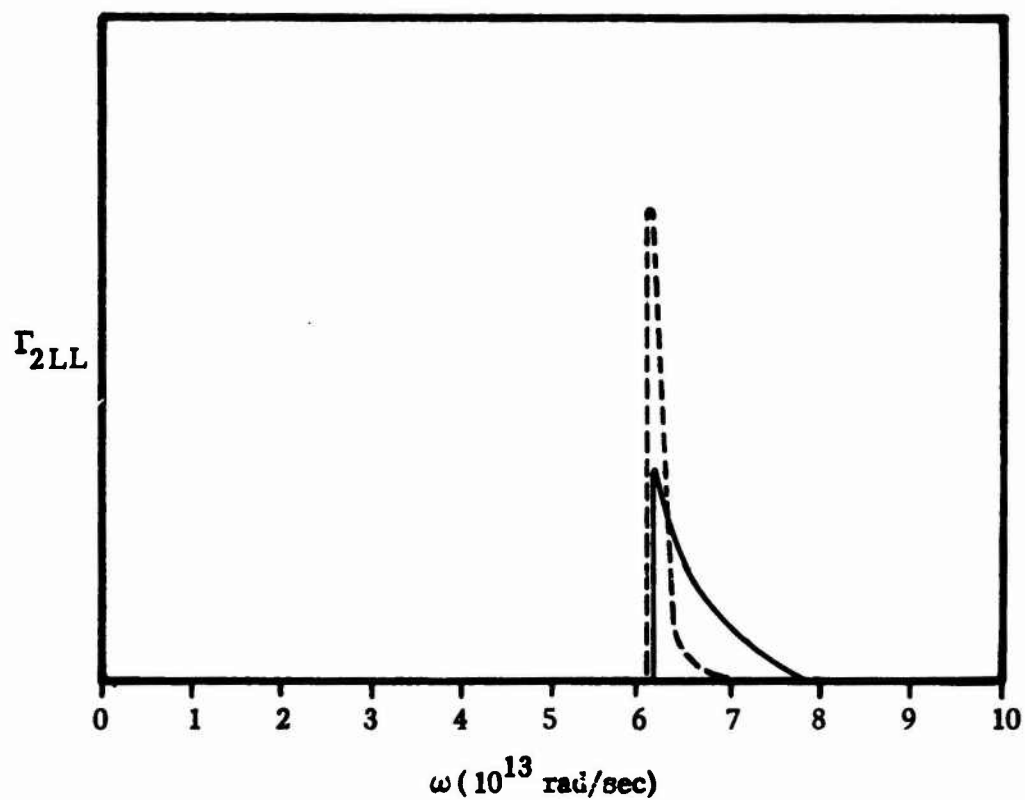


Fig. 7. Relaxation frequency Γ_{2LL} from the spherical-Brillouin-zone approximation (dashed line). Making the delta function approximation to $g_{LA}(\omega)$ gives the solid curve.

length of the nonzero region of convolved functions is the sum of the lengths of the nonzero regions of the individual functions. The difference in these two results arises from the fact that wavevector conservation was neglected in deriving the convolution result.

This difference can be understood in terms of the schematic illustrations in Fig. 8. The dispersion curves for the LO and LA modes are shown (for a spherical Brillouin zone) at the bottom of each section (a) ··· (d) of the figure. The bars at the top of each section indicate the nonzero regions of Γ_{2LL} (i. e., the region of ω for which $\omega = \omega_{LA} + \omega_{LO}$ for some pair of modes. The bars to the left are for the case of $k_{LA} = k_{LO}$, and those to the right are for no wavevector conservation. In going from Fig. 8c [for which $g_{LA}(\omega) = \delta(\omega - \omega_{LA})$] to Fig. 8b [for which $g_{LA}(\omega)$ is given by (3.20)], the left-hand bar decreases in length while the right-hand bar increases.

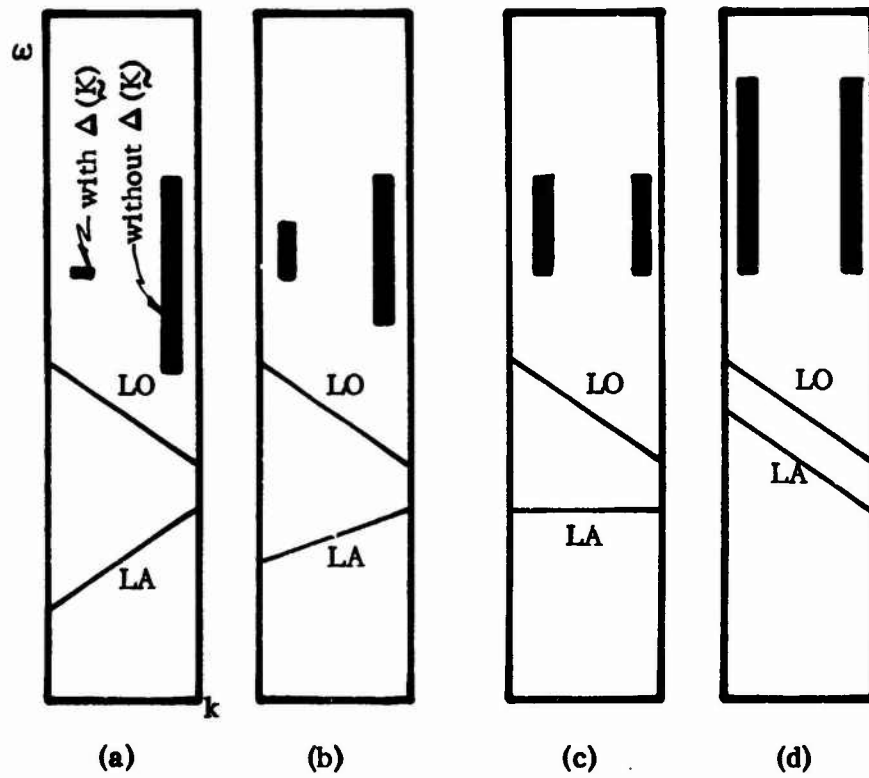


Fig. 8. Schematic illustration of regions for which the two-phonon-summation process with $\omega = \omega_{LA} + \omega_{LO}$ can conserve energy. The bars at the top left of each figure show this region for the case in which k is conserved, and those to the right are for no k conservation. The model dispersion curves for the four cases of interest are shown in the bottom portions of the figures.

IV. Closed-Form Approximation to β_n

The value of Σ_n in (2.18) for general n will be approximated by using the central-limit theorem as follows: First, wavevector conservation will be neglected by formally setting

$$N \Delta(K_n) = 1. \quad (4.1)$$

This is expected to be a good approximation for large n . Substituting (2.23) into (2.20) and using (4.1), (2.21), and (2.22) gives

$$\Sigma_n = \Sigma_{n+} + (-1)^{n+1} \Sigma_{n-}, \quad (4.2)$$

where

$$\begin{aligned} \Sigma_{n\pm} = & 2 \frac{1}{N} \sum_{Q_1} \frac{n_{Q_1}+1}{\omega_{Q_1}} \phi_{\pm}(Q_1) \cdots \frac{1}{N} \sum_{Q_n} \frac{n_{Q_n}+1}{\omega_{Q_n}} \phi_{\pm}(Q_n) \\ & \times \delta(\omega - \omega_{Q_1} - \cdots - \omega_{Q_n}), \end{aligned} \quad (4.3)$$

with

$$\phi_{\pm}(Q_i) \equiv [\text{Re } U_x(Q_i)]^2 \pm [\text{Im } U_x(Q_i)]^2.$$

By inserting the trivial relations

$$\int_{-\infty}^{\infty} d\Omega f(\Omega) \delta(\Omega - \omega_{Q_i}) = f(\omega_{Q_i}) \quad (4.4)$$

into (4.3), $\Sigma_{n\pm}$ can be written as

$$\begin{aligned} \Sigma_{n\pm} = & \frac{2 \langle \alpha_{\pm} \rangle^n}{\omega_{mx}^n} \int_{-\infty}^{\infty} d\Omega_1 \sigma_{\pm}(\Omega_1) \cdots \int_{-\infty}^{\infty} d\Omega_n \sigma_{\pm}(\Omega_n) \\ & \times \delta(\omega - \sum_{i=1}^n \Omega_i), \end{aligned} \quad (4.5)$$

where

$$\sigma_{\pm}(\Omega) = \frac{\omega_{mx}}{N \langle \alpha_{\pm} \rangle} \sum_Q \frac{n(\Omega)+1}{\omega_Q} \phi_{\pm}(Q) \times \delta(\Omega - \omega_Q) \quad (4.6)$$

and

$$\begin{aligned} \langle \alpha_{\pm} \rangle &\equiv \omega_{mx} \int_{-\infty}^{\infty} d\Omega \frac{1}{N} \sum_Q \frac{n(\Omega)+1}{\omega_Q} \phi_{\pm}(Q) \\ &\times \delta(\Omega - \omega_Q) \\ &= \frac{\omega_{mx}}{N} \sum_Q \frac{n(\omega_Q)+1}{\omega_Q} \phi_{\pm}(Q) . \end{aligned} \quad (4.7)$$

Note that $\sigma_{\pm}(\Omega)$ are normalized to unity:

$$\int_{-\infty}^{\infty} d\Omega \sigma_{\pm}(\Omega) = 1 .$$

The factor of ω_{mx} , which cancels out when (4.6) is substituted into (4.5), was introduced for later convenience.

For large n , the central-limit theorem¹³ reduces (4.5) to

$$\Sigma_{n\pm} = \frac{2 \langle \alpha_{\pm} \rangle^n}{\sqrt{2\pi n} \alpha_{\sigma_{\pm}} \omega_{mx}^{n+1}} e^{- (\omega - n \bar{\alpha}_{\pm} \omega_{mx})^2 / 2 n \alpha_{\sigma_{\pm}}^2 \omega_{mx}^2} \quad (4.8)$$

where

$$\bar{\omega}_{\pm} = \int_{-\infty}^{\infty} d\Omega \sigma_{\pm}(\Omega) \Omega \equiv \bar{\alpha}_{\pm} \omega_{mx} \quad (4.9)$$

and

$$\overline{\omega_{\pm}^2} = \int_{-\infty}^{\infty} d\Omega \sigma_{\pm}(\Omega) \Omega^2 = \overline{\alpha_{\pm}^2} \omega_{mx}^2 \quad (4.10)$$

and

$$\omega_{\sigma_{\pm}}^2 = \overline{\omega_{\pm}^2} - \overline{\omega_{\pm}^2} = \alpha_{\sigma_{\pm}}^2 \omega_{mx}^2. \quad (4.11)$$

With $\sigma_{\pm}(\Omega)$ given by (4.6), the results (4.9) and (4.10) become

$$\overline{\alpha_{\pm}} = \frac{1}{N \langle \alpha_{\pm} \rangle} \sum_Q (n_Q + 1) \phi_{\pm}(Q) \quad (4.12)$$

and

$$\overline{\alpha_{\pm}^2} = \frac{1}{N \langle \alpha_{\pm} \rangle \omega_{mx}} \sum_Q (n_Q + 1) \omega_Q \phi_{\pm}(Q). \quad (4.13)$$

Substituting (4.3) and (4.8) into (2.19) gives

$$\beta_n = \beta_{n+} + (-1)^{n+1} \beta_{n-} \cong \beta_{n+}$$

where the approximate equality is discussed in the following paragraph and

$$\begin{aligned} \beta_{n\pm} = & \frac{D \rho^K}{\alpha_{\pm}^4 \alpha_{\sigma_{\pm}} (n_{\omega} + 1)} \left(\frac{\overline{\alpha_{\pm}} \omega_{mx}}{\omega} \right)^4 \frac{1}{\sqrt{n!} n!} \left(\langle \alpha_{\pm} \rangle D_e \right)^n \\ & \times \exp \left[-(\omega - n \overline{\alpha_{\pm}} \omega_{mx})^2 / 2 n \alpha_{\sigma_{\pm}}^2 \omega_{mx}^2 \right] \end{aligned} \quad (4.14)$$

Using the central-limit theorem has reduced the multiple sum over $Q_1 \cdots Q_n$ [in (2.20)] to sums over the single phonon coordinate Q [in (4.7), (4.12), and (4.13)].

By calculating the values of the real and imaginary parts of $U_x(Q_i)$ for several points in the Brillouin zone using the eigenvector data of Karo and Hardy,¹⁴ it is simple to show that neither of the two parts is negligible in general. Thus, from

the definition of $\phi_{\pm}(Q_i)$ under (4.3), $\phi_{+} = \phi_{-}/s$, where $s \cong 2$. From (4.3), $\Sigma_{n+} \cong \Sigma_{n-}/s^n$; thus β_{n-} is negligible for large n since $\beta_{n\pm} \propto \Sigma_{n\pm}$.

The values of the α 's will now be estimated. First consider $U_x(Q)$. For $kL \ll 1$, the approximations (2.10) are valid. For modes near the zone edges, the one-dimensional results (3.5) and (3.6) will be used.

Substituting these results into (2.12) gives

$$|U_m(Q)|^2 \cong (\hat{\delta}_m \cdot \hat{u}_{<Q})^2, \quad \text{optical, zone edge}$$

$$|U_m(Q)|^2 \cong \frac{m_{<}}{m_{>}} (\hat{\delta}_m \cdot \hat{u}_{>Q})^2, \quad \text{acoustical, zone edge}$$

$$|U_m(Q)|^2 \cong \frac{m_{<}}{m_r} (\hat{\delta}_m \cdot \hat{u}_{\tau Q})^2, \quad \text{optical, } kL \ll 1$$

$$|U_m(Q)|^2 \cong \frac{m_{<}}{m_{>} + m_{<}} (\hat{\delta}_m \cdot \hat{u}_{\tau Q})^2 (\hat{\delta}_m \cdot \hat{k}_i)^2 (kL)^2, \quad \text{acoustical, } kL \ll 1.$$

Since $kL \ll 1$ in the last expression, this value of $|U_m(Q_i)|^2$ is negligible. Thus, as a rough approximation, $U_m(Q_i)$ will be set to zero for $\omega < f\omega_{mx}$, where $f < 1$. In the nonzero region, the remaining three terms are averaged to give

$$|U_x(\theta)|^2 \cong \frac{2}{3} \left(1 + \frac{m_{<}}{m_{>}} \right) (\hat{\delta}_m \cdot \hat{u}_{\tau Q})^2 \theta(f\omega_{mx} - \omega_{Q_i}), \quad (4.15)$$

where θ is the unit step function and

$$\frac{1}{3} \left(1 + \frac{m_{<}}{m_{>}} + \frac{m_{<}}{m_{>}} \right) = \frac{2}{3} \left(1 + \frac{m_{<}}{m_{>}} \right).$$

The value of the scalar product in (4.15) is approximated by $1/\sqrt{3}$, which is its value for $\delta_m = \hat{x}_1$ and $\hat{u}_{<I}$ a unit vector along $[111]$. The value of the square root of the average value of $\cos^2 \theta$ also is equal to $1/\sqrt{3}$:

$$\begin{aligned} \frac{1}{4\pi} \int d\Omega \cos^2 \theta &= \frac{1}{2} \int_0^\pi d\theta \sin \theta \cos^2 \theta \\ &= \int_0^1 du u^2 = 1/3 . \end{aligned}$$

This reduces (4.15) to

$$\left| U_x(\theta) \right|^2 \cong \frac{2}{9} \left(1 + \frac{m_{<}}{m_{>}} \right) \theta (f\omega_{mx} - \omega_Q) . \quad (4.16)$$

The sum in (4.7) now can be written as

$$\frac{1}{N} \sum_Q F(\omega_Q) = 6 \int_0^\infty d\omega_Q g(\omega_Q) F(\omega_Q) , \quad (4.17)$$

where the total density of states $g(\omega)$ is normalized to unity

$$\int_0^\infty d\omega g(\omega) = 1$$

in order to make the total number of states correct:

$$\sum_Q (1) = 6N \int_0^\infty d\omega g(\omega) = 6N .$$

Substituting (4.16) into (4.7) and using (4.17) gives

$$\langle \alpha_+ \rangle = \frac{4}{3} \left(1 + \frac{m_{<}}{m_{>}} \right) \left\langle \frac{n+1}{\omega} \theta \right\rangle \omega_{mx} , \quad (4.18)$$

where

$$\left\langle \frac{n+1}{\omega} \theta \right\rangle \equiv \int_{f\omega_{mx}}^{\infty} d\omega g(\omega) \frac{n(\omega)+1}{\omega} . \quad (4.19)$$

Similarly (4.12) and (4.13) give

$$\bar{\alpha}_+ = \frac{\langle (n+1) \theta \rangle}{\left\langle \frac{n+1}{\omega} \theta \right\rangle \omega_{mx}} \quad (4.20)$$

and

$$\bar{\alpha}_+^2 = \frac{\langle (n+1) \omega \theta \rangle}{\left\langle \frac{n+1}{\omega} \theta \right\rangle \omega_{mx}^2} , \quad (4.21)$$

where

$$\langle (n+1) \theta \rangle = \int_{f\omega_{mx}}^{\infty} d\omega g(\omega) [n(\omega) + 1]$$

and

$$\langle (n+1) \omega \theta \rangle = \int_{f\omega_{mx}}^{\infty} d\omega g(\omega) [n(\omega) + 1] \omega .$$

The density of states, shown as the solid curve in Fig. 9, will be approximated by the Debye density

$$g(\omega) = \frac{3\omega^2}{\omega_{mx}^3}, \quad (4.22)$$

as illustrated by the dashed curve in Fig. 9. The factor $n(\omega)+1$ will be approximated by its high-temperature limit

$$n(\omega)+1 = \frac{1}{1-e^{-\omega/\omega_T}} \cong \frac{\omega_T}{\omega} + \frac{1}{2}. \quad (4.23)$$

In the worst case of $\omega/\omega_T \cong 1$ for NaCl at 300 K, $n(\omega)+1 = 1.582$ and $(\omega_T/\omega) + \frac{1}{2} = 1.500$; thus, the approximation in (4.23) is quite good.

Substituting (4.21) and (4.22) into (4.18)-(4.21) and evaluating the simple integrals gives

$$\langle \alpha_+ \rangle = \frac{4}{3} \left(1 + \frac{m_{<}}{m_{>}} \right) \left[3(1-f) \frac{\omega_T}{\omega_{mx}} + \frac{3}{4} (1-f^2) \right], \quad (4.24)$$

$$\bar{\alpha}_+ = \frac{2 \left[(1-f^2) \frac{\omega_T}{\omega_{mx}} + \frac{1}{3} (1-f^3) \right]}{4(1-f) \frac{\omega_T}{\omega_{mx}} + (1-f^2)}, \quad (4.25)$$

$$\overline{\alpha_+^2} = \frac{\frac{1}{3} (1-f^3) \frac{\omega_T}{\omega_{mx}} + \frac{1}{8} (1-f^4)}{(1-f) \frac{\omega_T}{\omega_{mx}} + \frac{1}{4} (1-f^2)}, \quad (4.26)$$

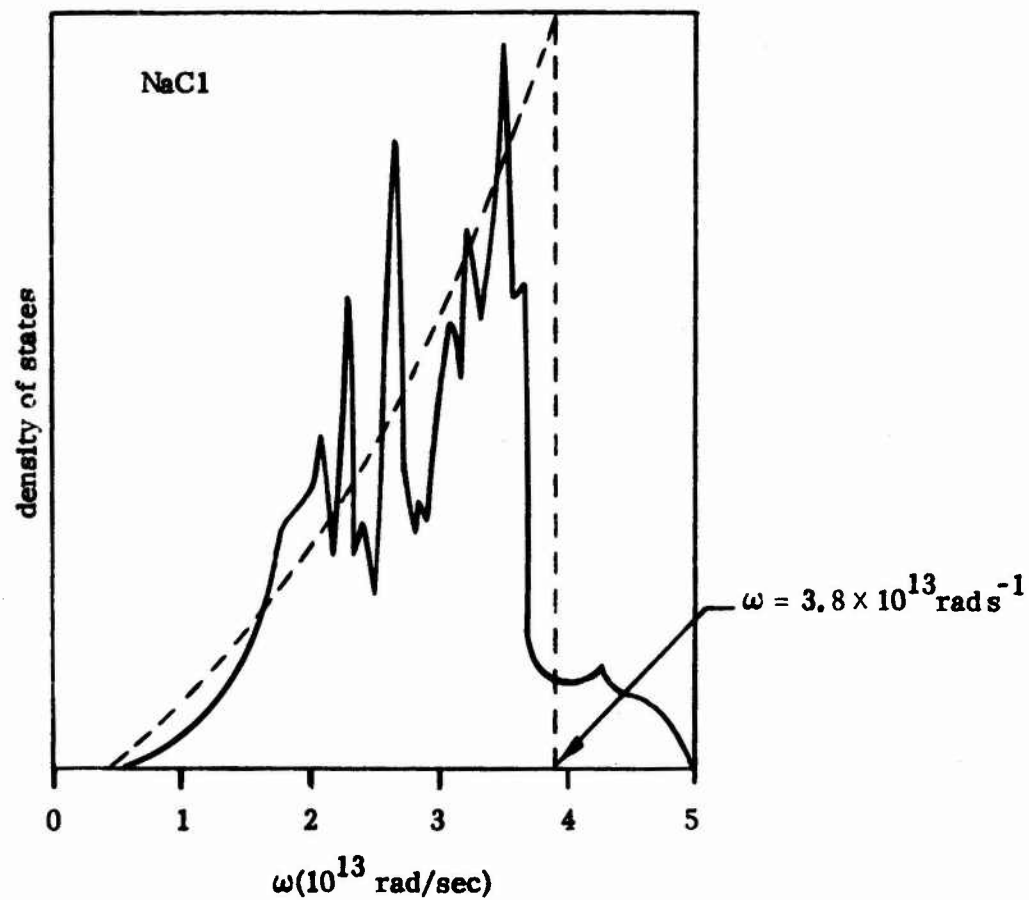


Fig. 9. Debye approximation (dashed ω^2 curve) to the density of states. The solid curve is the density of states calculated in Ref. 12.

and

$$\omega_{mx} \left\langle \frac{n+1}{\omega} \theta \right\rangle = 3(1-f) \frac{\omega_T}{\omega_{mx}} + \frac{3}{4} (1-f^2) . \quad (4.27)$$

Substituting these results (4.24)-(4.27) into (4.14) and assuming that the contribution from the β_{n-} term is negligible as discussed under (4.14) gives

$$\begin{aligned} \beta_n = & \frac{D_\rho K}{\bar{\alpha}_1^4 \alpha_{\sigma 1} (n\omega + 1)} \left(\frac{\bar{\alpha}_1 \omega_{mx}}{\omega} \right)^4 \frac{1}{\sqrt{n} n!} \\ & \times \left[\frac{4}{3} \left(1 + \frac{m_{<}}{m_{>}} \right) \left\langle \frac{n+1}{\omega} \omega_{mx} \theta \right\rangle D_e \right]^n \exp \left[- \frac{(\omega - n\bar{\alpha}_1 \omega_{mx})^2}{2 n \alpha_\sigma^2 \omega_{mx}^2} \right] \quad (4.28) \end{aligned}$$

where D_ρ and K are defined under (2.19).

Consider two values of f : $f = \frac{1}{2}$ and $f^3 = \frac{1}{2}$ (i.e., $f = 0.79$). The significance of considering more than one value of f will be discussed in Sec. V. The value of $f = \frac{1}{2}$ corresponds to assuming that $kL \ll 1$ for 1/8 of the modes (or 1/4 of the acoustical modes) according to the discussion of (4.15) above. Note that with $g(\omega)$ given by (4.22),

$$\int_{f\omega_{mx}}^{\omega_{mx}} d\omega g(\omega) = 1 - f^3 ,$$

which is equal to 7/8 for $f = \frac{1}{2}$. The value of $f^3 = \frac{1}{2}$ corresponds to considering only the optical modes. (Half of the modes -- the low-frequency, acoustical ones -- are then formally neglected, as discussed in Sec. V.)

Note that $f\omega_{\text{mx}} = 0.79 (3.8 \times 10^{13}) = 3.02 \times 10^{13}$ rad/sec, which is near the frequency 2.8×10^{13} rad/sec that roughly divides the optical and acoustical modes in Fig. 9.

Setting $f = \frac{1}{2}$ in (4.25)-(4.27) and using $\alpha_{\sigma}^2 = \overline{\alpha}^2 - \bar{\alpha}^2$ and $\omega_{\text{T}}/\omega_{\text{mx}} = 1.03$ for NaCl gives

$$\begin{aligned} \omega_{\text{mx}} \left\langle \frac{n+1}{\omega} \theta \right\rangle &= 2.11, & \bar{\alpha}_1 &= 0.757, \\ \overline{\alpha}_1^2 &= 0.594, & \alpha_{\sigma}^2 &= 0.594 - (0.757)^2 = 0.0210 = (0.145)^2. \end{aligned}$$

The corresponding values for $f^3 = \frac{1}{2}$ are

$$\begin{aligned} \omega_{\text{mx}} \left\langle \frac{n+1}{\omega} \theta \right\rangle &= 0.9165, & \bar{\alpha}_1 &= 0.899, \\ \overline{\alpha}_1^2 &= 0.811, & \alpha_{\sigma}^2 &= 0.0028 = (0.053)^2. \end{aligned}$$

The following values of parameters in (4.28) are used:

$$\begin{aligned} m_{>} &\equiv m_{\text{Cl}} = 5.89 \times 10^{-23} \text{ g}, & m_{<} &\equiv m_{\text{Na}} = 3.82 \times 10^{-23} \text{ g}, \\ m_{\text{r}} &= 2.32 \times 10^{-23} \text{ g}, & a_{\text{nn}} &= 2.815 \times 10^{-8} \text{ cm}, \\ n_{\text{r}} &= 1.5, & 1/\rho &= 9.05, \\ B &= 2.44 \times 10^{11} \text{ dyne/cm}^2, & e^* &= e = 4.80 \times 10^{-10} \text{ esu}, \end{aligned}$$

$$\omega_f = 3.09 \times 10^{13} \text{ rad/sec} ,$$

$$\omega_{mx} = 3.8 \times 10^{13} \text{ rad/sec } (\beta_n \text{'s independent of } \omega_{inx})$$

$$\overline{\alpha}_{\sigma_1} = 0.147 ,$$

$$\overline{\alpha}_1 = 0.757 ,$$

$$D_p = 2.85 ,$$

$$K = 5.92 \times 10^3 \text{ cm}^{-1} .$$

In Fig. 1, $\beta_2 \cdots \beta_7$ are plotted as the light curves. The sum $\beta = \sum_{n=2}^7 \beta_n$, plotted as the solid heavy curve, shows the approximate exponential behavior of β . The agreement between this theoretical result and experimental results (points and crosses in Fig. 1) is good in view of the simplicity of the model and the assumptions made. By adjusting the values of two parameters in (4.28), such as K and D_e , the experimental data can be fit to within the scatter of the points. By changing the value of the single interaction-strength parameter $1/\rho$ from 9.05 to 13.7, the heavy dashed curve in Fig. 1 is obtained. Results for materials other than NaCl, as well as computer evaluations of the multiple sums of β_n with $n = 2$ to 5 or 6, will be presented in a future report.

Concerning the value of ρ , it should be mentioned that the higher-order anharmonic coefficients are much more sensitive to the shape of the potential curve than are the quadratic terms, which are used in the analysis of the binding energy and bulk modulus. Thus, it would be reasonable to replace ρ by an n -dependent factor ρ_n . Since there appears to be no reasonable method of determining the values of ρ_n from first principles or from other experiments at present, the ρ_n would have to be considered as adjustable parameters. This would give five parameters to adjust in order to fit the experimental data in Fig. 1. Even though it is neither surprising nor impressive that an extremely good fit to the data can be obtained in this way, it is interesting that the value of $1/\rho_2$ is equal to the usual value of $1/\rho$ and the values of $1/\rho_3, 1/\rho_4 \cdots$ are somewhat larger.

The n -phonon regions, marked on Fig. 1 for $n = 3 - 6$, are given by the relations $(n - \alpha) \omega_f < \omega < (n + 1 - \alpha) \omega_f$, with values of α ranging from 0.5 for $n = 3$ to 0.8 for $n = 6$. The n -phonon region cannot be taken as $n\omega_f < \omega < (n + 1)\omega_f$, as $n\omega_{mx} < \omega < (n + 1)\omega_{mx}$, or as $n\omega_{LO} < \omega < (n + 1)\omega_{LO}$, as often done in the literature. In fact, the n -phonon regions shift as the temperature changes.

It has not been established conclusively that the Lax-Burstein-Born mechanism⁷ is negligible in polar crystals.^{14a} The fact that the present anharmonic-potential result explains the observed frequency dependence and order of magnitude of β suggests, though by no means proves, that the contribution of the anharmonic-potential mechanism is greater than that of the Lax-Burstein-Born mechanism over the experimental range of values of ω . The absence of a resonance denominator (2.1) in the Lax-Burstein-Born result would eliminate the factor ω^{-4} in (4.28), thus giving a significant deviation from an exponential frequency dependence. The frequency dependence and numerical values of the matrix elements in the Lax-Burstein-Born theory may be difficult to determine accurately, since they are expected to be rather strongly model dependent. (A simple rigid-ion model gives zero for the matrix elements.)

In the two previous reports,^{1,3} numerical values of β were obtained by making approximations that were different from those of the present report. Although the results are not too different, the present results are believed to be the more accurate of the two, and the form of the present results certainly is more convenient.

V. The Central-Limit Approximation

The central-limit theorem was found to be a powerful tool for obtaining the values of β_n for large n , at which straightforward computer calculations are impractical at present. However, considerable care must be exercised in the application of the central-limit approximation lest drastic errors should be introduced. In the present section and in Sec. VI it will be shown: that the confluence processes are negligible; that including the confluence processes and using the central-limit approximation gives drastically incorrect results for β ; and that truncating $g(\omega)$ can give improved values of β when the central-limit approximation is used and $\beta(\omega)$ is approximated by the locus of the peaks of the $\beta_n(\omega)$ curves.

The central-limit approximation will be applied to two model problems in order to illustrate these difficulties in applying the approximation to the present problem. First, consider the function in Fig. 10a. The n^{th} convolution of $f(\omega) \equiv f_1(\omega)$ is

$$f_n(\omega) = \int_{-\infty}^{\infty} d\omega_1 f(\omega_1) \cdots \int_{-\infty}^{\infty} d\omega_n f(\omega_n) \delta\left(\omega - \sum_{i=1}^n \omega_i\right). \quad (5.1)$$

From (5.1) it is easy to show that

$$f_2(\omega) = \int_{-\infty}^{\infty} d\omega_1 f(\omega_1) f(\omega - \omega_1), \quad (5.2)$$

$$f_n(\omega) = \int_{-\infty}^{\infty} d\omega_1 f_{n-1}(\omega_1) f(\omega - \omega_1). \quad (5.3)$$

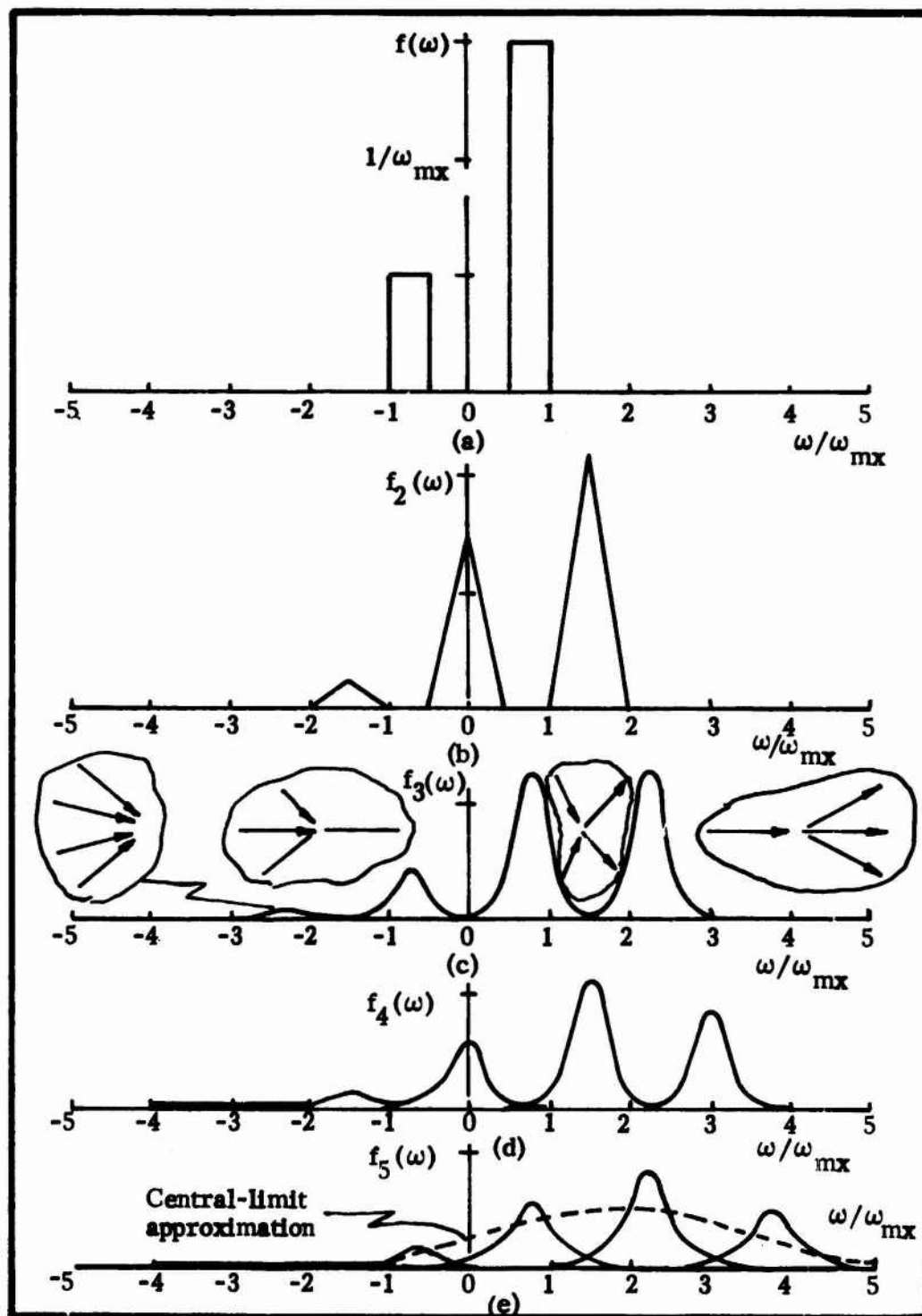


Fig. 10. The function $f(\omega)$, (a), and successive convolutions (b)-(e).

The result of the successive convolutions in (5.2) and (5.3) is shown in Fig. 10 for $n = 1, 2, \dots, 5$.

The central-limit approximation to $f_n(\omega)$ in (5.1) is

$$f_n(\omega) \cong \frac{1}{\sqrt{2\pi n} \omega_\sigma} \exp \left[-\frac{(\omega - n\bar{\omega})^2}{2n \omega_\sigma^2} \right], \quad (5.4)$$

where

$$\bar{\omega} \equiv \int_{-\infty}^{\infty} d\omega f(\omega) \omega \equiv \bar{\alpha} \omega_{mx}, \quad (5.5)$$

$$\overline{\omega^2} \equiv \int_{-\infty}^{\infty} d\omega f(\omega) \omega^2 \equiv \overline{\alpha^2} \omega_{mx}^2, \quad (5.6)$$

and

$$\omega_\sigma^2 \equiv \overline{\omega^2} - \bar{\omega}^2 \equiv \alpha_\sigma^2 \omega_{mx}^2. \quad (5.7)$$

Evaluating the integrals (5.5) and (5.6) for $f(\omega)$ in Fig. 10a gives

$$\bar{\omega} = \frac{3}{8} \omega_{mx}, \quad \overline{\omega^2} = \frac{7}{12} \omega_{mx}^2,$$

$$\omega_\sigma^2 = \frac{85}{192} \omega_{mx}^2 = (0.665 \omega_{mx})^2.$$

The result for $n = 5$ is shown as the dashed curve in Fig. 10e. The agreement with the exact solid curve is poor, since the central-limit approximation is not valid for the function in Fig. 10a unless n is very large. After convolving $f(\omega)$ n times, the Gaussian half-width of each peak is approximately $\sqrt{n} \omega_{\sigma+}$, where $\omega_{\sigma+} = \omega_{mx} / \sqrt{48}$ is the Gaussian half-width of the positive half of $f(\omega)$.

In order for the central-limit approximation to be valid, the width $\sqrt{n} \omega_{\sigma+}$ must equal the spacing $(3/4) \omega_{mx}$ of the two sections of $f(\omega)$, roughly. This gives $n/48 \cong 9/16$, or $n \cong 27$. Thus, n must be quite large before the central-limit result is valid for this function with a gap. This simple example will be used in Sec. VI to show that confluence processes are negligible in the exponential frequency region.

Next consider the function $F(\omega)$ in Fig. 11a. The central-limit approximation to the function

$$F_n(\omega) \equiv \int_{-\infty}^{\infty} d\omega_1 F(\omega_1) \cdots \int_{-\infty}^{\infty} d\omega_n F(\omega_n) \\ \times \delta\left(\omega - \sum_{i=1}^n \omega_i\right)$$

is

$$F_n(\omega) \cong \frac{1}{\sqrt{2\pi n} \omega_{\sigma}} \exp \left[-\frac{(\omega - n\bar{\omega})^2}{2n\omega_{\sigma}^2} \right],$$

where $\bar{\omega}$ and ω_{σ} are given by (5.5)-(5.7) with $f(\omega)$ replaced by $F(\omega)$. The functions $F_2(\omega)$ and $F_3(\omega)$ are plotted in Fig. 11. For this smooth function with no "gaps" the central-limit approximation is fairly good even for the very small values of $n = 2$ and 3 .

The following discussion is included for those interested in the details of the calculations. As a rough approximation to obtain preliminary results, the curve of $\beta = \sum \beta_n$ as a function of ω was approximated by the locus of the peaks of the individual β_n .^{1,3} (The size of the error introduced is apparent in Fig. 1.) Under this approximation, it is found that formally setting a

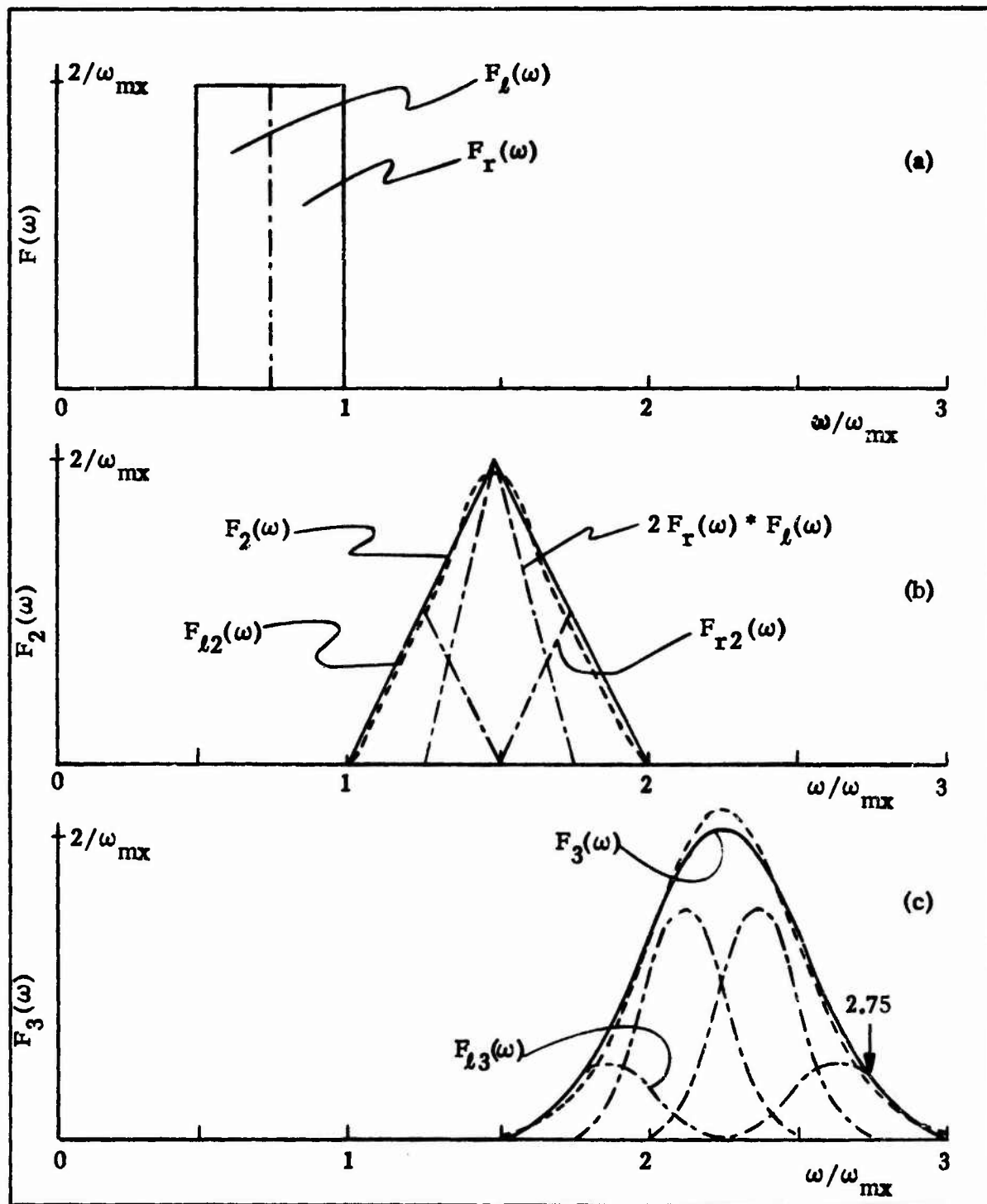


Fig. 11. Rectangular function $F(\omega)$ considered as the sum of two equal rectangular functions $F_l(\omega)$ and $F_r(\omega)$. The dashed curves in (b) and (c) are the central-limit approximations to F_2 and F_3 , respectively.

low-frequency portion of the density of states $g(\omega)$ equal to zero can increase the values of β . Increasing the value of f in (4.16), (4.19), and subsequent equations corresponds to such a truncation of $g(\omega)$. The reason for this result that decreasing the number of physical processes causes an increase in the value of β can be understood as follows. In Fig. 1 it is seen that the value of a given β_n , say β_6 , at its peak can be much smaller than the value of $\beta_{n-1} = \beta_5$ at the same frequency. Truncating $g(\omega)$ causes a reduction in the value of β_5 (especially at its peak and on the low-frequency side of the peak), but also causes the peak to shift to higher frequencies. This new peak lies nearer the true curve of $\beta = \sum \beta_n$ than does the old peak, as illustrated by the following example.

In order to examine the value of $F_n(\omega)$ in Fig. 11 in the wings (away from the peak), first consider $F(\omega)$ as the sum of the two equal rectangular functions

$$F(\omega) = F_\ell(\omega) + F_r(\omega) , \quad (5.8)$$

as shown in Fig. 11a. The first convolution $F_2(\omega)$ is then the sum of three terms, as seen by substituting (5.8) into (5.2) with $f(\omega)$ replaced by $F(\omega)$. This gives

$$\begin{aligned} F_2(\omega) = & \int_{-\infty}^{\infty} d\omega_1 [F_\ell(\omega_1) F_\ell(\omega - \omega_1) + F_\ell(\omega_1) F_r(\omega - \omega_1) \\ & + F_r(\omega) F_\ell(\omega - \omega_1) + F_r(\omega_1) F_r(\omega - \omega_1)] . \end{aligned} \quad (5.9)$$

The second and third integrals are equal as seen by making the transformation $\omega - \omega_1 \equiv \omega_1'$ in either integral. Thus, (5.9) gives

$$F_2(\omega) = F_{\ell 2}(\omega) + 2 F_{\ell}(\omega) * F_r(\omega) + F_{r 2}(\omega) . \quad (5.10)$$

where $*$ denotes the convolution. In the convolution notation, $F_{\ell 2}(\omega) = F_{\ell}(\omega) * F_{\ell}(\omega)$. The three functions in (5.10) are plotted in Fig. 11b. Similarly, $F_3(\omega)$ is the sum of four functions, as shown in Fig. 11c. In this figure, note that at $\omega/\omega_{mx} = 2.75$, the central-limit approximation (dashed line) has a smaller value than the exact result (solid line). Also note that at this value of ω/ω_{mx} , the central-limit approximation to $F_{r 2}(\omega)$ is a closer approximation to the correct value than is the central-limit approximation to $F(\omega)$. That is, if $F(\omega)$ is truncated to $F_r(\omega)$, the resulting central-limit approximation is more accurate in portions of the wings than the central-limit approximation to $F(\omega)$ itself.

In the same way, $F(\omega)$ could be truncated to the rectangular function $F_{rr}(\omega)$ extending from $\omega/\omega_{mx} = 7/8$ to 1. If the value of β_n in the wings of the exponential is important, formally truncating $g(\omega)$, by making f large in (4.16)-(4.19) for example, may result in a more accurate value of β_n . This result was the motivation for considering two values of f in Sec. IV. The result is similar to the result considered above and in Sec. VI that the central-limit approximations to β with confluence and splitting processes included is not as good an approximation as that obtained by including splitting processes only.

VI. Effect of Confluence Processes on β_n

It will now be shown that confluence processes are negligible in the exponential region. The analysis of Sec. IV, which is for the case of the splitting of the fundamental phonon into n phonons as in Fig. 3a, can be easily extended to include all confluence processes, such as those in (b) and (c) of Fig. 3. The general confluence process has m output phonons and $n - m + 1$ input phonons. The method below sums the diagrams over all values of m .

It can be shown that this generalization to include all confluence and splitting processes is accomplished simply by replacing $\delta(\Omega - \omega_Q)$ by $\delta(\Omega - \omega_Q) - \delta(\Omega + \omega_Q)$ in (4.6), giving

$$\sigma_{c\pm}(\Omega) = \frac{\omega_{mx}}{N \langle \alpha_{c\pm} \rangle} \sum_Q \frac{n(\Omega) + 1}{\omega_Q} \phi_{\pm}(Q) \times [\delta(\Omega - \omega_Q) - \delta(\Omega + \omega_Q)] , \quad (6.1)$$

and defining $g(-\omega) \equiv g(\omega)$ and

$$n(-\omega) \equiv -[n(\omega) + 1] ; \quad (6.2)$$

i.e., $n(-\omega) + 1 = -n(\omega)$. Standard Green's function analyses give the $\delta(\Omega + \omega_Q)$ terms automatically. See Eq. (4.19) of Ref. 6, for example. The resulting expressions for $\langle \alpha_{c\pm} \rangle$ are

$$\begin{aligned}
\langle \alpha_{c\pm} \rangle &= \omega_{mx} \int_{-\infty}^{\infty} d\Omega \frac{1}{N} \sum_Q \frac{n(\Omega)+1}{\omega_Q} \phi_{\pm}(Q) \\
&\times [\delta(\Omega - \omega_Q) - \delta(\Omega + \omega_Q)] \\
&= \frac{\omega_{mx}}{N} \sum_Q \frac{2n(\omega_Q)+1}{\omega_Q} \phi_{\pm}(Q)
\end{aligned} \tag{6.3}$$

and $\Sigma_{n\pm}$ still are equal to the n -fold convolution of $\sigma_{\pm}(\Omega)$ as in (4.5):

$$\Sigma_{nc\pm} = \frac{\langle \alpha_{c\pm} \rangle^n}{\omega_{mx}^n} \int_{-\infty}^{\infty} d\Omega_1 \sigma_{c\pm}(\Omega_1) \cdots \int_{-\infty}^{\infty} d\Omega_n \sigma_{c\pm}(\Omega_n) \delta(\omega - \sum_{i=1}^n \Omega_i) \tag{6.4}$$

Notice that the summation weighting functions $\sigma_{\pm}(\Omega)$ in Eq. (4.6) of Sec. IV are zero for negative Ω , while the confluence weighting functions in (6.1) are non-zero for both negative and positive values. For example, if the angle factors $\phi_{\pm}(Q)$ are approximated by a constant Φ_{\pm} , then (4.6) and (4.17) give

$$\begin{aligned}
\sigma_{\pm}(\Omega) &= \frac{6\Phi_{\pm}\omega_{mx}}{\langle \alpha_{\pm} \rangle} \int_0^{\infty} d\omega g(\omega) \frac{n(\Omega)+1}{\omega} \delta(\Omega - \omega) , \\
\sigma_{\pm}(\Omega) &= \frac{6\Phi_{\pm}\omega_{mx}}{\langle \alpha_{\pm} \rangle} g(\Omega) \frac{n(\Omega)+1}{\Omega} , & \text{for } \Omega > 0 , \\
&= 0 , & \text{for } \Omega < 0 .
\end{aligned} \tag{6.5}$$

Similarly, (6.1) and (4.17) give

$$\begin{aligned}\sigma_{c\pm}(\Omega) &= \frac{6\Phi_{\pm}\omega_{mx}}{\langle\alpha_{c\pm}\rangle} \int_0^{\infty} d\omega g(\omega) \frac{n(\Omega)+1}{\omega} \\ &\quad \times [\delta(\Omega-\omega) - \delta(\Omega+\omega)] , \\ \sigma_{c\pm}(\Omega) &= \frac{6\Phi_{\pm}\omega_{mx}}{\langle\alpha_{c\pm}\rangle} g(\Omega) \frac{n(\Omega)+1}{\Omega} , \quad \text{for } \Omega > 0 , \\ &= \frac{6\Phi_{\pm}\omega_{mx}}{\langle\alpha_{c\pm}\rangle} g(|\Omega|) \frac{n(|\Omega|)}{|\Omega|} , \quad \text{for } \Omega < 0 .\end{aligned}\tag{6.6}$$

Note that the top expression in (6.6) is formally correct for $\Omega < 0$ also, as seen by writing $\Omega = -|\Omega|$ and using (6.2).

The central-limit theorem could be used to evaluate the multiple integral in (6.4). The results, however, are quite misleading, as will now be shown. It is necessary to carry out the successive convolutions to obtain the values of β_2, β_3, \dots . Consider Σ_{nc+} in (6.4). In the example above, in which $\phi_{\pm}(Q)$ is approximated by a constant Φ_{\pm} , $\sigma_{c+}(\Omega)$ is given by (6.6). In the high-temperature limit, $n(\Omega)+1 \cong n(\Omega) \sim 1/\Omega$; thus, if $g(\Omega) \sim \Omega^2$ over its nonzero region, $\sigma_{c+}(\Omega)$ is constant over its nonzero regions. The function $f(\omega)$ in Fig. 10a is therefore a reasonable approximation to $\sigma_{c+}(\Omega)$ in (6.6). In fact, the ratio of 1 to 3 of the heights of the two peaks in Fig. 10a was chosen with foresight to agree with the room-temperature ratio $[n(\Omega)+1]/n(\Omega) \cong 3$ of the two peaks in σ_{c+} on the positive and negative Ω axes, according to (6.6).

Physically, the positive-axis peak in $f(\omega)$ in Fig. 10a corresponds to the creation of a phonon, and the negative-axis peak corresponds to the annihilation of a phonon. It is not difficult to show, by considering the frequency regions over which the various confluence processes can conserve energy, for example, that this interpretation of the two peaks in Fig. 10a is consistent with the following interpretation of the peaks in f_n in Fig. 10b-e. The peaks in these functions $f_n(\omega)$ correspond to the various splitting and confluence processes. For example, the last peak on the right of $f_3(\omega)$ corresponds to the splitting of the fundamental mode into three phonons and the next peak to the left corresponds to the confluence of a fundamental phonon with a thermally excited phonon to form two phonons, as illustrated on Fig. 10c.

The splitting peak (last to the right) is not the largest peak for a given n in general. However, in the present example, the other peaks can be neglected in the region of current interest since they are obscured by the contributions of lower-order terms (smaller n). For example, the last (splitting) peak of $n=3$ gives a much greater contribution to β than does the second peak from the right in $f_5(\omega)$: From (2.19) with the frequency dependence of $(n\omega + 1)^{-1}$ neglected and $\Sigma_n \cong \langle \alpha \rangle^n f_n(\omega) / \omega_{mx}^n$, β_n is given by the expression

$$\beta_n \sim \frac{1}{\omega_{mx}^4 n!} (\langle \alpha \rangle D_e)^n f_n(\omega) ,$$

where $\langle \alpha \rangle D_e \cong 0.1$. For the last β_3 peak in Fig. 10c,

$$(\beta_3)_1 \sim \frac{1}{3!} 10^{-3} (0.633 / \omega_{mx}) ,$$

and for the next-to-the-last β_5 peak

$$(\beta_5)_2 \sim \frac{1}{5!} 10^{-5} (0.4285 / \omega_{mx}).$$

Thus

$$(\beta_5)_2 / (\beta_3)_1 \cong 3.38 \times 10^{-4} \ll 1$$

so that $(\beta_5)_2$ is negligible. This simple example clearly illustrates that the confluence processes are negligible in the exponential frequency region; only the splitting process should be included.

The errors introduced by formally using the central-limit approximation to (6.4), which includes both the confluence and summation processes, are drastic. Direct calculation shows that the resulting values of β are incorrect by orders of magnitude in some cases. The difficulty can be seen simply by considering the positions of the peaks of the various β_n vs ω curves. For example, in Fig. 10e, the five-phonon peak is at $\omega \cong 2\omega_f$. Experimentally, this frequency is in the region of two-phonon peaks, not five-phonon peaks. An even more dramatic error results at high temperatures, where the heights of the negative-axis and positive-axis peaks are approximately equal. Then all β_n (for reasonable values of n) peak near $\omega = 0$, which is, of course, below the fundamental resonance frequency.

VII. Effects of Terms Other Than $V^{(n+1)}$ in \mathcal{K}_n

In the previous sections, only the term $V^{(n+1)}$ in \mathcal{K} [Eq. (2.4)] was considered. In determining the effect of the other terms $V^{(p)}$ with $p < n+1$ in (2.4), first the higher-order terms in the expansion of the square root in $R_{\ell m}$ in (2.5) are needed. With the definitions

$$\underline{u} \equiv \underline{u}_{\ell m} / \delta_{\ell m} , \quad A \equiv \hat{\delta}_{\ell m} \cdot \hat{u}_{\ell m} ,$$

and, formally,

$$\underline{u} \cdot \underline{u} = u^2 , \quad \hat{\delta} \cdot \underline{u} = Au ,$$

(2.5) becomes

$$\frac{R_{\ell m} - \delta_m}{\delta_m} = [1 + u^2 + 2Au]^{1/2} - 1 .$$

Expanding the square root gives

$$\frac{R_{\ell m} - \delta_m}{\delta_m} = \binom{1/2}{1} (u^2 + 2Au) + \binom{1/2}{2} (u^2 + 2Au)^2 + \binom{1/2}{3} (u^2 + 2Au)^3 + \dots , \quad (7.1)$$

where the binomial coefficients have the values

$$\begin{aligned} \binom{1/2}{1} &= \frac{1}{2} , & \binom{1/2}{2} &= -\frac{1}{8} , & \binom{1/2}{3} &= \frac{1}{16} , \\ \binom{1/2}{4} &= -\frac{5}{128} , & \binom{1/2}{5} &= \frac{35}{1280} , & \binom{1/2}{6} &= -\frac{105}{5120} . \end{aligned} \quad (7.2)$$

Expanding each power of $u^2 + 2Au$ in (7.1) and collecting equal powers of u gives

$$\frac{R_{lm} - \delta}{\delta} = \sum_{s=1}^{\infty} r_s u^s, \quad (7.3)$$

where

$$r_1 = \begin{pmatrix} 1/2 \\ 1 \end{pmatrix} \begin{pmatrix} 1 \\ 0 \end{pmatrix} 2A = A, \quad$$

$$r_2 = \begin{pmatrix} 1/2 \\ 2 \end{pmatrix} \begin{pmatrix} 2 \\ 0 \end{pmatrix} (2A)^2 + \begin{pmatrix} 1/2 \\ 1 \end{pmatrix} \begin{pmatrix} 1 \\ 1 \end{pmatrix} = \frac{1}{2} (1 - A^2), \quad$$

$$r_3 = \begin{pmatrix} 1/2 \\ 3 \end{pmatrix} \begin{pmatrix} 3 \\ 0 \end{pmatrix} (2A)^3 + \begin{pmatrix} 1/2 \\ 2 \end{pmatrix} \begin{pmatrix} 2 \\ 1 \end{pmatrix} (2A) = \frac{1}{2} A (-1 + A^2), \quad$$

$$r_4 = \begin{pmatrix} 1/2 \\ 4 \end{pmatrix} \begin{pmatrix} 4 \\ 0 \end{pmatrix} (2A)^4 + \begin{pmatrix} 1/2 \\ 3 \end{pmatrix} \begin{pmatrix} 3 \\ 1 \end{pmatrix} (2A)^2 + \begin{pmatrix} 1/2 \\ 2 \end{pmatrix} \begin{pmatrix} 2 \\ 2 \end{pmatrix}, \quad$$

$$= \frac{1}{8} (-1 + 6A^2 - 5A^4), \quad$$

$$r_5 = \begin{pmatrix} 1/2 \\ 5 \end{pmatrix} \begin{pmatrix} 5 \\ 0 \end{pmatrix} (2A)^5 + \begin{pmatrix} 1/2 \\ 4 \end{pmatrix} \begin{pmatrix} 4 \\ 1 \end{pmatrix} (2A)^3 + \begin{pmatrix} 1/2 \\ 3 \end{pmatrix} \begin{pmatrix} 3 \\ 2 \end{pmatrix} (2A), \quad$$

$$= \frac{1}{8} A [3 - 10A^2 + 7A^4], \quad$$

$$r_6 = \frac{1}{16} [1 - 15A^2 + 35A^4 - 21A^6]. \quad (7.4)$$

Expanding the powers of $(R_{lm} - \delta)/\delta$ gives the results displayed in Table I.

Table I. Values of the powers of $R_{\ell m} - \delta_{\ell m}$ used in deriving (7.5).

$$\begin{aligned}
\left(\frac{R_{\ell m} - \delta_{\ell m}}{\delta_{\ell m}} \right)^2 &= r_1^2 u^2 + 2r_1 r_2 u^3 + (r_2^2 + 2r_1 r_3) u^4 + 2(r_1 r_4 + r_2 r_3) u^5 + (r_3^2 + 2r_1 r_5 + 2r_2 r_4) u^6 + \dots \\
\left(\frac{R_{\ell m} - \delta_{\ell m}}{\delta_{\ell m}} \right)^3 &= r_1^3 u^3 + 3r_1^2 r_2 u^4 + 3(r_1^2 r_3 + r_1 r_2^2) u^5 + (r_2^3 + 3r_1^2 r_4 + 6r_1 r_2 r_3) u^6 + \dots \\
\left(\frac{R_{\ell m} - \delta_{\ell m}}{\delta_{\ell m}} \right)^4 &= r_1^4 u^4 + 4r_1^3 r_2 u^5 + 2(2r_1^3 r_3 + 3r_1^2 r_2^2) u^6 + \dots \\
\left(\frac{R_{\ell m} - \delta_{\ell m}}{\delta_{\ell m}} \right)^5 &= r_1^5 u^5 + 5r_1^4 r_2 u^6 + \dots \\
\left(\frac{R_{\ell m} - \delta_{\ell m}}{\delta_{\ell m}} \right)^6 &= r_1^6 u^6 + 6r_1^5 r_2 u^7 + \dots
\end{aligned}$$

Multiplying each $[(R_{\ell m} - \delta_{\ell m})/\delta_{\ell m}]^p$ by $(-1)^p (p! \rho^p)^{-1}$ and summing gives

$$\mathcal{K} = C \sum_{n=2}^{\infty} h_n u^{n+1}, \quad (7.5)$$

where

$$C = \frac{3 B a_{nn}^3 \rho^2}{1 - 2\rho}$$

and

$$h_1 = \frac{r_1^2}{2! \rho^2} = \frac{A^2}{2! \rho^2},$$

$$h_2 = -\frac{r_1^3}{3! \rho^3} + \frac{2 r_1 r_2}{\rho^2 2!} = -\frac{1}{3! \rho^3} (A^3 + 3\rho A^3 - 3\rho A),$$

$$h_3 = \frac{r_1^4}{4! \rho^4} - \frac{3 r_1^2 r_2}{3! \rho^3} + \frac{r_2^2 + 2 r_1 r_3}{2! \rho^2},$$

$$= \frac{1}{4! \rho^4} [A^4 + 3\rho(5\rho + 2)A^4 - 6\rho(1 + 3\rho)A^2 + 3\rho^2],$$

$$h_4 = -\frac{r_1^5}{5! \rho^5} + \frac{4 r_1^3 r_2}{4! \rho^4} - \frac{3(r_1^2 r_3 + r_2^2 r_1)}{3! \rho^3} + \frac{2(r_1 r_4 + r_2 r_3)}{2! \rho^2}$$

$$= \frac{1}{5! \rho^5} [-A^5 + 5\rho(2 - 9\rho - 21\rho^2)A^5$$

$$- 10\rho(1 - 6\rho - 15\rho^2)A^3 - 15\rho^2(1 + 3\rho)A],$$

$$\begin{aligned}
h_5 &= \frac{1}{6! \rho^6} [r_1^6 - 30\rho r_1^3 r_2 + 30\rho^2 (r_1^3 r_3 + 6r_1^2 r_2^2 + 3r_1^3 r_3) \\
&\quad - 120\rho^3 (3r_1^2 r_4 + 6r_1 r_2 r_3 + r_2^3) + 360\rho^4 (2r_1 r_5 + 2r_2 r_4 + r_3^2)] \\
&= \frac{1}{6! \rho^6} [A^6 (1 + 1155\rho^4 + 450\rho^3 - 120\rho^2 - 15\rho) \\
&\quad + A^4 (-1875\rho^4 - 675\rho^3 + 240\rho^2 + 15\rho) A^2 (765\rho^4 + 270\rho^3 + 180\rho^2) \\
&\quad + (45\rho^4 - 15\rho^3)] .
\end{aligned} \tag{7.6}$$

The first term,

$$\pm \frac{1}{(n+1)! \rho^{n+1}} A^{n+1} ,$$

in each h_n in (7.6) corresponds to the value used in the previous sections.

It is tempting to approximate $A \equiv \hat{\delta}_m \cdot \hat{u}_{\ell m}$ by $1/\sqrt{3}$ in (7.6) and calculate the ratio of h_n to the first term in h_n . The results of the previous sections could then be multiplied by the square of this ratio in order to approximate the effect of the additional terms. Indeed, this increases the value of $(\beta_{n+1})_{\text{mx}} / (\beta_n)_{\text{mx}}$ by a factor of approximately 3.7 for small n , giving better agreement with experiment. However, this result probably is not correct since considerable care must be exercised in approximations of this type. For example, if A is approximated by $1/3$ rather than by $1/\sqrt{3}$, the value of $(\beta_{n+1})_{\text{mx}} / (\beta_n)_{\text{mx}}$ changes erratically with increasing n .

From \mathcal{H}_2 in (7.6) it is seen that replacing A^3 by

$$A^3 + 3\rho A^3 - 3\rho A \quad (7.7)$$

takes into account all terms in \mathcal{K}_2 [in (2.5)]. Thus, $(\hat{\delta}_m \cdot \underline{u}_{lm})^3$ in (2.7) is replaced by

$$(1 + 3\rho)(\hat{\delta}_m \cdot \underline{u}_{lm})^3 - 3\rho(\hat{\delta}_m \cdot \underline{u}_{lm})(\underline{u}_{lm} \cdot \underline{u}_{lm}) .$$

The corresponding value of α_2 in (2.16) is replaced by

$$\begin{aligned} \alpha_2 = \sum_{m=1}^6 \left\{ (1+3\rho)(\hat{\delta}_m \cdot \hat{u}_f) U_m(Q_1) U_m(Q_2) \right. \\ \left. - \rho(\hat{\delta}_m \cdot \hat{u}_f) \underline{u}_m(Q_1) \cdot \underline{u}_m(Q_2) \right. \\ \left. - 2\rho U_m(Q_1) [\hat{u}_f \cdot \underline{u}_m(Q_2)] \right\} . \end{aligned} \quad (7.8)$$

For $\hat{u}_f = \hat{x}$, (7.8) gives

$$\begin{aligned} \alpha_2 = U_x(Q_1) U_x(Q_2) - \rho U_x(Q_1) U_y(Q_2) \\ - \rho U_z(Q_1) U_x(Q_2) - 2\rho U_y(Q_1) U_y(Q_2) \\ - 2\rho U_z(Q_1) U_z(Q_2) - cc . \end{aligned} \quad (7.9)$$

Notice that the coefficient of $U_x(Q_1)U_x(Q_2)$ from the extra terms $[3\rho A^3 - 3\rho A$ in (7.7)] vanishes. This is a general property of α_n for $n \geq 2$ resulting from the fact that all $r_n = 0$ when $A = 1$ for $n \geq 2$. See (7.4).

For α_3 , $(\hat{\delta}_m \cdot \underline{u}_{\ell m})^4$ in (2.7) is replaced by [see \mathcal{H}_3 in (7.6)]

$$[1+3\rho(5\rho+2)](\hat{\delta}_m \cdot \underline{u}_{\ell m})^4 - 6\rho(1+3\rho)(\hat{\delta}_m \cdot \underline{u}_{\ell m})(\underline{u}_{\ell m} \cdot \underline{u}_{\ell m}) \\ + 3\rho^2(\underline{u}_{\ell m} \cdot \underline{u}_{\ell m})(\underline{u}_{\ell m} \cdot \underline{u}_{\ell m}) .$$

The corresponding value of α_3 in (2.15) is

$$\alpha_3 = \sum_{m=1}^6 \left\{ [1+3\rho(5\rho+2)](\hat{\delta}_m \cdot \hat{u}_f) U_m(Q_1) U_m(Q_2) U_m(Q_3) \right. \\ - 3\rho(1+3\rho)(\hat{\delta}_m \cdot \hat{u}_f) U_m(Q_1) [\underline{u}_m(Q_2) \cdot \underline{u}_m(Q_3)] \\ - 3\rho(1+3\rho) U_m(Q_1) U_m(Q_2) [\hat{u}_f \cdot \underline{u}_m(Q_3)] \\ \left. + 3\rho^2[\underline{u}_f \cdot \underline{u}_m(Q_1)][\underline{u}_m(Q_2) \cdot \underline{u}_m(Q_3)] \right\} . \quad (7.10)$$

For $\hat{u}_f = \hat{x}$, (7.10) gives

$$\begin{aligned}
 \alpha_3 = & U_x(Q_1) U_x(Q_2) U_x(Q_3) - 3\rho(1+2\rho) [U_x(Q_1) U_x(Q_2) U_x(Q_3) \\
 & + U_x(Q_1) U_x(Q_2) U_z(Q_3) + U_y(Q_1) U_y(Q_2) U_y(Q_3) \\
 & + U_z(Q_1) U_z(Q_2) U_z(Q_3)] + 3\rho^2 [U_y(Q_1) U_y(Q_2) U_y(Q_3) \\
 & + U_y(Q_1) U_y(Q_2) U_z(Q_3) + U_z(Q_1) U_z(Q_2) U_z(Q_3) \\
 & + U_z(Q_1) U_z(Q_2) U_y(Q_3)] . \quad (7.11)
 \end{aligned}$$

These results (7.9) and (7.11) are being used in the computer analyses, to be discussed in a later report.

VIII. Higher-Order Processes In The n-Phonon Region

In this section it will be shown for NaCl at room temperature that the higher-order processes shown in Figs. 2b, 2c, 12, 13, 14, and 15 are negligible for reasonable values of n . The results suggest that higher-order processes may be negligible for values of n of current interest, say $n \lesssim 8$. Additional analyses will be made elsewhere to establish the validity of this suggestion.

The process shown in Fig. 12a will be called the single-vertex, n-phonon process. Processes with more than one vertex will be called higher-order processes. For $n = 2$ there are no higher-order processes except those of the type in Fig. 12b, which can be accounted for simply by renormalizing the phonons.

For $n = 3$, the only higher-order process of interest is shown in Fig. 12c. The contribution to β_3 can be obtained simply as follows: By standard perturbation theory, the matrix element for the process in Fig. 13a (with vertices a_Q , not $A_Q \equiv a_{\mathbf{k}b} + a_{-\mathbf{k}b}^\dagger$) is

$$\begin{aligned} \langle f n | \mathcal{K}_{ab+} | i \rangle = \sum_{Q_m} 4 \langle 1^+ 2^+ 3^+ f^- | \Delta(\mathbf{K}_b) V_{m23} a_m a_2^\dagger a_3^\dagger | 1^+ m^+ f^- \rangle \\ \times \langle 1^+ m^+ f^- | \Delta(\mathbf{K}_a) V_{fm1} a_f a_m^\dagger a_1^\dagger | 1^0 2^0 3^0 m^0 f^0 \rangle / \hbar(\omega - \omega_1 - \omega_m) \end{aligned} \quad (8.1)$$

where $|1^\pm\rangle \equiv |n_1 \pm 1\rangle$, $|m^0\rangle \equiv |n_m\rangle$, etc., and permutations of 2 and 3 and of m and 1 in \mathcal{K} give the factor of 4. Evaluating the sum on \mathbf{k}_m in (8.1) by using $\Delta(\mathbf{K}_a)$ and using the well known values of the matrix elements gives

$$\frac{\langle f n | \mathcal{K}_{ab+} | i \rangle}{\langle f n | \mathcal{K}_3 | i \rangle} = \sum_{b_m} \frac{2}{3} \frac{(n_m + 1) V_{m23} V_{fm1}}{\hbar(\omega - \omega_1 - \omega_m) V_{f123}} \quad (8.2)$$

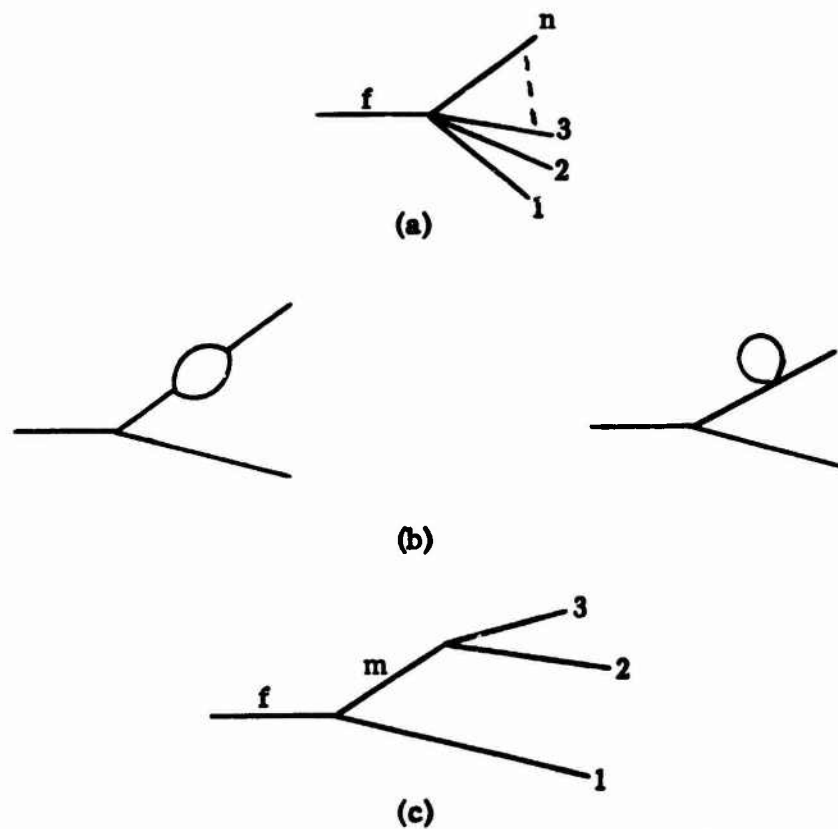


Fig. 12. Phonon relaxation processes: (a) single-vertex, n -phonon process; (b) processes with renormalized phonon lines; (c) three-phonon - summation higher-order process.

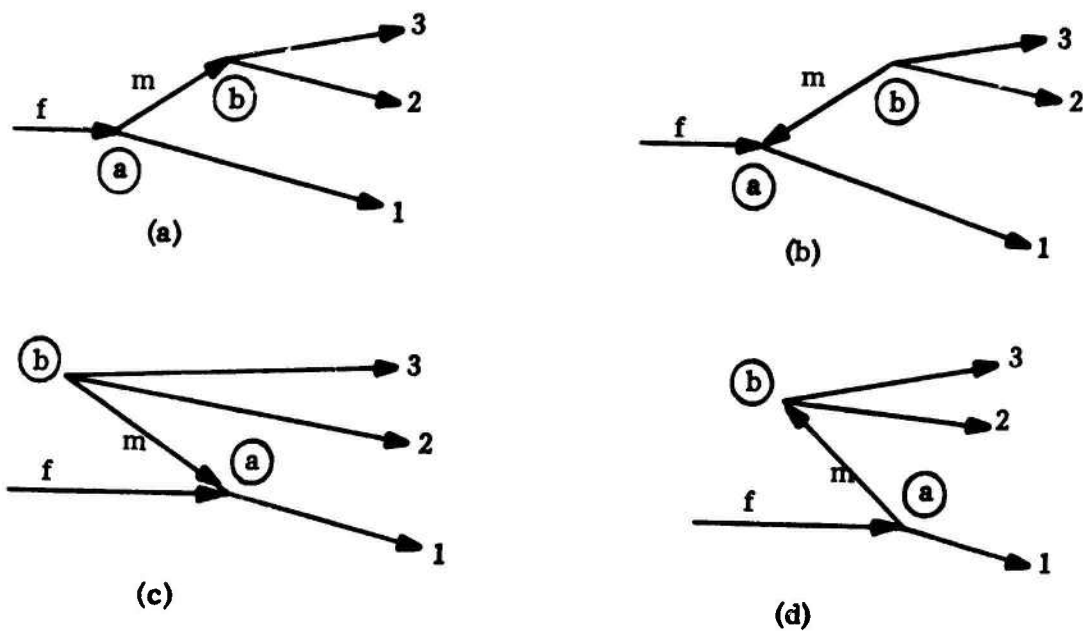
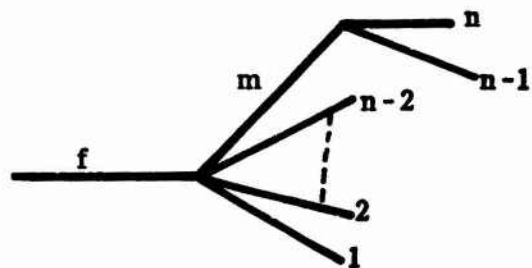
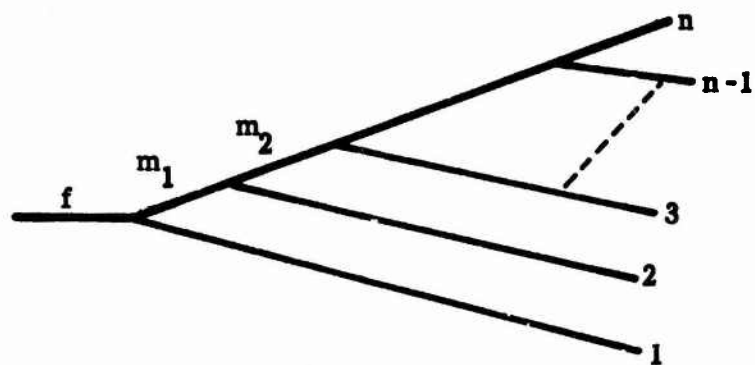


Fig. 13. Various time orderings of the process shown in Fig. 12(c).

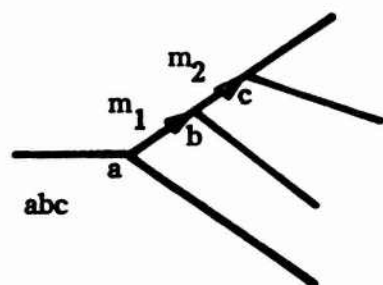


(a)

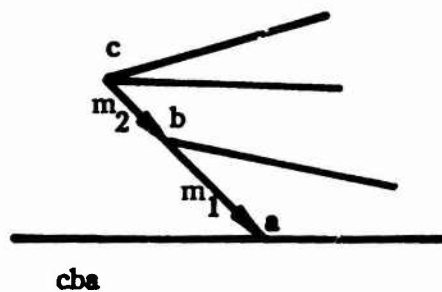


(b)

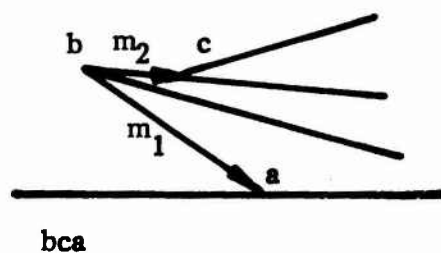
Fig. 14. Two-vertex, n -phonon process (a) and $(n-1)$ -vertex, n -phonon process (b).



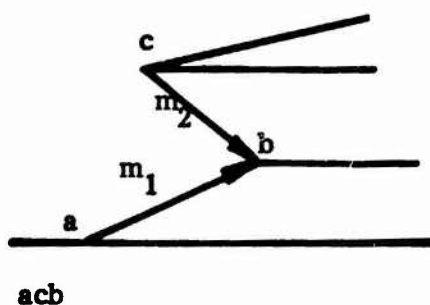
(a)



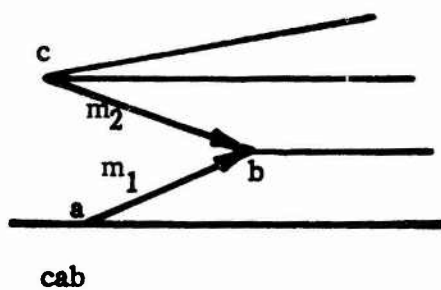
(b)



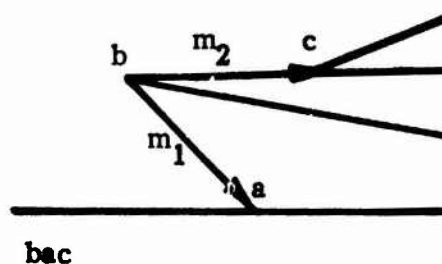
(c)



(d)



(e)



(f)

Fig. 15. Various time orderings of the process shown in Fig. 14(b) for $n = 4$.

where

$$\langle f_n | \mathcal{K}_3 | i \rangle = \langle 1^+ 2^+ 3^+ f^- | \Delta(K_b) V_{f123} a_1^\dagger a_2^\dagger a_3^\dagger a_f | 1^0 2^0 3^0 f^0 \rangle .$$

The diagram in Fig. 13b gives the same result as (8.2), but with ω_m replaced by $-\omega_m$ and $n_m + 1$ replaced by n_m

The contribution from the diagram in Fig. 13c is

$$\frac{\langle f_n | \mathcal{K}_{ba+} | i \rangle}{\langle f_n | \mathcal{K}_3 | i \rangle} = \sum_{b_m} \frac{2(n_m + 1) V_{m23} V_{fm1}}{-3\hbar(\omega - \omega_1 + \omega_m) V_{f123}} \quad (8.3)$$

and the contribution from the diagram in Fig. 13d is the same as (8.3), but with ω_m and $n_m + 1$ replaced by $-\omega_m$ and n_m , respectively.

Adding these four terms gives

$$\frac{\langle f_n | \mathcal{K}_{3-22} | i \rangle}{\langle f_n | \mathcal{K}_3 | i \rangle} = \sum_{b_m} \frac{4\omega_m V_{fm1} V_{m23}}{3\hbar[(\omega - \omega_1)^2 - \omega_m^2] V_{f123}} \quad (8.4)$$

The value of this ratio in the three-phonon region, say at $\omega = 3.5 \bar{\omega}$ [see (5.5)] is of interest. With this value of ω and with $\omega_1 = \bar{\omega}$ and $\omega_m \leq \bar{\omega}$, (8.4) reduces to

$$\frac{\langle f_n | \mathcal{K}_{3-22} | i \rangle}{\langle f_n | \mathcal{K}_3 | i \rangle} \cong \frac{4}{15.75} \frac{1}{\hbar \bar{\omega}^2} \sum_{b_m} \frac{\omega_m V_{fm1} V_{m23}}{V_{f123}} . \quad (8.5)$$

The value of $V_{f123} \equiv V_{fQ_1Q_2Q_3}$ is given in (2.15). This result (2.15) is also valid for $V_{1,2 \dots (n+1)}$ when written in the form:

$$V_{1,2 \dots n+1} = \pm \frac{3\rho \sqrt{\hbar}}{\sqrt{2} (1-2\rho)} \alpha'_n \frac{B a_{nn}^2}{n! N^{\frac{1}{2}} (n-1)} \frac{1}{(\omega_{Q_1} \dots \omega_{Q_{n+1}})^{1/2}} \\ \times \frac{1}{\sqrt{m_{<}}} \left(\frac{\hbar}{2\rho^2 m_{<} a_{nn}^2} \right)^{n/2} \quad (8.6)$$

where

$$\alpha'_n = \sum_{p=1}^6 U_{1p} \times \dots \times U_{(n+1)p} \quad (8.7)$$

with

$$U_{fp} = \hat{\delta}_p \cdot \hat{u}_f \left(\frac{m_{<}}{m_r} \right)^{1/2}.$$

Substituting (2.15) and (8.6) into (8.5) gives

$$\frac{\langle fn | \mathcal{K}_{3-22} | i \rangle}{\langle fn | \mathcal{K}_3 | i \rangle} = \frac{6}{10.5} \frac{1}{1-2\rho} \frac{B a_{nn}}{\bar{\omega}^2} \left(\frac{1}{m_{<} m_{>}} \right)^{1/2} \sum_{b_m} \frac{\alpha_{2fm1} \alpha_{2m23}}{\alpha_{3f123}}. \quad (8.8)$$

In evaluating the sum over b_m in (8.8), it will be assumed that the quasi-selection rule that the matrix element for the splitting of a fundamental phonon into two optical or two acoustical phonons in NaCl-structure crystals is negligibly small. Wavevector conservation of the three output phonons will be

neglected formally, and the value of $\langle f_n | \mathcal{H}_{3-22} | i \rangle / \langle f_n | \mathcal{H}_3 | i \rangle$ will be computed at $\omega = 3.5 \bar{\omega}$, assuming that

$$\omega_1 = \omega_2 = \omega_3 = \bar{\omega} \quad (8.9)$$

for the three output phonons. For NaCl, the three output phonons are longitudinal optical (LO) phonons. Thus, the quasi-selection rule requires that the intermediate phonon m be an acoustical phonon. The case of m being a longitudinal acoustical (LA) phonon will be considered. Since $b_m = \text{LA}$ and $b_1 = \text{LO}$, α_{2fm1} from (3.2) can be approximated by (3.9). From this same equation (3.9), with $\hat{\delta}_p \cdot \hat{u}_f$ replaced by $(m_r/m_<)^{1/2} U_{mp}$ to account for the fact that α_{2m23} does not involve the fundamental mode,

$$\begin{aligned} \alpha_{2m23} = & \left(\frac{m_r}{m_<} \right)^{1/2} \left(u_{<k_n \text{ LA } x} - \sqrt{\frac{m_<}{m_>}} u_{>k_m \text{ LA } x} e^{i k_{mx} a_{nn}} \right) \\ & \times \left(u_{<k_2 \text{ LO } x} - \sqrt{\frac{m_<}{m_>}} u_{>k_2 \text{ LO } x} e^{i k_{2x} a_{nn}} \right) \\ & \times \left(u_{<k_3 \text{ LO } x} - \sqrt{\frac{m_<}{m_>}} u_{>k_3 \text{ LO } x} e^{i k_{3x} a_{nn}} \right) - \text{cc} . \end{aligned} \quad (8.10)$$

As in Sec. III, we set $u_{<\text{LO } x} = 1/\sqrt{3}$, $u_{>\text{LO } x} = 0$, $u_{<\text{LA } x} = 0$, and $u_{>\text{LA } x} = 1/\sqrt{3}$. These values, with (8.10) and $\sin^2 k_{mx} a_{nn} = \frac{1}{2}$ formally, give

$$|\alpha_{2m23}|^2 \cong \frac{2}{27} \frac{m_r}{m_>} . \quad (8.11)$$

Next consider the value of α_{3f123} . The same arguments that gave (8.11) indicate that

$$|\alpha_{3f123}|^2 \cong \frac{4}{27} \quad (8.12)$$

is a reasonable approximation. Substituting (3.9), (8.11), and (8.12) into (8.8) gives

$$\begin{aligned} \left| \frac{\langle fn | \mathcal{K}_{3-22} | i \rangle}{\langle fn | \mathcal{K}_3 | i \rangle} \right|_{LO LA} &= \left[\frac{1}{20.7} \left(\frac{1}{1-2\rho} \frac{B_{ann}}{\bar{\omega}_m^2} \right)^2 \frac{m_{<}^2 m_r}{m_{>}^3} \right]^{1/2} \\ &= 1.0 \times 10^{-2} . \end{aligned} \quad (8.13)$$

Even if the other two acoustical intermediate states contribute as much as the LA state, the total ratio in (8.13) is increased only by a factor of 3, giving 3×10^{-2} for the value of this ratio. Thus, the order-of-magnitude calculation suggests that the higher-order processes are negligible in NaCl for $n = 3$.

In considering larger values of n , several classes of diagrams can be studied. First consider the n -phonon diagram in Fig. 14a. The energy denominator corresponding to $(\omega - \omega_1)^2 - \omega_m^2$ in (8.4) is

$$(\omega - \omega_1 - \omega_2 - \cdots - \omega_{n-2})^2 - \omega_m^2$$

Assuming that $\omega = (n + \frac{1}{2})\bar{\omega}$ and $\omega_1 = \omega_2 = \cdots = \omega_{n-1} = \omega_m = \bar{\omega}$, this energy denominator reduces to

$$\left[n + \frac{1}{2} \bar{\omega} - (n-2) \bar{\omega} \right]^2 - \bar{\omega}^2 = 5.25 \bar{\omega}^2 .$$

The rest of the analysis is the same as that leading to (8.8), and the results are the same as (8.8) with the appropriate changes in the matrix elements:

$$\frac{\langle fn | \mathcal{K}_{n-2(n-1)} | i \rangle}{\langle fn | \mathcal{K}_n | i \rangle} = \frac{6}{10.5} \left(\frac{n}{3} \right) \frac{1}{1-2\rho} \frac{B_{a_{nn}}}{\omega^2} \left(\frac{1}{m_{< m_{>}}} \right)^{1/2} \sum_{b_m} \frac{\alpha_{(n-1)fm1 \dots} \alpha_{2mn n-1}}{\alpha_{nf12 \dots n}} \quad (8.14)$$

The value of $\alpha_{2mn n-1}$ is given by (8.11):

$$|\alpha_{2mn n-1}|^2 = \frac{2}{27} \frac{m_r}{m_{>}} \quad (8.15)$$

With all output phonons $1 \dots n$ as LO phonons and the intermediate phonon as a LA phonon, the arguments leading to (3.9) indicate that

$$|\alpha_{nf12 \dots n}|^2 \cong \frac{4}{3^n}, \quad |\alpha_{(n-1)fm1 \dots}|^2 \cong \frac{8}{3^n} \frac{m_{<}}{m_{>}}, \quad (8.16)$$

are reasonable approximations. A factor of $2/3$ was included in (8.16) as discussed in Sec. III. From (8.14)-(8.16) with $\sum_{b_m} = 3$ formally,

$$\left| \frac{\langle fn | \mathcal{K}_{n-2(n-1)} | i \rangle}{\langle fn | \mathcal{K}_n | i \rangle} \right|^2 \cong \frac{1}{20.7} \left(\frac{n}{3} \right)^3 \left(\frac{1}{1-2\rho} \frac{B_{a_{nn}}}{\omega^2 m_{<}} \right)^2 \frac{m_{<}^2 m_r}{m_{>}^3}. \quad (8.17)$$

This result (8.17) is $(n/3)^2$ times larger than the $n = 3$ result (8.13). The ratio in (8.17) is equal to unity for $n = 190$. Thus, it is clear that the contribution to β from the diagram in Fig. 14a is negligible.

Next consider the diagram in Fig. 14b. For $n = 3$, this diagram reduces to that of Fig. 12c, and the matrix element is given by (8.13). For larger values of n , a straightforward evaluation of the sums over the diagrams corresponding to those in Fig. 13 would be tedious. A simple method of evaluating the sums is first illustrated for $n=3$. Since the ratio $\langle fn | \mathcal{H}_{3-22} | i \rangle / \langle fn | \mathcal{H}_3 | i \rangle$ is independent of temperature, all occupation numbers, such as n_m in (8.2), must sum to zero. Thus, only terms containing factors of $(n+1)$ need be considered. For example, the diagrams in Figs. 13(a) and (c) are considered, and those in Figs. 13(b) and (d) are dropped. [For the m arrow going from left to right, the term $a_m a_m^\dagger$ gives rise to $n_m + 1$, while the m arrow going from right to left corresponds to $a_m^\dagger a_m = n_m$.]

Since the sum over the four diagrams contains the factor ω_m , the energy denominators can be expanded, and only the ω_m terms retained. For example, the energy denominator corresponding to Fig. 13(a) is

$$\begin{aligned} \frac{1}{\omega - \omega_1 - \omega_m} &= \frac{1}{\omega - \omega_1} + \frac{\omega_m}{(\omega - \omega_1)^2} + \dots \\ &= \frac{\omega_m}{(\omega - \omega_1)^2} + \dots \end{aligned} \quad (8.18)$$

and that for Fig. 13(c) is

$$\frac{1}{-(\omega - \omega_1 + \omega_m)} = -\frac{1}{\omega - \omega_1} + \frac{\omega_m}{(\omega - \omega_1)^2} + \dots = \frac{\omega_m}{(\omega - \omega_1)^2} + \dots \quad (8.19)$$

For large n , $n + \frac{1}{2} \cong n$. Thus we set $\omega = (n + \frac{1}{2}) \bar{\omega} \cong n \bar{\omega}$, or $\omega = 3 \bar{\omega}$ for $n = 3$ in anticipation of the large values of n of interest. Adding (8.18) and (8.19) and using $\omega \cong 3 \bar{\omega}$ and $\omega_1 \cong \bar{\omega}$ gives

$$\frac{2 \omega_m}{(3.5 - 1)^2 \bar{\omega}^2} \quad (8.20)$$

which corresponds to

$$\frac{2 \omega_m}{(\omega - \omega_1)^2 - \omega_m^2} \quad (8.21)$$

in (8.4). For large n , the factor ω_m^2 in the denominator of (8.21) is negligible, and (8.20) and (8.21) are equivalent. To shorten the notation further, set $\omega = 3 \omega_g$, $\omega_1 = \omega_g$ and $\omega_m \equiv m \omega_g$ in (8.18) and (8.19). This reduces (8.18) and (8.19) to

$$\frac{1}{2-m} = \frac{m}{4} + \dots$$

$$\frac{1}{-(2+m)} = \frac{m}{4} + \dots$$

and the sum is to $2m/4$, which can be written as

$$\frac{2m}{4} = \frac{2m}{(2!)^2} \quad (8.22)$$

For $n = 4$, a straightforward evaluation of the sum over the energy denominators of the 24 diagrams gives

$$\frac{\omega_{m_1} \omega_{m_2}}{9 \bar{\omega}^4} \rightarrow \frac{m_1 m_2}{9} = \frac{(2)^2 m_1 m_2}{(3!)^2} \quad (8.23)$$

This result (8.23) can be obtained by the method above as follows: The energy denominators corresponding to the diagrams in Figs. 15(a)-(f) are, respectively

$$\frac{1}{(3-m_1)(2-m_2)} = \frac{1}{6} \left(1 - \frac{1}{3} m_1\right)^{-1} \left(1 - \frac{1}{2} m_2\right)^{-1} = \frac{1}{6^2} m_1 m_2 + \dots$$

$$\frac{1}{(3+m_1)(2+m_2)} = \frac{1}{6} m_1 m_2 + \dots$$

$$\frac{1}{(3+m_1)(1+m_1+m_2)} = \left(\frac{1}{9} + \frac{2}{3}\right) m_1 m_2 + \dots$$

$$\frac{1}{(3-m_1)(1-m_1-m_2)} = \left(\frac{1}{9} + \frac{2}{3}\right) m_1 m_2 + \dots$$

$$-\frac{1}{(2+m_2)(1-m_1-m_2)} = \left(\frac{1}{4} - 1\right) m_1 m_2 + \dots$$

$$-\frac{1}{(2-m_2)(1+m_1+m_2)} = \left(\frac{1}{4} - 1\right) m_1 m_2 + \dots$$

Adding these six terms gives $(2)^2 m_1 m_2 / (3!)^2$ in agreement with (8.23).

For $n = 5$, adding the 24 terms gives

$$\frac{2^3 m_1 m_2 m_3}{(4!)^2}$$

By induction, for general n the corresponding result is

$$\frac{2^{n-2} m_1 m_2 \dots m_{n-2}}{[(n-1)!]^2} \quad (8.24)$$

Thus

$$\frac{\langle f_n | \mathcal{H}_{n-22} \dots | i \rangle}{\langle f_n | \mathcal{H}_n | i \rangle} = \pm \frac{2^{n-2}}{[(n-1)!]^2} \frac{1}{(f_n \bar{\omega}^2)^{n-2}} \sum_{b_{m_1}} \dots \sum_{b_{m_{n-2}}} \omega_{m_1} \dots \omega_{m_{n-2}} \\ \times \frac{V_{f1m_1} V_{m_1 m_2}^2 \dots V_{m_{n-2}(n-1)n}}{V_{f12} \dots n} \quad (8.25)$$

Substituting (2.15) and (8.6) into (8.25) gives

$$\frac{\langle f_n | \mathcal{H}_{n-22} \dots | i \rangle}{\langle f_n | \mathcal{H}_3 | i \rangle} = \pm \frac{n}{2(n-1)!} \left[\frac{3}{2(1-2\rho)} \frac{B a_m}{m \bar{\omega}^2} \right]^{n-2} \\ \times \sum_{b_{m_1}} \dots \sum_{b_{m_{n-2}}} \frac{\alpha_{2f1m_1} \alpha_{2m_1 m_2}^2 \dots \alpha_{2m_{n-2}(n-1)n}}{\alpha_{nf12} \dots n} \quad (8.26)$$

For $n = 3$, the numerical coefficient $9/8$ in (8.26) is slightly different from the corresponding value $9/10.5$ from (8.8). The difference is that ω_m^2 in (8.21) was not neglected in the derivation of (2.15) and $n + \frac{1}{2}$ was not approximated by n .

The values of the multiple sum in (8.26) can be estimated by formally setting

$$\sum_{b_{m_1}} \dots \sum_{b_{m_{n-2}}} = (3)^{n-2}$$

and using (8.11) and (8.16), which gives

$$\left| \frac{\langle f_n | \mathcal{H}_{3-22 \dots} | i \rangle}{\langle f_n | \mathcal{H}_3 | i \rangle} \right|^2 \cong \frac{n}{24(n-1)!} \left(\frac{3\sqrt{2}}{2(1-2\rho)} \frac{B a_{nn}}{m \bar{\omega}^2} \right)^{2n-4} \quad (8.27)$$

Since the value of the ratio in (8.27) decreases with increasing n and is negligible for $n = 3$, the order of magnitude calculation suggests that the contribution to β from the diagrams in Fig. 14b is negligible.

Although the temperature and frequency dependence of β for the higher-order processes is of academic interest only since these processes are negligible, it is mentioned that the frequency dependence of the higher-order processes is different from that of the single-vertex process. The formal expression for the temperature dependence of the higher-order phonon processes is the same as that of the single-vertex n -phonon process. However, wave-vector conservation in the intermediate states may cause the final-state phonons to be different in the single-vertex and higher-order processes, thus giving some difference in the temperature dependence of the two types of processes. Furthermore, the factors B , a_{nn} , and $\bar{\omega}$ in (8.27) are temperature dependent. At the present state of knowledge (of the phonon dispersion relations and the coefficients in the scattering Hamiltonian, for example) these temperature differences could not be used to distinguish between the two types of processes.

IX. Anharmonic-Einstein-Oscillator Model

A study of the absorption of electromagnetic radiation by a collection of non-interacting but anharmonic oscillators has been initiated as an alternate approach to the multiphonon absorption problem. A preliminary report of the results is presented here. A complete presentation will be given in a future report.

Since most of the experimental measurements of interest to this study have been carried out at room temperature or higher, purely classical methods were used. The first step was to derive an expression for the absorption coefficient of the oscillator array, assuming the system in thermal equilibrium at temperature T . The resulting general form may be applied easily and quickly to compute the absorption coefficients for a number of anharmonic potentials of physical interest.

The Liouville equation for the classical distribution function $\rho(q, p, t)$ of the oscillator array in the presence of a spatially uniform driving field of frequency ω was treated by perturbation theory to obtain a classical form of the well known Kubo formula for the absorption coefficient. The Kubo formula was then reduced to a form that may readily be computed once the nature of the particle orbit in the anharmonic potential is known. The final form is particularly convenient for use in the quasi-harmonic region, where anharmonic corrections to the particle orbit are small. This is the temperature region of interest in the discussion of both solids below their melting temperature, and for molecular gases below the temperature at which dissociation occurs.

The formula was applied to the case of particles whose motion is governed by the Morse potential, an anharmonic potential used frequently in molecular physics. In this quasi-harmonic region, we obtain a particularly simple result for the absorption coefficient. If the fundamental vibration frequency of the molecule is ω_0 , then the intensity of the n^{th} harmonic absorption at $\omega_n = n\omega_0$ is given by the simple expression

$$P_n = n! \left(\frac{kT}{D} \right)^{n-1} P_1$$

where D is the dissociation energy, and P_1 the strength of the fundamental absorption line at ω_0 . For temperatures near room temperature, $kT \ll D$, and a plot of P_n against n gives a form very close to the exponentially decaying form observed in many crystalline materials.

Mangir and Hellwarth¹⁵ have treated the same problem from a quantum mechanical point of view and obtained a result that reduces to ours in the correspondence-principle limit $\hbar \rightarrow 0$. A detailed comparison between our calculation and theirs should prove most illuminating.

We believe a form similar to the result quoted above will very likely emerge for large n from the study of any potential for which the deviations of the small-amplitude motions from the harmonic approximation are small. It is interesting to contrast this near-exponential behavior with that appropriate to a potential for which the harmonic approximation cannot be applied. An example of such a potential would be a simple square-well potential, with a flat bottom and infinitely steep sides. Applying the method to this problem indicates that at high frequencies the absorption does not fall off in a near exponential manner,

but rather as $1/\omega^2$. We plan to examine two or three more potential functions to see whether or not one can make a clear systematic statement about the relation of the form of the potential function, and the frequency dependence of the absorption coefficient at high frequencies.

The comparison between the results for the Morse potential and the square well leads us to conjecture about the possible role of certain impurities in increasing the linear absorption coefficient of crystals above the value expected for the intrinsic processes apparently responsible for the near-exponential tail at high frequencies. It is well known that in the alkali halides, certain impurities (Li and Ag, as examples) move in potential wells that are very flat, since very low, strongly temperature-dependent frequencies are associated with these impurities. It may be that the presence of these impurities will give contributions to the absorption coefficient which falls off like ω^{-2} rather than exponentially with frequency. Consequently, at high frequencies, the value of the absorption coefficient may be greatly affected by these impurities.

The results obtained to date will enable us to make semi-quantitative estimates of the impurity concentrations required to give rise to a given value of the absorption coefficient. The simplicity of the method may make it useful in other problems, such as examining nonlinear absorption mechanisms.

C. THEORY OF INFRARED ABSORPTION AND MATERIAL FAILURE IN CRYSTALS CONTAINING INCLUSIONS

Small amounts of macroscopic inclusions in or on the surface of a nonabsorbing host crystal, in some cases a fractional volume of $\sim 10^{-7}$ to 10^{-8} , can give rise to a value of the optical absorption coefficient β of 10^{-4} cm^{-1} (a typical value of current interest). For various types of inclusions, the frequency dependence of β ranges from increasing as ω^2 , to independent of ω , to exponentially decreasing with ω . The temperature dependence ranges from independent of T to increasing as T^p in the high-temperature limit, where $p \cong 2 - 4$ typically. Simple expressions for the absorption cross section are derived for various cases of practical interest. The cross sections are used to derive expressions for β for the four cases of large inclusions of strong and weak absorbers and of small inclusions of dielectric and metallic particles. A result of general interest in the theory of scattering is that the absorption cross section of large spheres is equal to $(1 - R_{\perp})\pi a^2$, where R_{\perp} is the reflection coefficient for normal incidence, rather than $(1 - \langle R \rangle)\pi a^2$, where $\langle R \rangle$ is the geometric-optics average reflection over the illuminated hemisphere. The material failure resulting from local heating of macroscopic inclusions is a far greater problem in high-intensity short-pulse systems than in low-intensity long-pulse or cw systems having equal average intensity. Microsecond pulses with energy densities as low as $\sim 5 \text{ J/cm}^2$ can cause material failure.

I. Introduction

Several theoretical studies of intrinsic infrared absorption are currently underway.^{15-17a,1,3} It is expected that the results of these studies, especially in conjunction with experimental investigations, will afford estimates of the values of β for various materials that could be approached by removing the extrinsic sources of absorption. The present investigation is concerned with another aspect of the problem -- that of extrinsic absorption by macroscopic inclusions. Since the inclusions may be either in the bulk of the crystals or on their surfaces, the results are of interest in surface studies as well as studies of bulk properties.

Absorption is of greater interest than scattering in the study of high-power infrared windows. A value of $\beta = 10^{-4} \text{ cm}^{-1}$ for the absorption coefficient can cause sufficient heating for the system to fail, for example, by thermal defocusing or by window fracture.¹⁸⁻²⁰ But an equal amount of scattering $\beta_{\text{scat}} = 10^{-4} \text{ cm}^{-1}$ may be tolerable. Thus, scattering will be neglected here, except to mention that the observation of the associated scattering may help to identify the absorption mechanism in some cases. Winsor²¹ has shown theoretically that scattering, especially in conjunction with total internal reflection at the host crystal boundaries, may increase the measured value of β by increasing the path lengths of the rays in the crystal.

There is great interest²² in lowering the value of β for candidate materials for high-power infrared windows. Materials of current interest include ZnSe, CdTe, KCl, KBr, and TI 1173 glass ($\text{Ge}_{28}\text{Sb}_{12}\text{Se}_{60}$). Results, such as

those presented here, concerning the magnitude and the temperature and frequency dependence of β for extrinsic and intrinsic processes are needed in the material-improvement programs. The effects of inclusions on absorption in the infrared have not been studied experimentally. Such experimental studies would be welcomed.

It has been realized for some time that windows in high-power infrared laser systems can cause the system to fail with or without actual mechanical failure of the window.¹⁸⁻²⁰ Examples are thermally induced fracture of the window material and thermal defocusing of the laser beam by the window resulting from uneven heating of the window, respectively. The increase in the spatial average of β resulting from inclusions can cause either type of failure. In addition to this overall heating of the material, localized heating in the vicinity of inclusions can cause material failure. This local-heating failure effect is considered in Sec. V.

For sufficiently large concentrations of inclusions, the localized heating can also cause considerable optical degradation of the beam. In the present study it is assumed that the concentration of inclusions is so small that this localized-heating type of optical distortion is negligible. However, it should be mentioned that scattering may be considerably larger at high-power levels than at low levels as a result of the scattering by the heated host material near the inclusion. This effect should be greatest for scattering near the forward angle.

II. Analysis of Absorption Cross Sections

Consider a sample consisting of a nonabsorbing host material of dielectric constant ϵ_H (real) containing N_I inclusions per unit volume, each inclusion having absorption cross section σ_{abs} . Multiple scattering will be neglected -- a reasonable approximation for the present case of small impurity concentrations. The well known result for the absorption coefficient β of the sample is then

$$\beta = \sigma_{abs} N_I . \quad (2.1)$$

Only the case of spherical inclusions of radius a will be considered. The absorption cross section is not generally equal to the geometrical cross section πa^2 . For $ka \ll 1$, where $k = 2\pi/\lambda_H$, with λ_H the wavelength of the radiation in the host material, the value of σ_{abs} typically is small ($\sigma_{abs} \ll \pi a^2$). In the case of $ka \gg 1$ and $|\epsilon| \gg 1$, where $\epsilon = \epsilon_I/\epsilon_H$, with ϵ_I the dielectric constant of the inclusion, the reflection at the surface of the sphere is great, which again makes $\sigma_{abs} \ll \pi a^2$.

Simple expressions for σ_{abs} for various limiting cases will be derived from the classic result of Mie:^{23,24}

$$\sigma_{abs} = \frac{2\pi}{k^2} \sum_{\ell=1}^{\infty} (2\ell+1) \left[\text{Re}(a_{\ell} + b_{\ell}) - |a_{\ell}|^2 - |b_{\ell}|^2 \right] , \quad (2.2)$$

where Re denotes "the real part of." The values of a_{ℓ} and b_{ℓ} in the regions of interest are given below in Eqs. (2.3), (2.7), and (2.8).

For small spheres ($ka \ll 1$),^{24,25} the sums are well approximated by the single term containing a_1 , where

$$a_1 = -i \frac{2}{3} \frac{\epsilon - 1}{\epsilon + 2} (ka)^3. \quad (2.3)$$

The time dependence is taken as $\exp(-i\omega t)$. Some authors²⁴ use $\exp(+i\omega t)$, in which case all factors of i in (2.3) and below would be changed to $-i$. With $\epsilon = \epsilon_R + i\epsilon_g$, substituting (2.3) and $|a_1|^2 \ll \text{Re } a_1$ into (2.2) gives

$$\sigma_{\text{abs}} \cong \frac{12 \epsilon_g ka}{(\epsilon_R + 2)^2 + \epsilon_g^2} \pi a^2, \quad \text{for } ka \ll 1. \quad (2.4)$$

Two limiting cases of (2.4) are of interest. For $\epsilon_g \ll \epsilon_R$, which is satisfied for nonmetals at frequencies not too near the fundamental resonance frequency or the high-frequency absorption edge, β_I and ϵ_g are related the expression

$$\beta_I = 2 \text{Im}(n) k \cong \frac{\epsilon_g k}{\text{Re } n}. \quad (2.5)$$

Using this result to eliminate $\epsilon_g k$ in (2.4) gives

$$\sigma_{\text{abs}} = \frac{12 \text{Re } n}{(\epsilon_R + 2)^2} (\beta_I a) \pi a^2, \quad \epsilon_g \ll \epsilon_R. \quad (2.6)$$

The second limiting case of (2.4) is that of small metallic inclusions. The Drude expression for the dielectric constant is

$$\epsilon = \epsilon_\infty - \frac{\omega_p^2}{\epsilon_H(\omega^2 + i\omega\Gamma)}, \quad (2.7)$$

where Γ is the electron relaxation frequency (often written as $1/\tau$), ϵ_∞ is the contribution to ϵ from the core electrons, and $\omega_p = (4\pi Ne^2/m)^{1/2}$ is the plasma frequency, which has a typical value of $\omega_p = 5 \times 10^{15}$ rad/sec. At $10.6 \mu\text{m}$, $\omega \approx 1.9 \times 10^{14}$ rad/sec. There are two contributions to the relaxation frequency Γ : $\Gamma = \Gamma_{\text{Bu}} + \Gamma_{\text{Su}}$, where the bulk contribution Γ_{Bu} has a typical value¹⁰ of $\Gamma_{\text{Bu}} \approx 5 \times 10^{13} \text{ sec}^{-1}$. The value of the surface-scattering contribution Γ_{Su} is $\sim v_F/a$, where the Fermi velocity v_F has the value $v_F \approx 10^8$ cm/sec for many metals. With $\Gamma_{\text{Bu}} \approx 5 \times 10^{13} \text{ sec}^{-1}$ and $v_F \approx 10^8$ cm/sec, $\Gamma_{\text{Su}} > \Gamma_{\text{Bu}}$ for $a \lesssim 200 \text{ \AA}$.

For typical metals at $10.6 \mu\text{m}$, $\omega_p^2 \gg |\omega^2 + i\omega\Gamma|$, and (2.7) gives

$$\epsilon_{\text{H}} \approx - \frac{\omega_p^2}{\omega^2 + i\omega\Gamma} = - \frac{\omega_p^2}{\omega^2 + \Gamma^2} \left(1 - i \frac{\Gamma}{\omega} \right), \quad \epsilon_{\text{R}} + 2 \approx \epsilon_{\text{R}}. \quad (2.8)$$

Both the real and imaginary parts of the dielectric constant are large in magnitude for small particles of typical metals at $10.6 \mu\text{m}$. Substituting (2.8) into (2.4) gives

$$\sigma_{\text{abs}} = 12 \epsilon_{\text{H}}^{3/2} \frac{\omega^2}{\omega_p^2} \frac{\Gamma a}{c} \pi a^2; \quad \omega_p^2 \gg |\omega^2 + i\omega\Gamma|, \quad (2.9)$$

for metals. This simple expression for the absorption cross section will be used in Sec. III.

Next consider the case of large spheres, so that

$$ka \gg 1, \quad \frac{1}{2} \beta_1 a \gg 1 \quad (2.10)$$

are satisfied, where $\beta_1 = 2k \Im m n$ is the bulk absorption coefficient of the inclusion, $n \equiv \sqrt{\epsilon}$, and $\Im m$ denotes "the imaginary part of." The inequality $\frac{1}{2} \beta_1 a \gg 1$ typically is satisfied for metals and strongly absorbing dielectrics. It will be shown that

$$\sigma_{\text{abs}} = (1 - R_{\perp}) \pi a^2, \quad ka, \frac{1}{2} \beta_1 a \gg 1 \quad (2.11)$$

where $R_{\perp} = |(n-1)/(n+1)|^2$ is the reflection coefficient for normally incident radiation.

The asymptotic expressions for the a_{ℓ} and b_{ℓ} in (2.2) are^{25a}

$$\begin{aligned} a_{\ell} &\approx -i^{\ell} e^{-ika} \frac{\sin x - n \cos x \tanh y}{1 - in \tanh y}, & \text{for } \ell \leq ka \\ &\approx 0, & \text{for } \ell > ka \end{aligned} \quad (2.12)$$

$$\begin{aligned} b_{\ell} &\approx i^{\ell+1} e^{-ika} \frac{\cos x \tanh y - n \sin x}{\tanh y + in}, & \text{for } \ell \leq ka \\ &\approx 0, & \text{for } \ell > ka \end{aligned} \quad (2.13)$$

where $x = ka - \frac{1}{2}(\ell+1)\pi$ and $y = nka - \frac{1}{2}(\ell+1)\pi$. The approximation $\tanh y \approx i$ is valid when $\Im m(n)ka \gg 1$ is satisfied, as seen from the expression

$$\tan(A+iB) = \frac{\sin 2A + i \sinh 2B}{\cos 2A + \cosh 2B} \approx i \tanh 2B \approx i, \quad (2.14)$$

where the approximations are valid for $B \gg 1$.

Using $\tanh y \approx i$ and

$$i^{\ell+1} e^{-ika} = \left(e^{i \frac{\pi}{2}} \right)^{\ell+1} e^{-ika} = e^{-ix} \quad (2.15)$$

reduces (2.12) and (2.13) to

$$a_l \cong e^{-ix} \frac{i \sin x + n \cos x}{1+n}, \quad b_l \cong e^{-ix} \frac{\cos x + i n \sin x}{1+n}, \quad (2.16)$$

for $l \leq ka$. From (2.16), it is easy to show that

$$|a_l|^2 + |b_l|^2 \cong \frac{|n|^2 + 1}{|n+1|^2}, \quad a_l + b_l \cong 1, \quad (2.17)$$

for $l \leq ka$, and from (2.12) and (2.13), $a_l \cong b_l \cong 0$ for $l > ka$.

Substituting (2.17) into (2.2) with the upper limit in the sum replaced by ka and using

$$1 - \frac{|n|^2 + 1}{|n+1|^2} = \frac{2 \operatorname{Re} n}{|n+1|^2} = \frac{1}{2} (1 - R_{\perp}) \quad (2.18)$$

gives

$$\sigma_{\text{abs}} \cong \frac{2\pi}{k^2} \frac{1}{2} (1 - R_{\perp}) \sum_{l=1}^{ka} (2l+1). \quad (2.19)$$

This expression, with

$$\sum_{l=1}^{ka} (2l+1) \cong (ka)^2, \quad \text{for } ka \gg 1, \quad (2.20)$$

gives (2.12).

When $\frac{1}{2} \nu_I a \gg 1$ is not satisfied, that is, when a ray traversing the inclusion is not completely absorbed, it is reasonable that (2.11) should be replaced by the approximate expression

$$\sigma_{\text{abs}} \cong (1 - R_{\perp}) (1 - e^{-\beta I^a}) \pi a^2. \quad (2.21)$$

The well known result that the extinction cross section $\sigma_{\text{ext}} = \sigma_{\text{abs}} + \sigma_{\text{scat}}$ is equal to twice the geometrical cross section when $ka \gg 1$ follows directly from (2.17). Substituting $a_l + b_l = 1$ for $l \leq ka$ and $a_l + b_l = 0$ for $l \geq ka$ into the expression

$$\sigma_{\text{ext}} = \frac{2\pi}{k^2} \sum_{l=1}^{\infty} (2l+1) \operatorname{Re}(a_l + b_l)$$

and using (2.20) gives $\sigma_{\text{ext}} = 2\pi a^2$.

For large spheres with (2.10) satisfied, it is not difficult to show that using geometrical optics approximations gives the result

$$\sigma_{\text{abs}} = (1 - \langle R \rangle) \pi a^2, \quad (2.22)$$

where $\langle R \rangle$ is the value of the reflection coefficient averaged over the illuminated hemispherical surface:

$$\langle R \rangle = \int_0^1 d(\cos^2 \theta) R = \int_0^1 d(\cos^2 \tau) R, \quad (2.23)$$

where θ is the angle between the surface normal and the wave vector of the incident radiation, $\tau \equiv \frac{1}{2}\pi - \theta$, and $R = |r_p|^2 + |r_n|^2$, with r_p and r_n the Fresnel reflection coefficients for the two polarizations. By numerical evaluation of (2.23) for specific values of n , it is not difficult to show that $R_{\perp} \neq \langle R \rangle$ in general, although they do not differ greatly for a number of different values of n .

For example, for $n = 1.27 + i 1.37$, $\langle R \rangle = 0.66$ (p. 292 of Ref. 24) and $R_{\perp} = 0.72$. These two values differ by 8%, which is a typical value of other values of n considered.

It is believed that the result (2.11) is correct since it was derived from the exact theory of Mie.^{23,24} The difference between (2.11) and (2.22) is not important in the present study since the small difference is overshadowed by other effects, such as deviations of particle shapes and sizes from the assumed spheres of common radius. In passing, notice that the phenomenological expression (2.22) results from using geometrical optics approximations and assuming that the reflections for both polarizations from the (curved) differential area on the sphere are the same as those of a plane semi-infinite medium at the same angle of incidence. With these approximations, the Franz, Depperman, Foch²⁶⁻²⁸ surface waves do not arise and surface wave "spray" is neglected. The exact theory of Mie^{23,24} does contain these effects.

Limiting values of the absorption cross section have been discussed above. For example, (2.4) and (2.11) are the expressions for σ_{abs} for the two cases of $ka \ll 1$ and $ka, \frac{1}{2}\beta_1 a \gg 1$, respectively. In some cases the two limiting values are joined smoothly by a monotonically increasing function of particle radius a , as illustrated schematically in Fig. 1. In other cases, σ_{abs} as a function of a may exhibit a maximum, as illustrated in Fig. 2. In this figure, the value of $\sigma_{\text{abs}}/\pi a^2$ at $ka = \infty$ was corrected $(1 - R_{\perp}) = 0.75$, as compared with $1 - \langle R \rangle = 0.66$ in the reference).

The value of σ_{abs} at the peak not only is greater than the $a \rightarrow \infty$ limiting value, but also may be greater than πa^2 . In Fig. 2, for example, $\sigma_{\text{abs}} \cong 2\pi a^2$ at the peak. An absorption coefficient greater than the geometrical cross section πa^2 is possible since the electric field in the inclusion may be larger than the incident field, as is well known in electromagnetic theory (large fields near sharp cracks in dielectrics, for example).

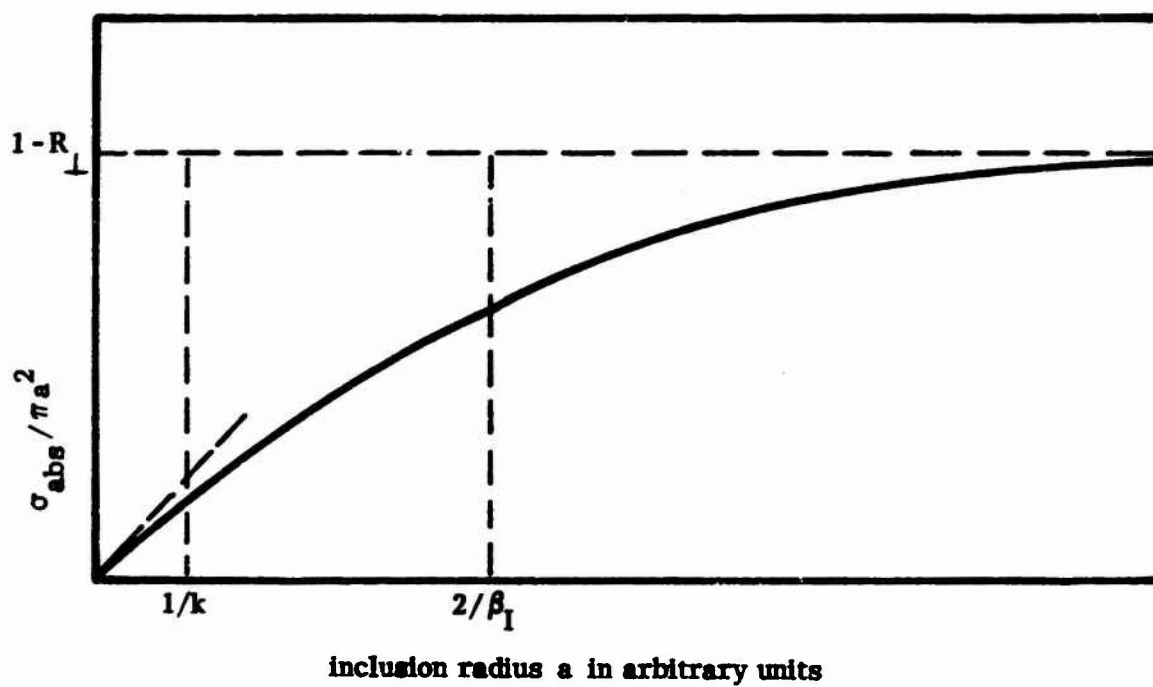


Fig. 1. Schematic illustration of a monotonically increasing cross section.

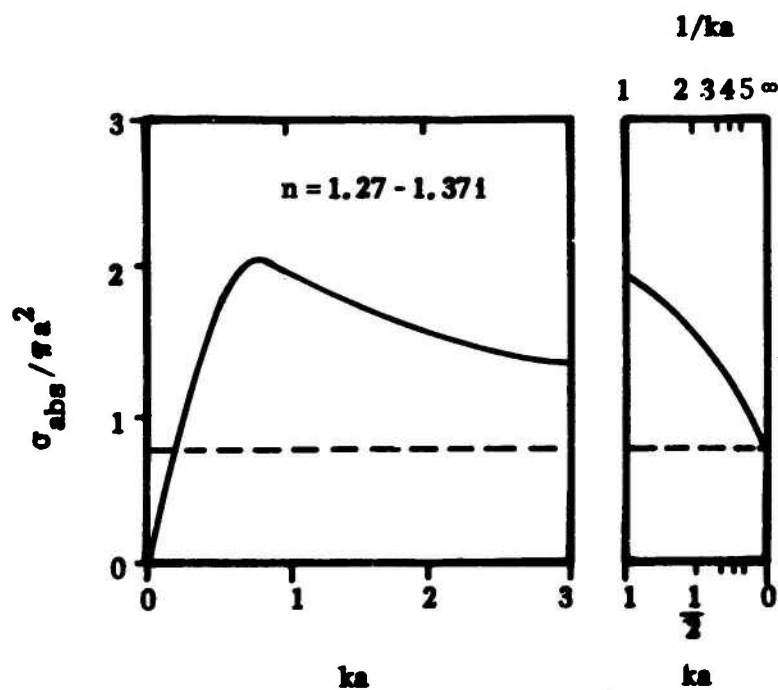


Fig. 2. Example of a cross section with a maximum value greater than πa^2 . After Van der Hulst, Ref. 24, p. 276.

III. Absorption Coefficients for Various Types of Inclusions

The results (2.1), (2.4), (2.11), and (2.21) will now be used to determine the effects of various types of inclusion in crystals. First consider the case of $ka \gg 1$ and $\beta_I a \gg 1$. From (2.1) and (2.11)

$$\beta = \pi a^2 (1 - R_{\perp}) N_I, \quad \text{for } ka, \beta_I a \gg 1. \quad (3.1)$$

This result for β is essentially independent of temperature in many cases of interest. In the infrared region, the frequency dependence of large metallic inclusions is either $\beta \sim \omega^{1/2}$ or β independent of ω , as discussed at the end of the present section. Near the reststrahl region of dielectric materials, R_{\perp} is strongly frequency dependent; otherwise R_{\perp} is relatively constant in the infrared region.

If the absorption coefficient β_I of the inclusion becomes too large, R_{\perp} approaches unity and β becomes small. In the other limit of small β_I ($\beta_I a \ll 1 \ll ka$), the rays traversing the inclusions are not completely absorbed, and β becomes small again.

Consider this latter case of large inclusions ($ka \gg 1$) that absorb only a fraction of the radiation in the inclusion $\beta_I a \ll 1$. From (2.1) and (2.21),

$$\beta \cong \frac{3}{4} (1 - R_{\perp}) f \beta_I, \quad \beta_I a \ll 1 \ll ka, \quad (3.2)$$

where $f = 4 \pi a^3 N_I / 3$ is the fractional volume of inclusions.

Next consider the small-inclusion case of $ka \ll 1$. From (2.1) and (2.4)

$$\beta \cong \frac{9 \epsilon_g}{(\epsilon_R + 2)^2 + \epsilon_g^2} f k, \quad ka \ll 1. \quad (3.3)$$

For nonmetals, where $\epsilon_g \ll \epsilon_R$ typically is satisfied, (2.1) and (2.6) give

$$\beta \cong \left[\frac{9 \operatorname{Re} n}{(\epsilon_R + 2)^2 + \epsilon_g^2} \right] \beta_I f, \quad \text{for } ka \ll 1, \epsilon_g \neq 1, \quad (3.4)$$

where the factor in the bracket typically has a value near unity. For very strongly absorbing dielectric materials (ω near the fundamental resonance or the electronic absorption edge, for example), the result (3.3) should be used, otherwise (3.4) is more convenient.

The absorption coefficients in (3.2) and (3.4) are strongly temperature and frequency dependent in general. If β_I is controlled by, say, the n-phonon summation process, then $\beta \sim T^{n-1}$ in the high temperature limit and β decays exponentially with frequency.

For the case of $\frac{3}{4}(1 - R_{\perp}) \cong 9 \operatorname{Re}(n) [(\epsilon_R + 2)^2 + \epsilon_g^2]^{-1} \cong 1$, (3.2) and (3.4) give

$$\beta \cong f \beta_I, \quad \text{for both } ka \gg 1 \text{ and } ka \ll 1. \quad (3.5)$$

For the cases above [(3.2), (3.4), and (3.5)] for which $\beta \sim \beta_I$, a small fraction of the radiation entering the inclusion is absorbed, while for $\beta \sim (1 - R_{\perp}) \pi a^2$ in (3.1), essentially all the radiation entering the inclusion is absorbed, roughly speaking.

Next consider the case of small ($ka \ll 1$) metallic inclusions. From (2.1) and (2.9),

$$\beta \cong \frac{9 n_H^3 \omega^2 \Gamma f}{c \omega_p^2} . \quad (3.6)$$

This expression (3.6) shows that β increases quadratically with frequency and is independent of temperature, roughly.

The absorption by small metallic inclusions has a peak that lies in the ultraviolet or visible region typically.¹⁰ The value of β at this peak is much greater than the value in the infrared. Thus ultraviolet and visible measurements can be used to verify the source of absorption by small metallic particles in the infrared.

Consider, as an example, small potassium spheres in KCl or KBr. F centers can be transformed to colloidal potassium (small spheres) by heating the crystal.²⁹⁻³¹ The transformation is enhanced by ultraviolet radiation. The wavelengths λ_0 of the peaks for the small potassium spheres in KCl or KBr are 0.730 and 0.770 μm , respectively.¹⁰ In the visible and ultraviolet, $\Gamma^2 \ll \omega^2$, and (2.7) and (3.3) give, with $k = n_H \omega/c$

$$\epsilon \cong \epsilon_\infty - \frac{\omega_p^2}{\epsilon_H \omega^2} + i \frac{\omega_p^2 \Gamma}{\epsilon_H \omega^3} ,$$

$$\beta \cong \frac{\Gamma^2 \omega^2 \beta_{pk}}{(\omega^2 - \omega_0^2)^2 + (\Gamma \omega_0^2 / \omega)^2} , \quad (3.7)$$

where

$$\omega_0^2 = \frac{\omega_p^2}{2\epsilon_H + \epsilon_{I\omega}}, \quad \beta_{pk} = \frac{9n_H^3 \omega_0^4}{c \omega_p^2 \Gamma} f.$$

Notice that for fairly narrow lines ($\Gamma \lesssim \omega_0/10$), $\beta \cong \beta_{pk}$ at the peak at $\omega = \omega_0$, and Γ is the full line width between the points $\beta = \frac{1}{2} \beta_{pk}$.

Dividing β_{pk} by the infrared absorption coefficient (3.6) gives

$$\frac{\beta_{pk}}{\beta_{IR}} = \frac{\omega_0^4}{\omega_{IR}^2 \Gamma^2}. \quad (3.8)$$

For $\lambda_0 = 2\pi c/\omega_0 = 0.75\mu\text{m}$, $\lambda_{IR} = 10.6\mu\text{m}$, and $\Gamma = 5 \times 10^{14} \text{ sec}^{-1}$, (3.8) gives

$$\frac{\beta_{pk}}{\beta_{10.6}} = 6.4 \times 10^3. \quad (3.9)$$

If it is assumed that the limit of detectability of color for the colloids in KBr or KCl corresponds to $\beta_{pk} = 0.03 \text{ cm}^{-1}$, the value of $\beta_{10.6}$ from (3.9) is $\beta_{10.6} = 5 \times 10^{-6} \text{ cm}^{-1}$. Thus the contribution to β from potassium colloids in water while KCl or KBr crystals should be less than $\sim 5 \times 10^{-6} \text{ cm}^{-1}$, according to the order-of-magnitude estimate. Colored crystals could have a greater contribution to β from this source. It should be mentioned that impurities in the form of F centers which give rise to strong absorption in the visible region, may not give rise to detectable absorption in the infrared.

The usual concept of reflectivity loses its meaning when $ka \ll 1$. However, in this case of a small sphere, the incident electric field is nearly constant across the sphere, and the field E_I inside the sphere can be obtained from simple electrostatic theory. The well known result is

$$E_I = \frac{3}{\epsilon + 2} E_H ,$$

where E_H is the field in the host crystal in the absence of the inclusion. Thus, for a sphere with $|\epsilon| \gg 1$, the field inside the sphere is much smaller than that in the host material.

Consider the frequency dependence of $1 - R_{\perp}$ in (3.1). For the case of $\Gamma^2 \gg \omega^2$, (2.8) gives the familiar result

$$\epsilon_g = \frac{\omega_p^2}{\epsilon_H \omega \Gamma} = \frac{4\pi\sigma}{\epsilon_H \omega} ,$$

where $\sigma = \omega_p^2 / 4\pi\Gamma$ is the conductivity. For $\epsilon \cong i\epsilon_g$, the value of n is $n = \sqrt{\epsilon}$ is $\left(\frac{2\pi\sigma}{\epsilon_H \omega} \right)^{1/2} (1+i)$, and (2.18) gives

$$1 - R_{\perp} = \left(\frac{8}{\epsilon_g} \right)^{1/2} = \left(\frac{2\omega\epsilon_H}{\pi\sigma} \right)^{1/2} . \quad (3.10)$$

With (3.1), this gives $\beta \sim \omega^{1/2}$, as discussed under (3.1).

For the case of $\Gamma^2 \cong \Gamma_{Bu}^2 \ll \omega^2$, (2.8) gives

$$n = \sqrt{\epsilon} \cong \frac{\omega_p \Gamma_{Bu}}{2n_H \omega^2} \left(1 + i \frac{2\omega}{\Gamma_{Bu}} \right) . \quad (3.11)$$

Substituting (3.11) into (2.18) gives

$$1 - R_{\perp} \cong \frac{2n_H \Gamma_{Bu}}{\omega_p} , \quad \Gamma^2 \cong \Gamma_{Bu}^2 \ll \omega^2 . \quad (3.12)$$

From (3.12) and (3.1), β is independent of frequency, as mentioned in the second case under (3.1). The temperature dependence of β in this case is determined by Γ_{Bu} in the usual case in which n_H and ω_p are nearly independent of T .

IV. Examples

Volume fractions of various inclusions in a nonabsorbing host for $\beta = 10^{-3} \text{ cm}^{-1}$ will be calculated in this section. For large nonmetallic particles with $1 - R_{\perp} \sim 1$, (3.1) gives $\beta = \pi a^2 N_I$. Thus, a single nonmetallic particle of radius $a = 50 \mu\text{m}$ (with $ka, \beta_I a \gg 1$) in a 1 cm^3 crystal gives

$$\beta \cong 10^{-4} \text{ cm}^{-1}.$$

The volume fraction for this inclusion, $f \equiv (4\pi a^3 N_I / 3)$, is $f = 5 \times 10^{-7}$. The same value ($\beta = 10^{-4} \text{ cm}^{-1}$) is obtained with 100 particles per cubic centimeter of $a = 5 \mu\text{m}$ (with, say, $k \equiv k_{\text{host}} = 2k_{\text{vac}} = 4\pi / 10 \mu\text{m}$, so that $ka = 2\pi \gg 1$ $\Im m(n) \cong 1$). The volume fraction of inclusions in this case is $f = 5 \times 10^{-8}$.

Clearly, such macroscopic inclusions must be essentially eliminated in order to obtain small values of β . Metallic inclusions (with $ka \gg 1$) are not as troublesome as nonmetallic. For a metallic inclusion with $R_{\perp} = 0.95$, or $1 - R_{\perp} = 1/20$, 20 times more inclusions are required to give $\beta = 10^{-4} \text{ cm}^{-1}$. Even with such a reduction in absorption, the absorption by large metallic inclusions is not negligible; the volume fractions in the two examples above become 10^{-5} and 10^{-6} , which are still quite small.

For the small inclusion case of $9\text{Re}(n)[(\epsilon_R + 2)^2 + \epsilon_I^2]^{-1} \cong 1$ in (3.4), or for $\frac{3}{4}(1 - R_{\perp}) \cong 1$ in (3.2), with $f = 10^{-5}$ and $\beta_I = 10 \text{ cm}^{-1}$, (3.4) or (3.2) gives $\beta = 10^{-4} \text{ cm}^{-1}$. For $\beta_I = 10^3 \text{ cm}^{-1}$, $f = 10^{-7}$ gives $\beta = 10^{-4}$. Consider the specific example of ZnS in ZnSe, which is of interest because Kodak's Irtran 4 is polycrystalline ZnSe. Until recently, ZnS was added to inhibit grain growth. It is believed

that ZnS collects along grain boundaries. With $Re n_I = 2.47$ and $\beta_I = 0.4 \text{ cm}^{-1}$ for ZnS and $n_H = 2.89$ for ZnSe, $Re n \cong n \cong 0.855$, and for $ka \ll 1$ and $\epsilon_j \ll 1$, (3.4) gives

$$\beta \cong 0.38 f \text{ cm}^{-1}.$$

The volume fraction corresponding to $\beta = 10^{-4} \text{ cm}^{-1}$ is $f = 2.6 \times 10^{-4}$. The results for $\beta_I a \ll 1 \ll ka$ from (3.2) are $\beta = 0.29 f \text{ cm}^{-1}$ and $\beta = 10^{-4} \text{ cm}^{-1}$ for $f = 3.4 \times 10^{-4}$. Thus, ~ 0.01 to ~ 0.03 volume percent of ZnS in ZnSe gives $\beta \cong 10^{-4} \text{ cm}^{-1}$.

The present theory indicates that the $10.6 \mu\text{m}$ value of $\beta \cong 0.1 \text{ cm}^{-1}$ for Irtran 4 is not a result of ZnS in the crystal. Since $\beta_I = 0.4 \text{ cm}^{-1}$, approximately 25 percent ZnS would be required to give $\beta = 0.1 \text{ cm}^{-1}$. Even the doped samples did not contain such a large fraction of ZnS.

Next consider the case of very small metallic inclusions. For $\omega \cong 2 \times 10^{14} \text{ rad/sec}$, $\Gamma \cong \Gamma_{Su} \cong 5 \times 10^{14} \text{ sec}^{-1}$ (for $a = 20 \text{ \AA}$), $\omega_p = 5 \times 10^{15} \text{ rad/sec}$, $k_{vac} \cong 2\pi/10.6 \mu\text{m}$, and $\epsilon_H = 4$, (3.6) gives

$$\beta \cong 2000 f \text{ cm}^{-1}.$$

For a very small fractional volume of $f = 5 \times 10^{-8}$, this gives $\beta = 10^{-4} \text{ cm}^{-1}$ for the small metallic inclusions.

As a final example, consider the problem of a surface contaminated by, say, a polishing compound. Since polishing compounds contain light elements such as oxygen, aluminum, and carbon (in order to obtain hardness), their fundamental resonance frequencies are high, that is, near the $10.6 \mu\text{m}$ frequency.

Thus, their absorption coefficients are large at $10.6\mu\text{m}$. For example, extrapolating the Al_2O_3 data on the range $4\mu\text{m} < \lambda < 5.5\mu\text{m}$ to $10.6\mu\text{m}$ gives $\beta_I = 10^2 - 10^4 \text{ cm}^{-1}$. Even though the extrapolation procedure gives a highly uncertain value of β_I , a value of $\beta_I = 100 \text{ cm}^{-1}$ seems quite reasonable; the values of β for LiF, MgO, and GaP at $10.6\mu\text{m}$ are 50, 60, and 123 cm^{-1} , respectively.

As a simple specific model, consider particles of radius $a = \frac{1}{4}\mu\text{m}$ in a surface layer of thickness $L_{\text{Su}} = 2a$. The fraction volume in the surface layer is taken as $f_{\text{Su}} = 10^{-2}$, and the value of β_I is assumed to be 100 cm^{-1} . The value of β for the surface layer, from (3.5), is $\beta_{\text{Su}} \cong f_{\text{Su}} \beta_I = 1$. The fraction of the energy absorbed in the surface layer is $\beta_{\text{Su}} L_{\text{Su}} = 5 \times 10^{-5}$. Thus, the fractional absorption at two surfaces is $\sim 10^{-4}$.

In spite of the fact that the cross sections are often much less than πa^2 , they are quite large in a number of important cases. As a point of reference, recall that the real and imaginary parts of the wavevector are equal for $\beta_I = 4\pi/10.6\mu\text{m} = 10^4 \text{ cm}^{-1}$, roughly, at $10.6\mu\text{m}$. See Eq. (2.5). For $N = 10^{23} \text{ cm}^{-3}$, the corresponding cross section is $\sigma = \beta/N = 10^{-19} \text{ cm}^2$. These large values of $\sigma = 10^{-19} \text{ cm}^2$ or $\beta = 10^4 \text{ cm}^{-1}$ are typical of values at the fundamental resonance in ionic crystals.

For a value of $\beta = 10^{-4} \text{ cm}^{-1}$ and a volume of $f \sim 10^{-7}$ to 10^{-8} , which corresponds to $\sim 10^{15}$ to 10^{16} impurity atoms per cm^3 , the value of the cross section per impurity atom is $\sim 10^{-4}/10^{15}$ to $10^{-4}/10^{16} = 10^{-19}$ to 10^{-20} cm^2 . Thus, the average cross section per atom in a highly absorbing inclusion is large, approaching that of an atom in a solid absorbing at the fundamental resonance.

V. Material Failure From Local Heating

The heating of macroscopic inclusions can give rise to localized regions of high temperature that can cause material failure when the intensity is large. This is not a nonlinear effect, but is usually important only at relatively high intensities. Consider the same model, used in the previous sections, of a uniformly heated spherical inclusion of radius a in an infinite host crystal that does not absorb the laser radiation. For times short with respect to a characteristic time for heat to diffuse by a distance a , very roughly speaking, most of the energy absorbed by the inclusion remains in the inclusion. Thus the temperature in the inclusion increases linearly with time. For times large with respect to the characteristic time, part of the absorbed energy has diffused into the host crystal, and the temperature rise in the inclusion is considerably less than the value obtained by neglecting diffusion. Thus, a given amount of energy will cause a greater temperature rise if it is deposited in a time that is short with respect to the characteristic time than if deposited in a time long with respect to the characteristic time; the local heating of macroscopic inclusions is a more severe problem in high-intensity short-pulse systems than in low-intensity long-pulse or cw systems of equal average intensity.

The criterion for failure of the window material depends on the details of the laser system and the type of material and inclusions. Since there is no universal criterion, it will be assumed that a temperature rise of 1,000 K constitutes failure. This is a reasonable choice for the following reasons: This temperature is approximately the correct value for melting temperatures and fracture-inducing temperatures. The latter have typical values of the order

of $^{32-34} \sigma_f / \alpha E$, where σ_f is the material strength, α the linear thermal expansion coefficient, and E the Young's modulus. For $\sigma_f = 10^5$ psi, $\alpha = 10^{-5}$ and $E = 10^7$ psi, the temperature corresponding to fracture is 1,000 K. Heats of fusion have typical values corresponding to several hundred degrees Kelvin. At 1,000 K above ambient temperature in materials which do not melt, the ionic diffusion may be important. Although order-of-magnitude accuracy in temperature usually is not sufficient, order-of-magnitude accuracy of intensities corresponding to failure is all that can be expected at present, and this is often sufficient. Since the present interest is in this failure intensity I_f and the failure temperature T_f is linearly related to I_f , the value $T_f = 1,000$ K should be sufficient for present purposes.

Some differences between the failure criteria for high-power windows and for previous studies of glasses for glass-host lasers (at $1.06 \mu\text{m}$, for example) should be mentioned. In the latter, highly focused, single nano-second pulses are used, and breakdown occurs in a small volume. In the former, all of the window is illuminated, apart from edges, support-structure shadows, Cassegranian-optics "shadows", etc., and operating durations range from microsecond pulses with repetition rates of a few hundred pulses per second, to ~ 1 sec pulses with several seconds between pulses in order to allow the window to be cooled, to continuous operation.

Thus, two important features of high-power laser-window failure are that failure of the weakest part of the window can constitute system failure, and that fatigue and other multiple-pulse effects must be considered since repeated pulses must be withstood. As an example, in a single-pulse measurement, a laser glass conceivably could melt locally and recrystallize without

leaving detectable damage. For a window in a pulse-operated system, the local absorption coefficient could be changed by the high temperature associated with the first pulse or the first n pulses, thus causing increased absorption in subsequent pulses with eventual failure.

Bloembergen has suggested that local field enhancement, such as that occurring at the edge of a crack in a material, may give rise to local intensities up to 100 times greater than the nominal external intensity. This effect could lower the values of the breakdown intensities calculated below by a factor of ~ 100 .

The temperature rise for $T < T_m$, where T_m is the melting temperature, can be calculated simply for the following model. The spherical inclusion of radius a has temperature-independent values C_I and K_I of heat capacity per unit volume and thermal conductivity. The host crystal has temperature-independent values C_H and K_H . The boundary between the two is assumed to be thermally perfect; that is, there is no thermal impedance. Heat absorption by the host crystal is assumed negligible.

The thermal time constant

$$\tau = Ca^2/4K$$

is the time required for heat to diffuse a distance a , roughly speaking. For short times $t \ll \tau_I, \tau_H$, where the subscripts I and H denote the values of τ in the inclusion and in the host crystal, respectively, the diffusion of heat out of the inclusion is negligible. Thus, the heat-flow equation

$$-K \nabla^2 T + C \frac{\partial T}{\partial t} = S, \quad (5.1)$$

where S is the heat source (W/cm^3), can be approximated by

$$C_I \frac{\partial T_I}{\partial t} = S_I, \quad \text{for } t \ll \tau_I, \tau_H. \quad (5.2)$$

Uniform volume heating of inclusion. First consider the case of spatially constant heat generation in the inclusion (for example, $\beta_I a \ll 1$ or, in metals, skin depth $\delta \gg a$). The source term can be written as $S = 0$ in the host material and

$$S_I = 3 \sigma_{\text{abs}} I / 4 \pi a^3 \quad (5.3)$$

in the inclusion, where I is the incident intensity and σ is the cross section of the inclusion, as discussed in Sec. II. It should be mentioned that (5.1) will be solved separately in the inclusion and in the host material, and the appropriate matching of the temperature and heat flow at the boundary will be made. Thus K is a constant in each region, and the usual spatial derivatives of K do not appear in (5.1).

For T defined as zero at the time the laser is turned on ($t = 0$), the solution to (5.2) is

$$T_I = 3 \sigma_{\text{abs}} I t / 4 \pi a^3 C_I, \quad \text{for } t \ll \tau_I, \tau_H. \quad (5.4)$$

There is a steady-state solution to (5.1), which can be obtained as follows.

The function

$$T_I = T_c - \frac{S_I}{6K_I} r^2 = T_c - \Delta T \left(\frac{r}{a}\right)^2, \quad t \gg \tau_I, \tau_H, \quad (5.5)$$

with

$$\Delta T = \sigma_{\text{abs}} I / 8 \pi a K_I ,$$

is a solution to $-K_I \nabla^2 T_I = S_I$, as is easily seen by substitution, since

$$\nabla^2 r^2 = \frac{1}{r^2} \frac{\partial}{\partial r} r^2 \frac{\partial r^2}{\partial r} = 6 .$$

Here T_c is the temperature at the center of the inclusion and ΔT is the temperature difference between the center and edge of the inclusion.

The heat flow across the surface $r = a$ is

$$Q_a = -4 \pi a^2 K_I \left(\frac{\partial T_I}{\partial r} \right)_{r=a} = \frac{1}{3} 4 \pi a^3 S_I . \quad (5.6)$$

Physically, this result indicates that the heat generated in the inclusion flows out of its surface in the steady state.

Next consider the steady-state solution of (5.1) in the host crystal. It is well known, from the electrostatic potential of a point charge, for example, that $\nabla^2 (1/r) \sim \delta(r)$, where δ is the delta function. Thus, $\nabla^2 (1/r) = 0$ for $r > 0$, as is easily verified by taking the derivatives. Thus, the solution to $-K_H \nabla^2 T_H = 0$ for $r > a$ is

$$T_H = a T_a / r . \quad (5.7)$$

From (5.7), the value of Q_a is

$$Q_a = -4 \pi a^2 K_H \left(\frac{\partial T_H}{\partial r} \right)_{r=a} = 4 \pi a K_H T_a , \quad (5.8)$$

where T_a is the temperature at $r = a$. Equating the values of Q_a in (5.6) and (5.8) and using (5.3) gives

$$T_a = \sigma_{\text{abs}} I / 4\pi a K_H . \quad (5.9)$$

From (5.5) with $r^2 = a^2$

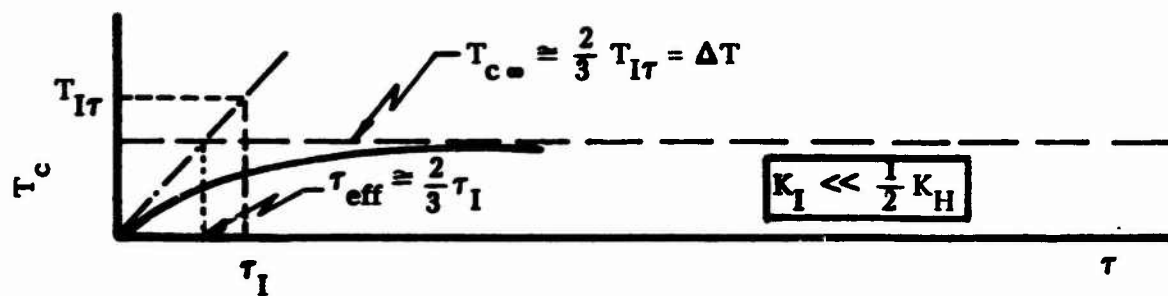
$$T_a = T_c - \Delta T = T_c - \frac{\sigma_{\text{abs}} I}{8\pi a K_I} . \quad (5.10)$$

From (5.9) and (5.10), the steady state value of T_c is

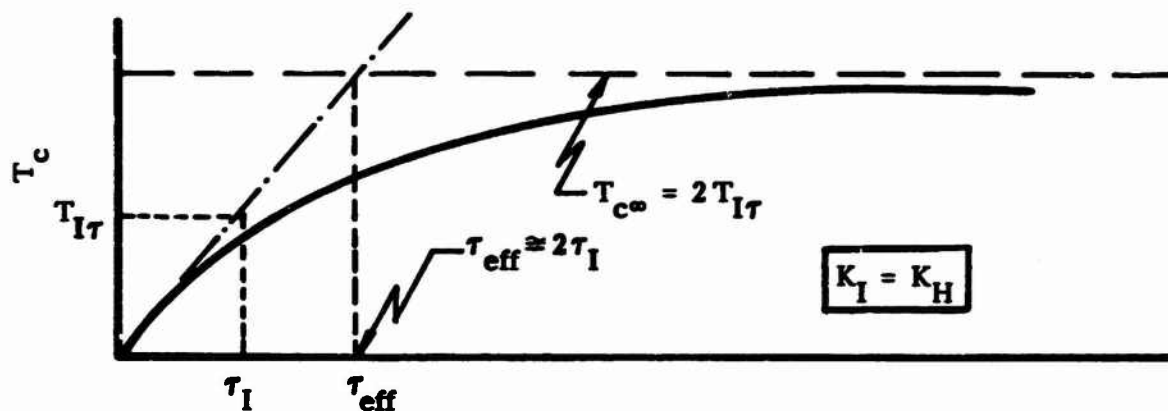
$$T_{c\infty} = \Delta T \left(1 + \frac{2K_I}{K_H} \right) = \frac{3\sigma_{\text{abs}} I}{8\pi a K_{\text{eff}}} , \quad \frac{1}{K_{\text{eff}}} \equiv \frac{1}{3} \left(\frac{2}{K_H} + \frac{1}{K_I} \right) . \quad (5.11)$$

The first term in (5.11) is the temperature rise in the inclusion and the second term is the temperature rise in the host crystal. The value of K_{eff} is determined by the smaller of K_H and K_I when one K is much larger than the other. Thus for a metallic inclusion in an infrared window material, $K_{\text{eff}} \cong \frac{3}{2} K_H$.

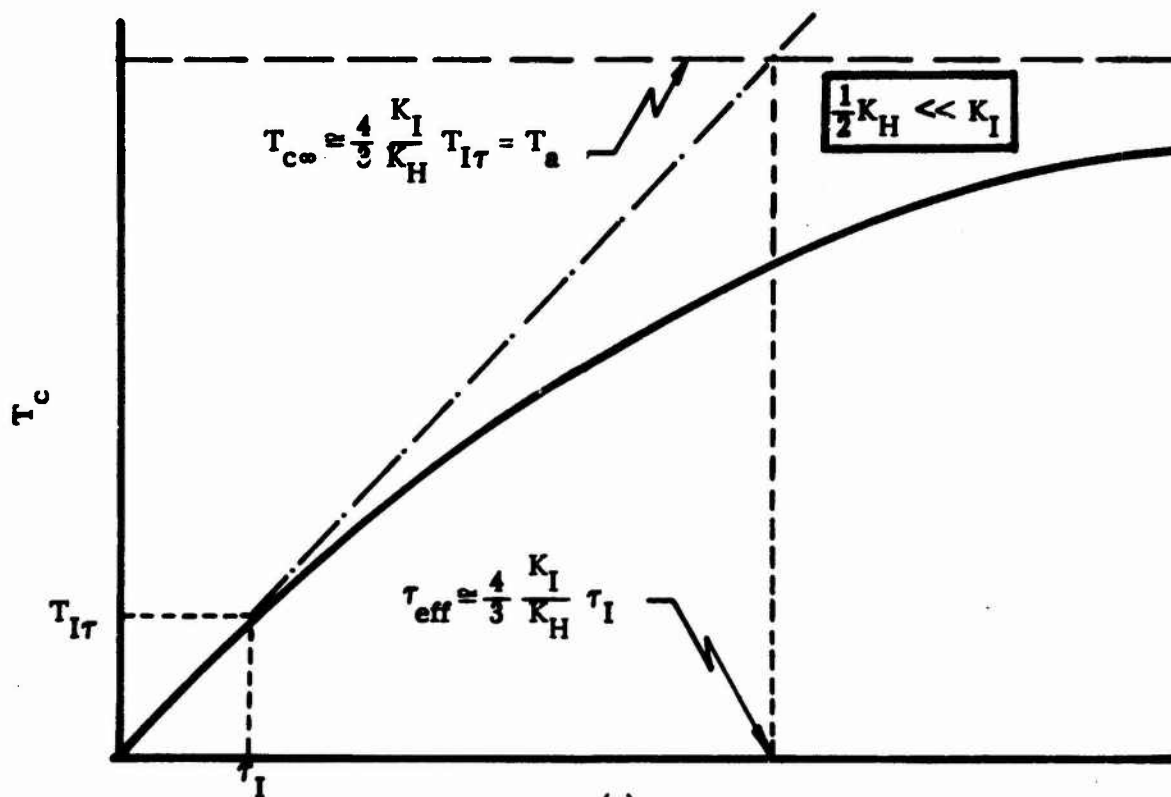
The results (5.4) and (5.11) are illustrated schematically in Fig. 3 for the three cases of $K_I \ll \frac{1}{2} K_H$, $K_I = K_H$, and $\frac{1}{2} K_H \ll K_I$ in the (a), (b), and (c) parts of the figure, respectively. For all three cases, T_c increases linearly with time according to (5.4) for $t \ll \tau_{\text{eff}}$. Consider the values of T_c for $t \ll \tau_{\text{eff}}$. For $K_H \rightarrow \infty$, (5.9) gives $T_a = 0$; the infinitely conducting host maintains the temperature of the surface of the inclusion at $T = 0$. In this case, (5.11) and (5.5) give $T_{c\infty} = \Delta T = \frac{2}{3} T_{\tau I}$, and the $T_{c\infty}$ asymptote lies below $T_{\tau I}$ in Fig. 3a. In Fig. 3b, for $K_I = K_H$, $T_{c\infty} = 2 T_{\tau I}$.



(a)



(b)



(c)

Fig. 3. Schematic illustration of the temperature at the center of a uniformly heated spherical inclusion for three limiting values of K_H/K_I . See Eqs. (5.4) and (5.11).

For $K_H \rightarrow 0$, (5.11) gives $T_{c\infty} \rightarrow \infty$. There is no finite steady-state solution since the host crystal conducts no heat out of the inclusion. The temperature of the inclusion rises linearly with time for all times according to (5.4). For K_H large but finite, $T_{c\infty}$ is large as illustrated in Fig. 3c.

Surface heating of inclusion. Next consider the case in which the heat is generated near the surface of the inclusion, rather than uniformly throughout its volume. Such is the case for typical metallic inclusions in dielectric hosts or in the extreme case of $\beta a \gg 1$ for other types of inclusions in dielectric hosts. As an example of the latter, for $\beta = 10^4 \text{ cm}^{-1}$ and $a = 10 \mu\text{m}$, $\beta a = 10$. The skin depth δ for a metal is³⁵

$$\delta = c (2\pi\omega\sigma)^{-1/2} \quad (5.12)$$

in Gaussian units, where c is the velocity of light, ω is the angular frequency, and σ is the conductivity. A typical value for δ is 40 \AA for Cu with $\lambda = 10 \mu\text{m}$.¹⁰ Energy is absorbed in the metal at a rate which decreases exponentially with distance into the metal [$S \propto E^2 \propto \exp(-2x/\delta)$].

For spherical inclusions with radius $a \gg \delta$, we assume that heat is generated uniformly within a layer of thickness δ over the entire surface of the inclusion. This is a good approximation for $a \ll \lambda$ because the electric field is nearly constant over distances of order a . For larger radii, there will be local hot spots over the surface not only on the front surface but also on the rear surface.

There are three characteristic times of interest. First,

$$\tau_{\delta} = 4C_I \delta^2 / \pi K_I \quad (5.13)$$

is roughly the time in which heat diffuses out of the skin depth, assuming negligible diffusion into the host for small time since K_H (dielectric) $\ll K_I$ (metal).

Second,

$$\tau_a = 4C_I a^2 / 9\pi K_I \quad (5.14)$$

is the time in which heat diffuses from the inclusion surface to the center, roughly speaking. Third,

$$\tau_H = C_H a^2 / 3K_H \quad (5.15)$$

is roughly the time in which heat diffuses a distance equal to the radius of the inclusion into the host. The values of the numerical coefficients in (5.13)-(5.15) are chosen for later convenience.

The temperature at the inclusion surface will now be determined for four time scales: For $t \ll \tau_{\delta}$, heat does not diffuse out of the skin depth, and the surface temperature is linear in time. At later times, but with $t \ll \tau_a$, heat is diffusing out of the skin depth and the thickness of the heated region increases as $t^{1/2}$. Thus, the surface temperature increases as $t^{1/2}$. For still larger times $\tau_a \ll t \ll \tau_H$, the temperature within the sphere reaches a spatially constant value and increases linearly with time. Finally, for $t \gg \tau_H$, heat diffusion into the host becomes important and the temperature within the inclusion reaches an equilibrium value.

For $t \ll \tau_\delta$ and $\delta \ll a$, the spherical shape of the inclusion surface is not important, and we can solve the easier problem of heat generation in a thin plane slab. The Laplace transform of the diffusion equation (5.1) is³⁶

$$\frac{d^2 T(x, p)}{dx^2} - q^2 T = \frac{S}{Kp}, \quad q^2 = \frac{pc}{K}. \quad (5.16)$$

In the present problem, heat is generated at a rate $S = I\sigma_{abs}/4\pi a^2 \delta$ in the slab $0 < x < \delta$, where $x = \delta$ corresponds to inclusion surface $r = a$. Equation (5.16) inside, outside, and within the skin depth of the inclusion becomes

$$\frac{d^2 T_I(p)}{dx^2} - q_I^2 T_I(p) = 0, \quad x < 0 \quad (5.17a)$$

$$\frac{d^2 T_H(p)}{dx^2} - q_H^2 T_H(p) = 0, \quad x > \delta \quad (5.17b)$$

$$\frac{d^2 T_\delta(p)}{dx^2} - q_I^2 T_\delta(p) = \frac{S}{K_I p}, \quad 0 < x < \delta. \quad (5.17c)$$

Equation (5.17) has the solution

$$T_I(p) = A e^{q_I x}, \quad x < 0 \quad (5.18a)$$

$$T_H(p) = B e^{-q_H x}, \quad x > \delta \quad (5.18b)$$

$$T_\delta(p) = \frac{S}{p^2 C_I} + C e^{q_I x} + D e^{-q_I x}, \quad 0 < x < \delta. \quad (5.18c)$$

The constants A through D are determined from the boundary conditions that T and $K \frac{dT}{dx}$ are continuous at $x = 0$ and $x = a$:

$$A = \frac{S}{p^2 C_I} + C + D \quad (5.19a)$$

$$q_I A = q_I C - q_I D \quad (5.19b)$$

$$B e^{-q_H a} = \frac{S}{p^2 C_I} + C e^{q_I a} + D e^{-q_I a} \quad (5.19c)$$

$$-K_H q_H B e^{-q_H a} = K_I q_I C e^{q_I a} - K_I q_I D e^{-q_I a} \quad (5.19d)$$

The temperature at the inclusion surface is given by $T(p) = B \exp(-q_H \delta)$.

Solving (5.19) for B gives

$$T(x=\delta, p) = \frac{S}{C_I} \frac{\sqrt{C_I K_I}}{(\sqrt{C_I K_I} + \sqrt{C_H K_H})} \frac{1}{p^2} (1 - e^{-q_I a}).$$

Inverting and keeping the dominant term for t small gives

$$T(x=\delta, t) = \frac{S}{C_I} \frac{\sqrt{C_I K_I}}{(\sqrt{C_I K_I} + \sqrt{C_H K_H})} t, \quad t \ll \tau_\delta.$$

Notice that for $C_I K_I \gg C_H K_H$ (appropriate for metal in dielectric)

$T(x=\delta, t) = St/C_I$ as one would expect. From this last equation with $S = I \sigma_{abs} / 4 \pi a^2 \delta$, the surface temperature of the inclusion for small times is

$$T_a = \frac{1}{C_I} \frac{\sqrt{C_I K_I}}{(\sqrt{C_I K_I} + \sqrt{C_H K_H})} \frac{I \sigma_{abs}}{4 \pi a^2 \delta} t \approx \frac{I \sigma_{abs}}{4 \pi a^2 \delta C_I} t, \quad t \ll \tau_\delta. \quad (5.20)$$

In (5.20) and in equations below, the approximate equalities are valid for $C_I K_I \gg C_H K_H$. For $\tau_\delta \ll \tau \ll \tau_a$, we can still use the approximation of heat generation in a plane slab with the heat generating region approximated by a delta-function source at $x = 0$. Solutions to the heat-diffusion equation (5.16) are now

$$T_I(p, x) = A e^{q_I x}, \quad x < 0, \quad (5.21a)$$

$$T_H(p, x) = B e^{-q_H x}, \quad x > 0. \quad (5.21b)$$

The boundary conditions are that $T_I = T_H$ at $x = 0$ and that the heat flux away from $x = 0$ is $I \sigma_{\text{abs}} / 4 \pi a^2$:

$$A = B, \quad \frac{1}{p} \frac{I \sigma_{\text{abs}}}{4 \pi a^2} = A K_I q_I + B K_H q_H. \quad (5.22)$$

Solving (5.22) for A or B gives

$$T(x=0, p) = \frac{1}{(\sqrt{C_H K_H} + \sqrt{C_I K_I})} \frac{I \sigma_{\text{abs}}}{4 \pi a^2} \frac{1}{p^{3/2}}. \quad (5.23)$$

The inverse transform of (5.23) is the temperature at the inclusion surface

$$T_a = \frac{2}{\sqrt{\pi} (\sqrt{C_H K_H} + \sqrt{C_I K_I})} \frac{I \sigma_{\text{abs}}}{4 \pi a^2} t^{1/2}, \quad \tau_\delta \ll t \ll \tau_a. \quad (5.24)$$

When $t \gg \tau_a$, the temperature inside the spherical inclusion reaches a spatially uniform value. The present problem then is equivalent to uniform

heat generation within an inclusion of infinite conductivity, and we can use the previously calculated result (5.4) to obtain

$$T_a = \frac{3 I \sigma_{abs} t}{4 \pi a^3 C_I} , \quad \tau_a \ll t \ll \tau_H . \quad (5.25)$$

For $t \gg \tau_H$, the temperature inside the spherical inclusion reaches an equilibrium value, and the temperature in the host is given by $T_H = T_{a\infty}(a/r)$. The constant, $T_{a\infty}$, is determined by equating the heat flux away from the inclusion to $I \sigma_{abs}$,

$$I \sigma_{abs} = 4 \pi a^2 K_H T_{a\infty} / a ,$$

or

$$T_{a\infty} = \frac{I \sigma_{abs}}{4 \pi a K_H} , \quad t \gg \tau_H . \quad (5.26)$$

This result is equivalent to (5.11) with $K_I = \infty$ (so that the temperatures at the edge and center of the inclusion are equal).

The temperature at the surface of the spherical inclusion is sketched in Fig. 4 for the various time regimes. The extrapolated low-temperature linear time dependence of the temperature intersects the $t^{1/2}$ curve at $t = t_1$.

Equating (5.20) and (5.24) gives

$$t_1 = \tau_\delta \equiv 4 C_I \delta^2 / \pi K_I . \quad (5.27)$$

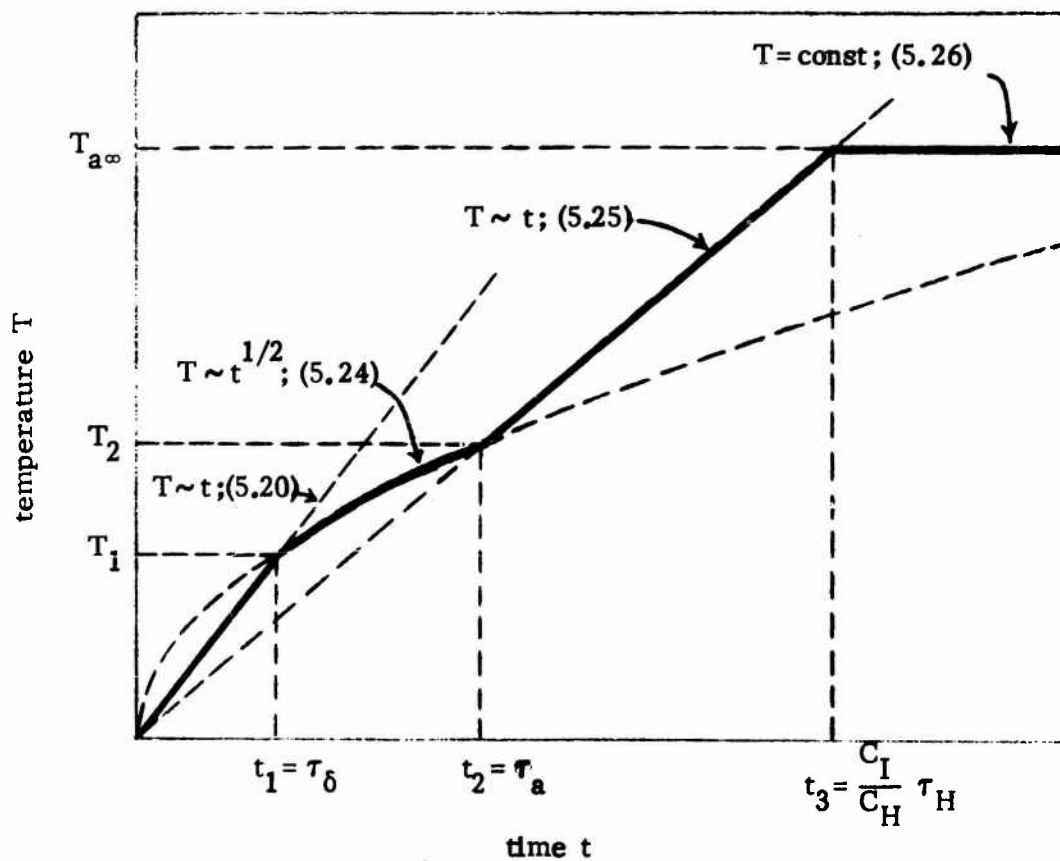


Fig. 4. Schematic illustration of the temperature at the surface of spherical inclusion with uniform heat generation within skin depth $\delta \ll a$ at the surface. The approximation $C_I K_I \gg C_H K_H$ is made in the values of the parameters. See Eqs. (5.26)-(5.31).

At $t = t_1$, these extrapolations give

$$T_1 = \frac{1 \delta \sigma_{\text{abs}}}{\pi^2 a^2} \frac{1}{K_I} \frac{\sqrt{C_I K_I}}{(\sqrt{C_I K_I} + \sqrt{C_H K_H})} \cong \frac{1 \delta \sigma_{\text{abs}}}{\pi^2 a^2 K_I} \quad (5.28)$$

At $t = t_2$, the extrapolated $t^{1/2}$ curve intersects the next linear region given by (5.25). Equating the temperatures in (5.24) and (5.25) at t_2 , we find

$$t_2 = \frac{4 a^2 C_I^2}{9 \pi (\sqrt{C_H K_H} + \sqrt{C_I K_I})^2} \cong \tau_a \quad (5.29)$$

At $t = t_2$, (5.29) and (5.25) give

$$T_2 = \frac{I \sigma_{\text{abs}} C_I}{3 \pi^2 a (\sqrt{C_H K_H} + \sqrt{C_I K_I})^2} \cong \frac{I \sigma_{\text{abs}}}{3 \pi^2 a K_I} \quad (5.30)$$

At $t = t_3$, the extrapolated linear curve (5.25) crosses the equilibrium value (5.26). Equating (5.25) and (5.26) yields

$$t_3 = \frac{C_I a^2}{3 K_H} = \frac{C_I}{C_H} \tau_H \quad (5.31)$$

and

$$T_3 = T_{a\infty}$$

For absorption in a metallic inclusion at $\lambda = 10 \mu\text{m}$, with $\delta = 4 \times 10^{-7} \text{ cm}$, $C_I = 2 \text{ J/cm}^3 \text{ K}$, $a = 10 \mu\text{m}$, $K_I = 2 \text{ W/cm K}$, and $K_H = 10^{-1} \text{ to } 10^{-3} \text{ W/cm K}$, (5.27), (5.29), and (5.31) give

$$\begin{aligned}
 t_1 &\cong 2 \times 10^{-13} \text{ sec} , & t_2 &\cong 10^{-7} \text{ sec} , \\
 t_3 &\cong 10^{-3} \text{ to } 10^{-5} \text{ sec} .
 \end{aligned}
 \tag{5.32}$$

The values of t_1 and t_2 are shorter than pulse lengths of current high-power pulsed CO_2 lasers. For a pulse length of $1 \mu\text{sec}$, the temperature is given by (5.25).

The various time regimes in Fig. 4 depend on inclusion size in such a way that if the pulse length is fixed, long times in Fig. 4 are associated with small inclusions. For example, the time t_3 at which the temperature reaches equilibrium is equivalent to an inclusion of radius $a = (3K_H t / C_I)^{1/2}$ for a pulse of duration t .

The above results also apply to dielectric inclusions with $\beta_I a \gg 1$, as well as to the metallic inclusion used in the examples. However, in the case of strongly absorbing dielectrics the following differences should be noted: First, the approximation $K_I \gg K_H$ is not generally valid and $K_I \cong K_H$ is perhaps more generally true. Second, the radiation penetrates to a greater depth into the inclusion. Generally $\beta < 10^4 \text{ cm}^{-1}$ so that the radiation penetration depth is usually greater than $1 \mu\text{m}$, as compared to $\sim 40 \text{ \AA}$ for good conductors. As a result, the first linear region of Fig. 4, (5.20), which was only of academic interest in the case of metals, will be important, and the size at which volume heating rather than surface heating applies will occur at a larger radius.

For repetitively pulsed lasers, the above results may be applied directly to each pulse if the temperature relaxes to the initial value between pulses. In the case of a fast repetition rate, the temperature will not relax and the failure

Sec. C

temperatures will be reached at a lower intensity than calculated for single pulse. This will occur for two cases: First, if the time between pulses is less than τ_H , heat will not diffuse away from the inclusion before the next pulse. Second, for a large density of inclusions, heat that diffuses away from one inclusion appears at another, and the background temperature of the entire window is increased. This occurs when the time between pulses is greater than about $C_H \ell^2 / 4 K_H$, where ℓ is the distance between inclusions, but less than the time constant for cooling the window.

In the following contractual period the dielectric or metallic inclusion temperature will be calculated as a function of inclusion radius for various pulse durations. The heating of platinum inclusions in a glass host by 30 nsec duration pulses has also been considered by Hopper and Uhlmann.³⁷ They assumed $\sigma_{\text{abs}} = \pi a^2 \epsilon_\lambda$ (ϵ_λ = emissivity) which is not valid for small inclusions (long times). Using the absorption cross sections discussed in Sec. II, our preliminary results indicate that the plot of temperature versus size in their example does not have a maximum as they found, but instead T is a monotonically increasing function of a .

Preliminary calculations show that micron-size metal or dielectric inclusions can typically be heated to the failure temperature of 1,000 K by a single microsecond pulse with $I t$ less than 50 J/cm^2 ($I = 5 \times 10^7 \text{ W/cm}^2$ with $t = 1 \mu\text{sec}$). In cases of optimum heating, local material failure can occur at microsecond duration - pulse energies as low as 5 J/cm^2 . Even though the failure temperature is reached in repetitively pulsed systems of these energies, cw systems with the same average intensity will only heat the inclusions to about 1 K.

As mentioned by Bloembergen,³⁸ local electric field enhancement for inclusions near imperfections such as cracks in the host material could lower the calculated material damage pulse energy by as much as a factor of 100.

VI. Conclusions

Small amounts of macroscopic inclusions in or on the surface of transparent crystals can cause substantial absorption. For example, a fractional volume of $f \sim 10^{-7}$ to 10^{-8} , which corresponds roughly to $\sim 10^{15}$ to 10^{16} impurity atoms per cm^3 , can give rise to $\beta = 10^{-4} \text{ cm}^{-1}$ for some types of inclusions. The corresponding effective average cross sections per atom, $\sim 10^{-19}$ to 10^{-20} cm^2 , are quite large.

Simple expressions for the absorption cross sections of spherical inclusions were derived for the cases of $ka \ll 1$ [Eq. (2.4)] and of $ka \gg 1$ [Eq. (2.16)]. The results were used to derive expressions for β for the four cases of large inclusions ($ka \gg 1$) of weak and strong absorbers and of small inclusions ($ka \ll 1$) of dielectric and metallic particles. The results are summarized in Table I, which contains expressions for β , typical temperature and frequency dependences, and typical numerical results.

The result that the cross section (2.6) for $ka, \beta_1 a \gg 1$ contains R_{\perp} , rather than $\langle R \rangle$, is of general interest in the theory of scattering.

The local heating of macroscopic inclusions is a far greater problem in high-intensity short-pulse systems than in low-intensity long-pulse or cw systems having equal average intensity. Preliminary results indicate that material failure can occur for pulse energies as low as 5 J/cm^2 with microsecond pulse durations. Bloembergen has suggested that local electric field enhancement near imperfections such as cracks in the host material could lower the calculated material damage pulse energy by as much as a factor of 100. The determination of the thresholds for damage in typical window materials will be further explored during the next contractual period.

Table I. Tabulation of expressions for β , typical T and ω dependence of β , and typical values of parameter [in brackets] that give $\beta \approx 10^{-4} \text{ cm}^{-1}$.

Large Inclusions ($ka \gg 1$)		Small Inclusions ($ka \ll 1$)	
Weak Absorber $\beta_I a \ll 1$	Strong Absorber $\beta_I a \gg 1$	Dielectric Inclusions $\epsilon_g \approx 1$	Metallic Inclusions at IR $\epsilon \approx -\frac{\omega_p^2}{\omega^2 + i\omega\Gamma}$
$\beta \approx \frac{3}{4} (1 - R_L) f \beta_I \quad (3.2)$ <p>(a)</p> $\beta \sim T^p \quad (a)$ $\beta \sim e^{-\omega/\omega_0}$ <p>$\left[\frac{4}{3} (1 - R_L) \approx 1, \right.$ $\beta_I = 10 \text{ cm}^{-1}$ $f = 10^{-5} \left. \right]$</p>	$\beta \approx \pi a^2 (1 - R_L) N_I \quad (3.1)$ <p>(b)</p> $\beta \sim T^0$ <p>(c)</p> $\beta \sim \omega^0$ <p>[One inclusion per cubic centimeter with $a = 50 \mu\text{m}$ and $1 - R_L \approx 1$. The value of f is 5×10^{-7}.]</p>	$\beta \approx \frac{9 \text{Re} n}{(\epsilon_R + 2)^2 + \epsilon_g^2} f \beta_I \quad (3.4)$ <p>(a)</p> $\beta \sim T^p$ $\beta \sim e^{-\omega/\omega_0}$ <p>$[9\epsilon_g [(\epsilon_R + 2)^2 + \epsilon_g^2]^{-1} \approx 1,$ $\beta_I = 10^3 \text{ cm}^{-1}, f = 10^{-7} \left. \right]$</p>	$\beta \approx \frac{9 n_H^3 \Gamma \omega^2 f}{c \omega_p^2} \quad (3.6)$ <p>(b)</p> $\beta \sim T^0$ $\beta \sim \omega$ <p>$[\Gamma = 5 \times 10^{14} \text{ sec}^{-1},$ $\omega = 2 \times 10^{14} \text{ rad/sec},$ $\omega_p = 5 \times 10^{15} \text{ rad/sec},$ $f = 2 \times 10^{-7} \left. \right]$</p>

- (a) $p \sim 2 - 4$ typically at high temperature
(b) for $\Gamma = \Gamma_{\text{Su}}$ in the case of metals
(c) For the case of $\omega^2 \ll \Gamma^2$ in metals, $\beta \sim \omega^{1/2}$

D. COLLECTION OF EXPERIMENTAL RESULTS FOR $\beta(\omega)$

Information on the frequency dependence of the absorption coefficient has been collected from the literature. All these results have been plotted on the same scale for convenience of comparison. Figs. 1-17 contain all the results collected to date. Figs. 18-22 give comparisons of alkali halides, alkaline earth fluorides, zincblend-structure semiconductors, and type IV elemental semiconductors plus Ba Ti O_3 , respectively. Fig. 23 shows a comparison of one material from each of the above groups, plus Ba Ti O_3 . In this last curve, the elements in KBr, ZnSe, and Ge are from the same row in the periodic table. The lozenges denote the $10.6 \mu\text{m}$ values from references 39 and 43.

For Figs. 1-7, the solid-curve data was presented in the original references as graphs of conductivity 2σ vs ω or imaginary part of the dielectric constant ϵ_j vs ω . According to the relations,

$$\beta = \frac{2\pi(2\sigma)}{n_r}, \quad \beta = \frac{\omega \epsilon_j}{cn},$$

the values of the index of refraction $n_r(\omega)$ are needed to obtain the values of β . Since the values of $n(\omega)$ used in these references were not given, the following values (lowest-wavelength values from AIP Handbook) were used formally:

$n_r = 1.5$ for KBr; $n_r = 1.2$ for KCl and NaCl; $n_r = 1.1$ for LiF; $n_r = 1.4$ for BaF_2 ; $n_r = 1.4$ for SrF_2 ; and $n_r = 1.3$ for CaF_2 . Notice that this solid-curve data is in the vicinity of the main resonance, where n_r is a strong function of ω .

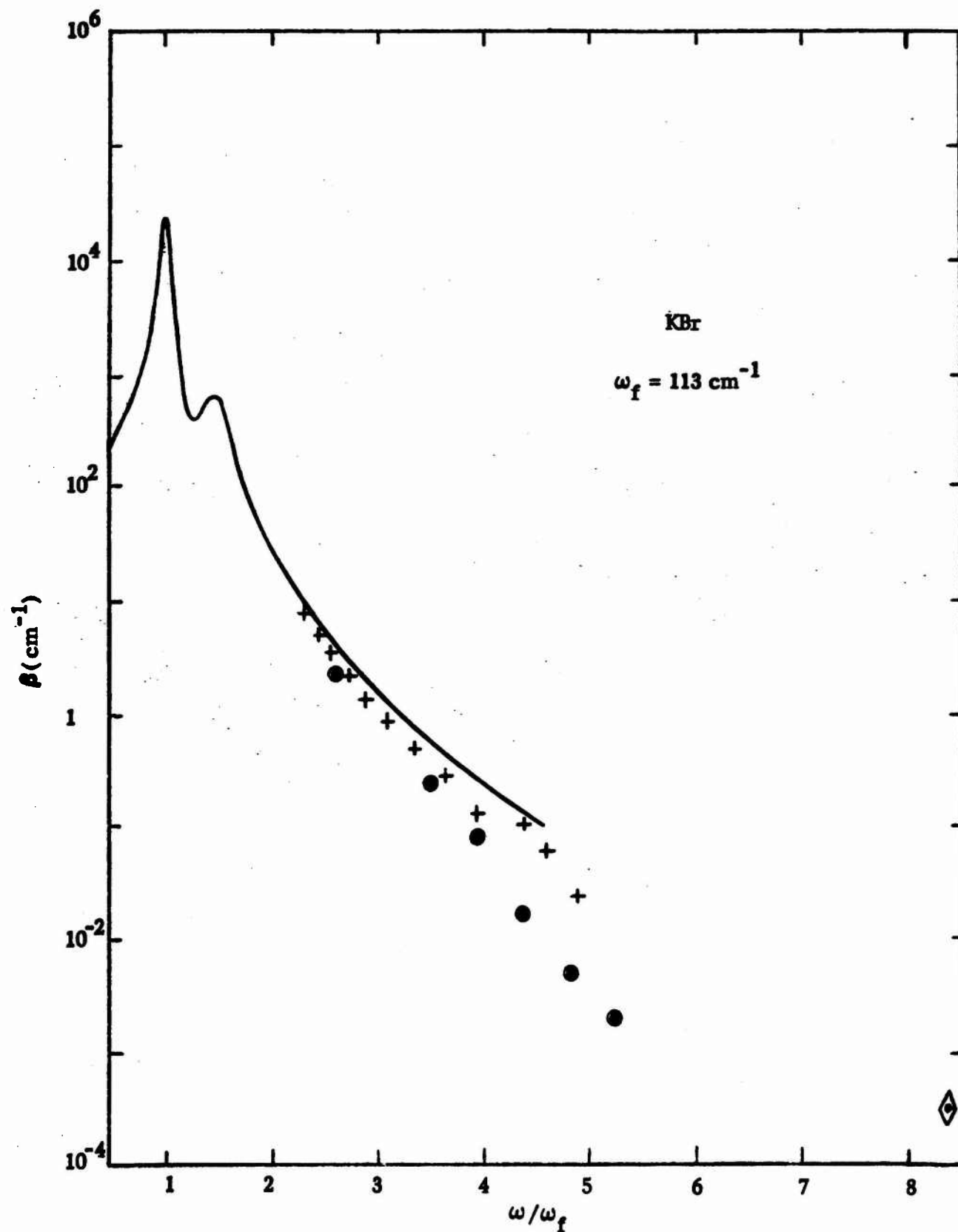


Fig. 1. Experimental frequency dependence of the infrared absorption coefficient β for KBr after Horrigan and Deutsch (+, \odot) Ref. 39, and Genzel (—), Ref. 40.

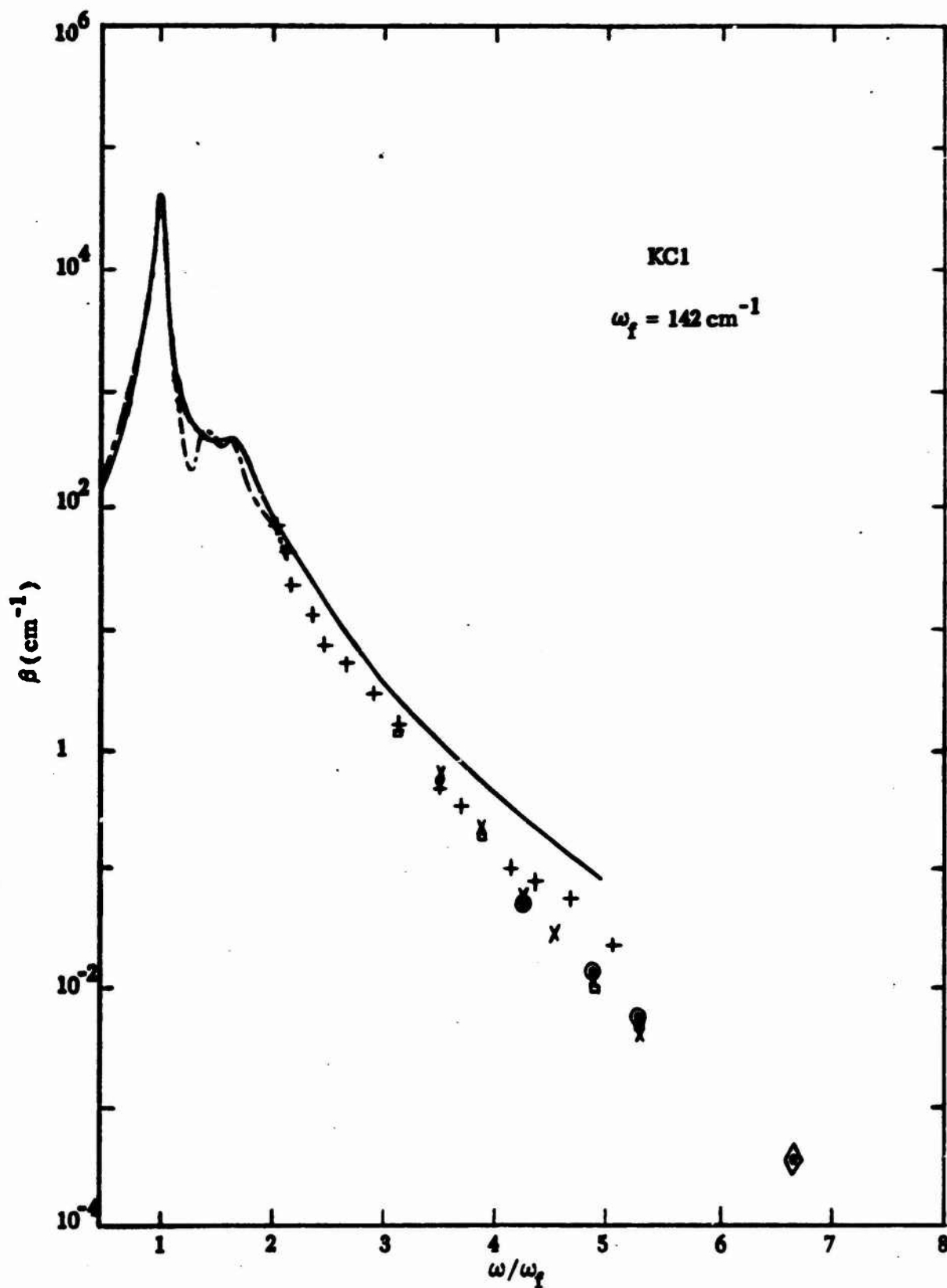


Fig. 2. Experimental frequency dependence of the infrared absorption coefficient β for KCl after Horrigan and Deutsch (+, x, ⊙, □) Ref. 39, Smart et al (- · -) Ref. 41, and Genzel (—) Ref. 40.

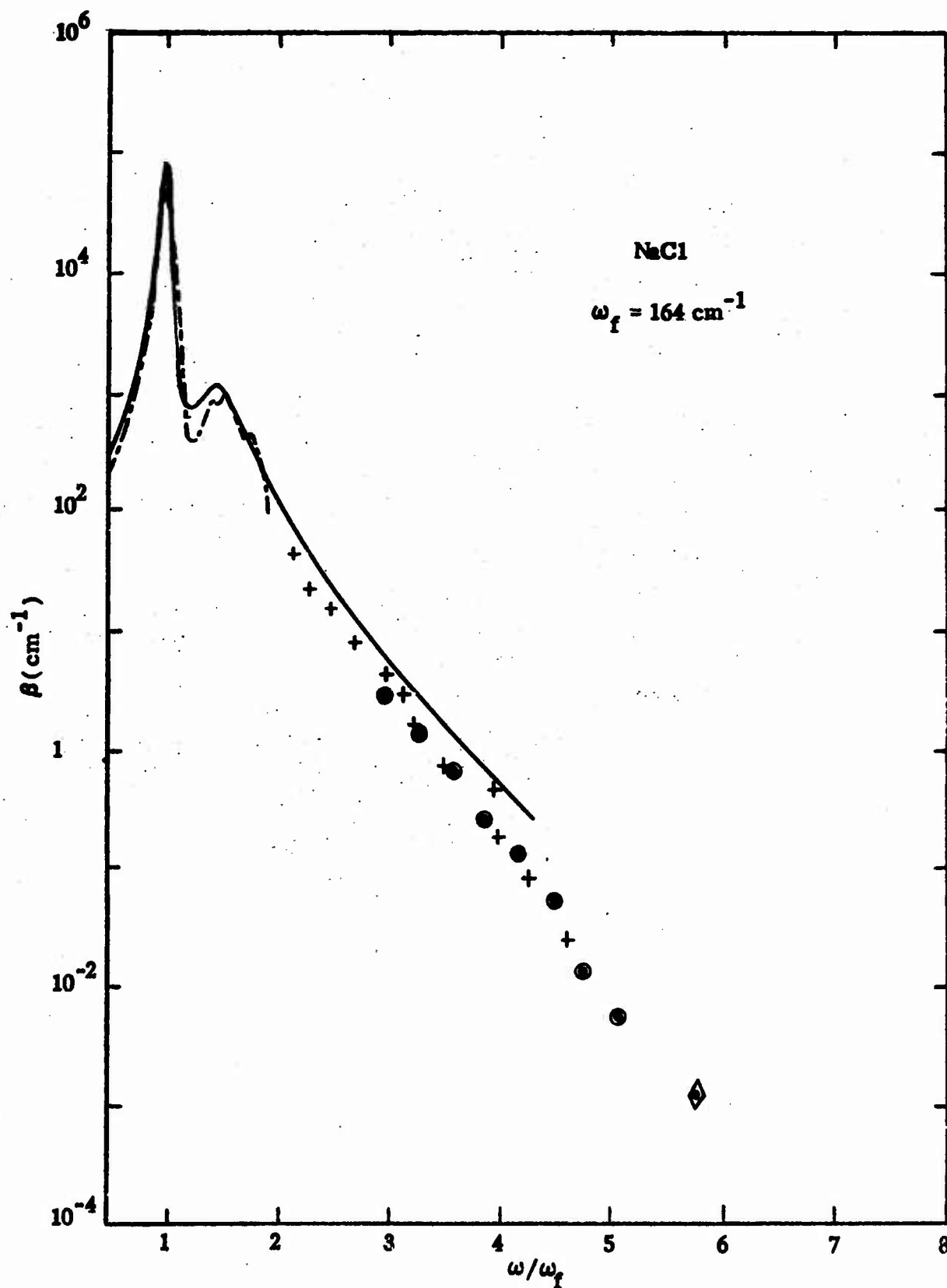


Fig. 3. Experimental frequency dependence of the infrared absorption coefficient β for NaCl after Horrigan and Deutsch (+, ●) Ref. 39, Smart et al (— · —) Ref. 41, and Genzel (—) Ref. 40.

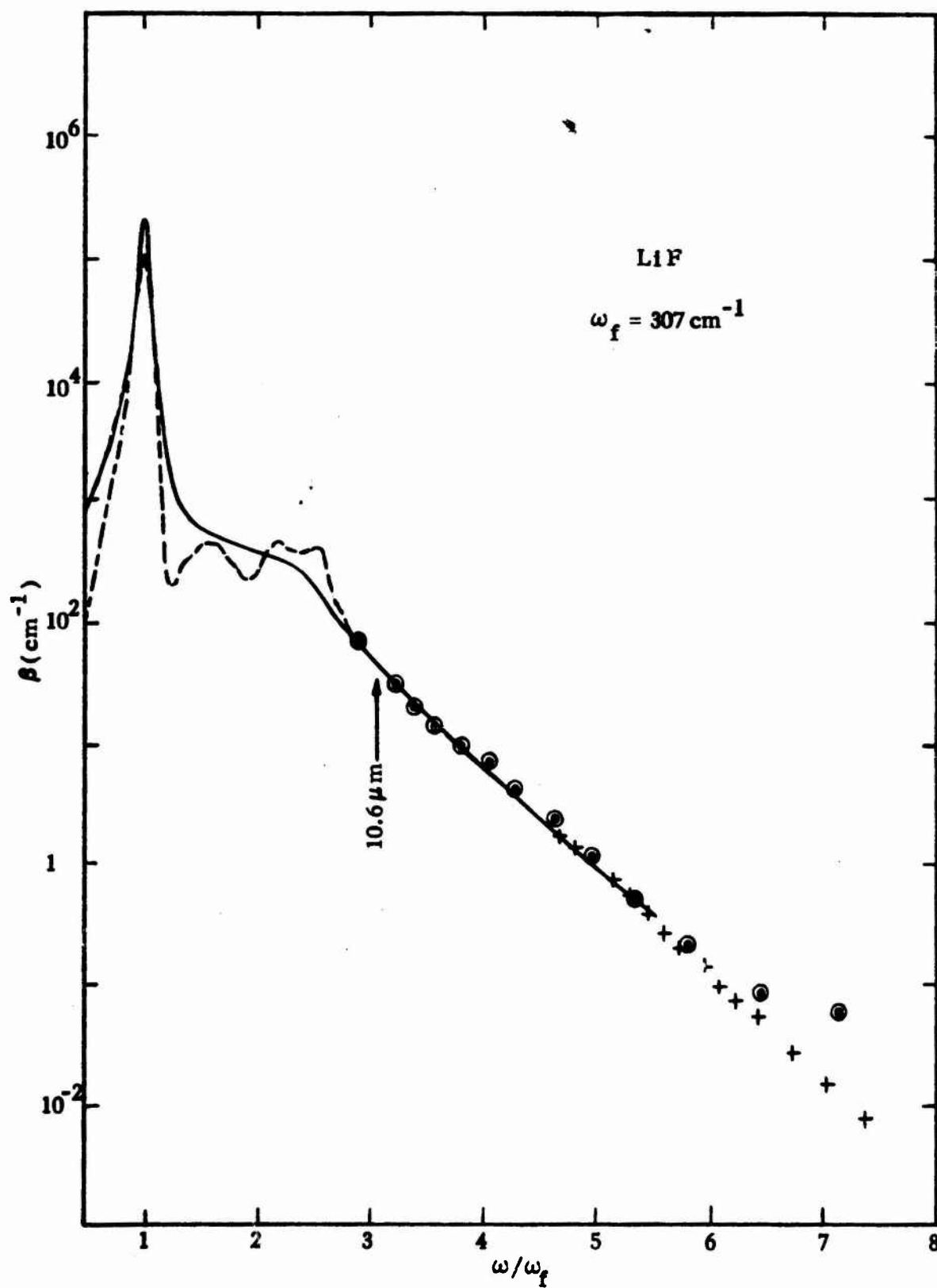


Fig. 4. Experimental frequency dependence of the infrared absorption coefficient β for LiF after Horrigan and Deutsch (+, \odot) Ref. 39, Smart et al (— \leftarrow —) Ref. 41, and Genzel (—) Ref. 40.

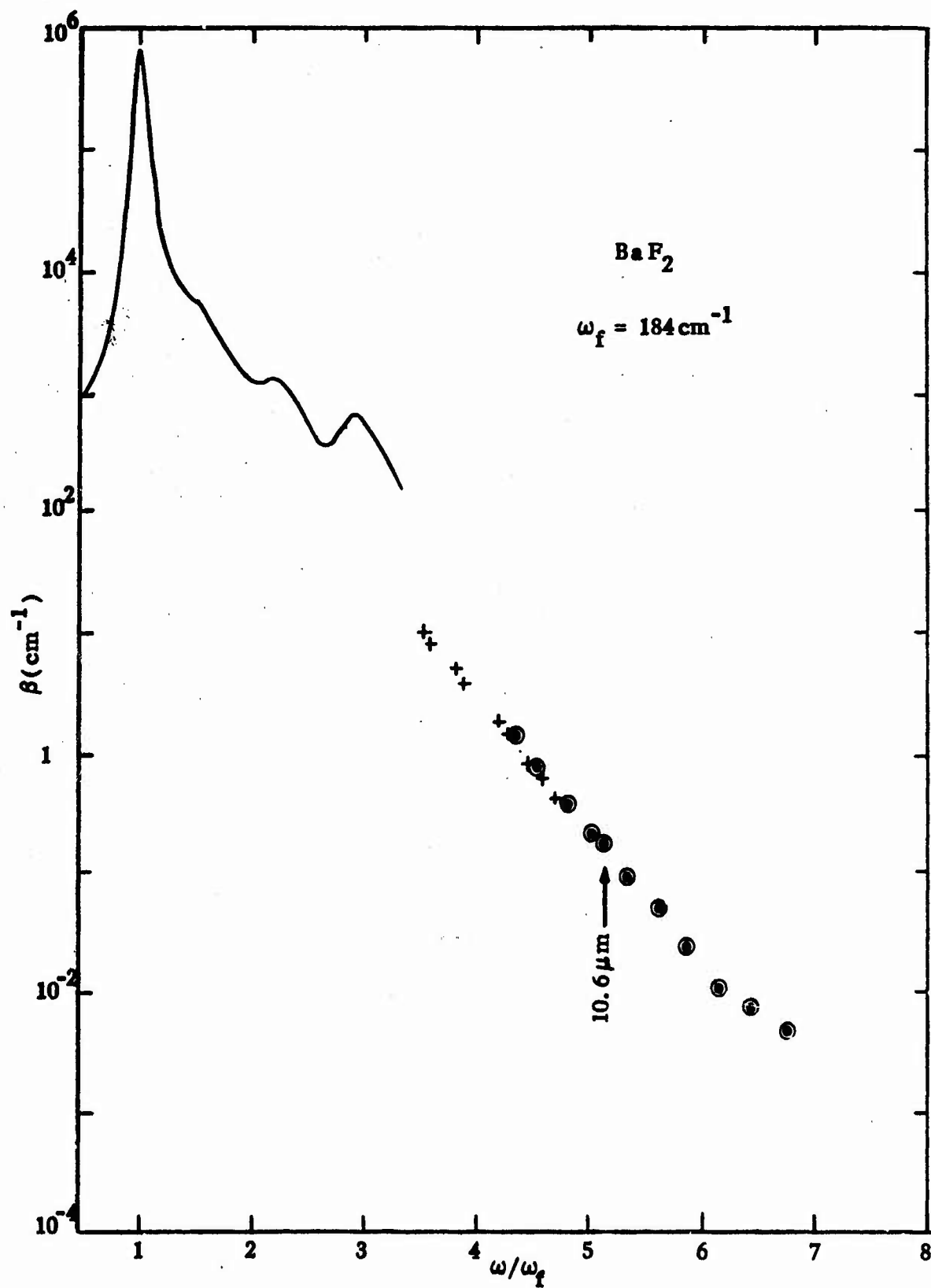


Fig. 5. Experimental frequency dependence of the infrared absorption coefficient β for BaF_2 after Horrigan and Deutsch (+, \odot), Ref. 39, and Denham et al (-) Ref. 42.

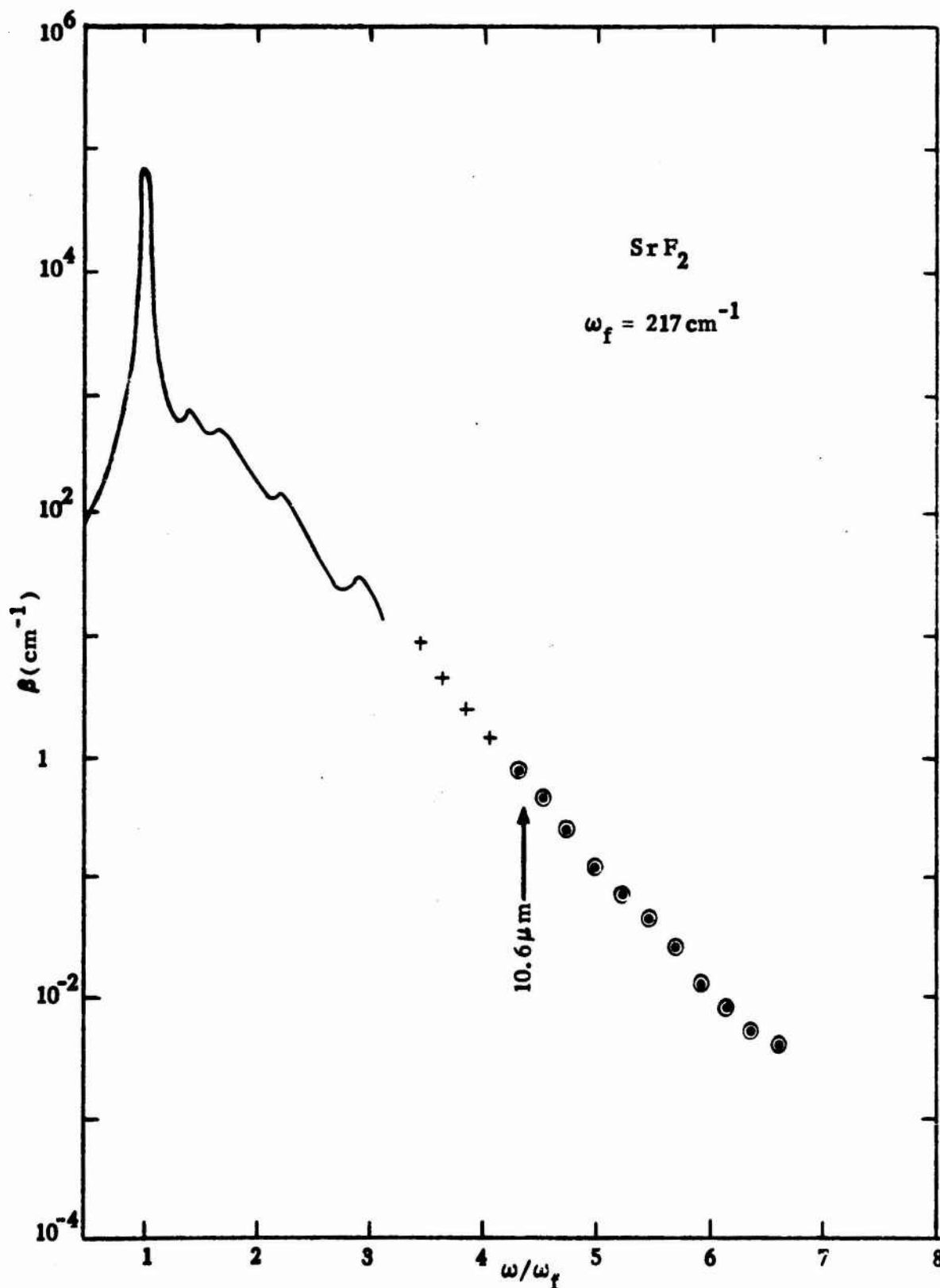


Fig. 6. Experimental frequency dependence of the infrared absorption coefficient β for SrF_2 after Horrigan and Deutsch (+, \odot) Ref. 39, and Denham et al (—) Ref. 42.

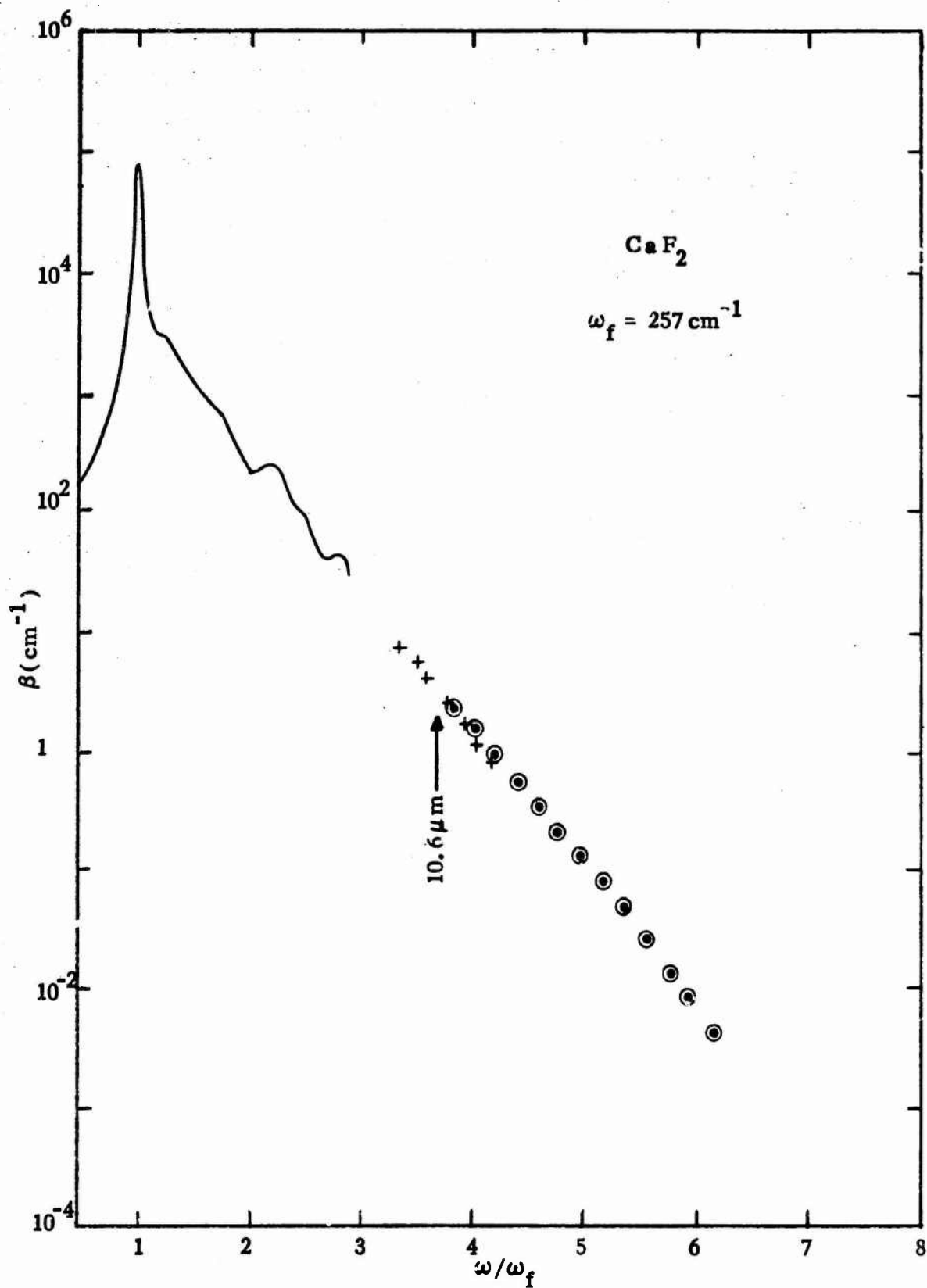


Fig. 7. Experimental frequency dependence of the infrared absorption coefficient β for CaF_2 after Horrigan and Deutsch (+, \odot) Ref. 39, and Denham et al (—) Ref. 42.

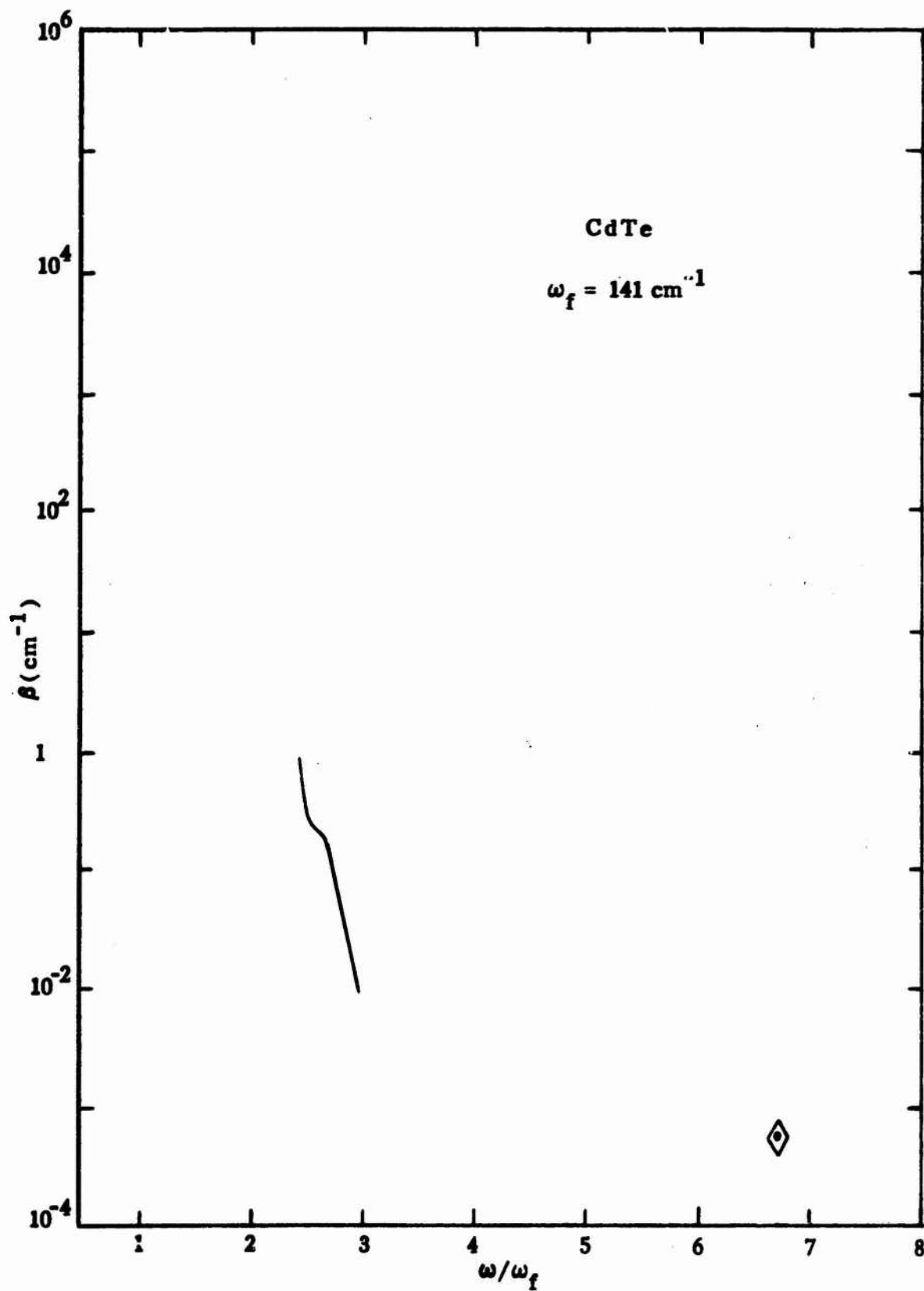


Fig. 8. Experimental frequency dependence of the infrared absorption coefficient β for CdTe after Horrigan and Deutsch, Ref. 48.

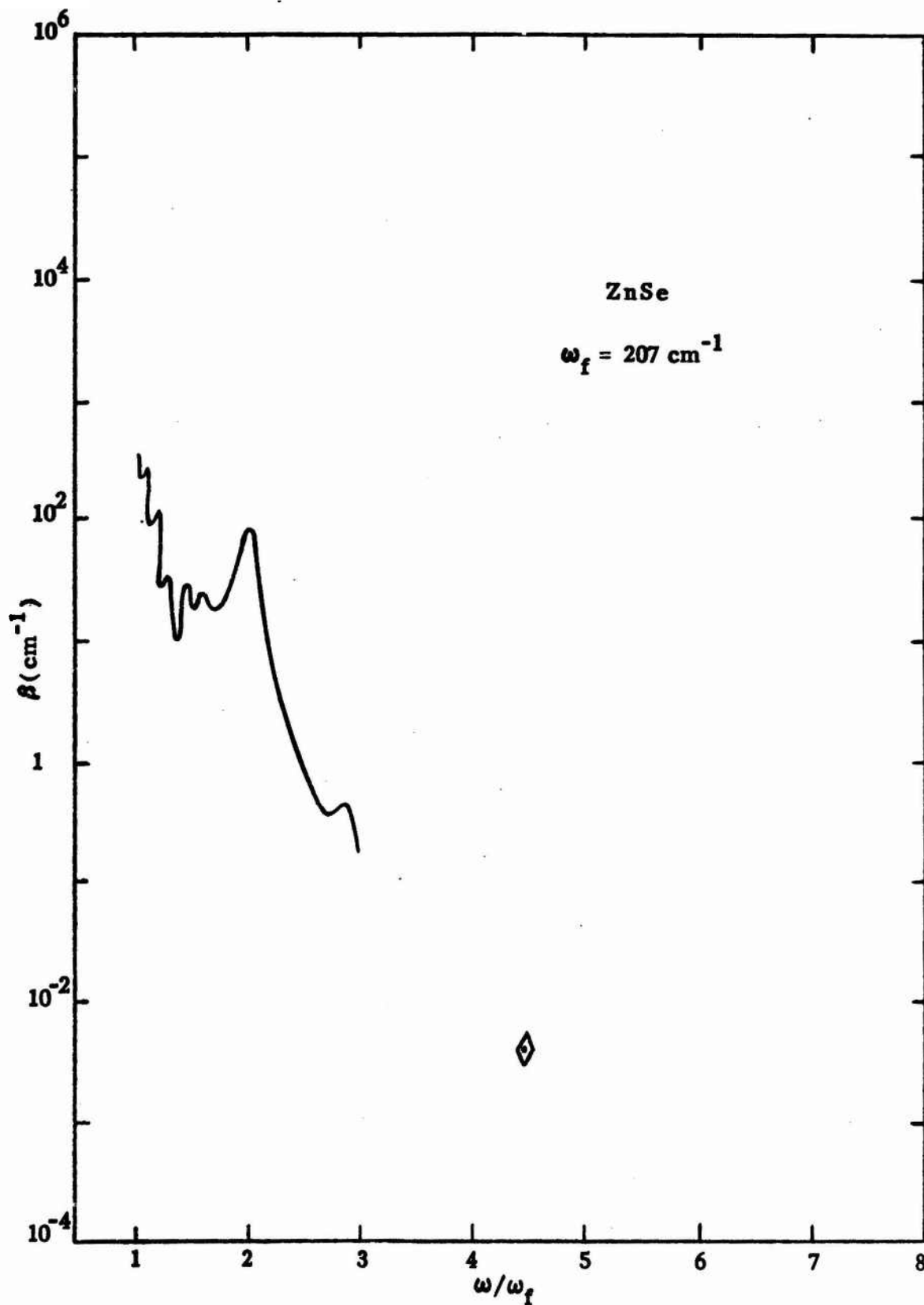


Fig. 9. Experimental frequency dependence of the infrared absorption coefficient β for ZnSe after Horrigan and Deutsch, Ref. 43.

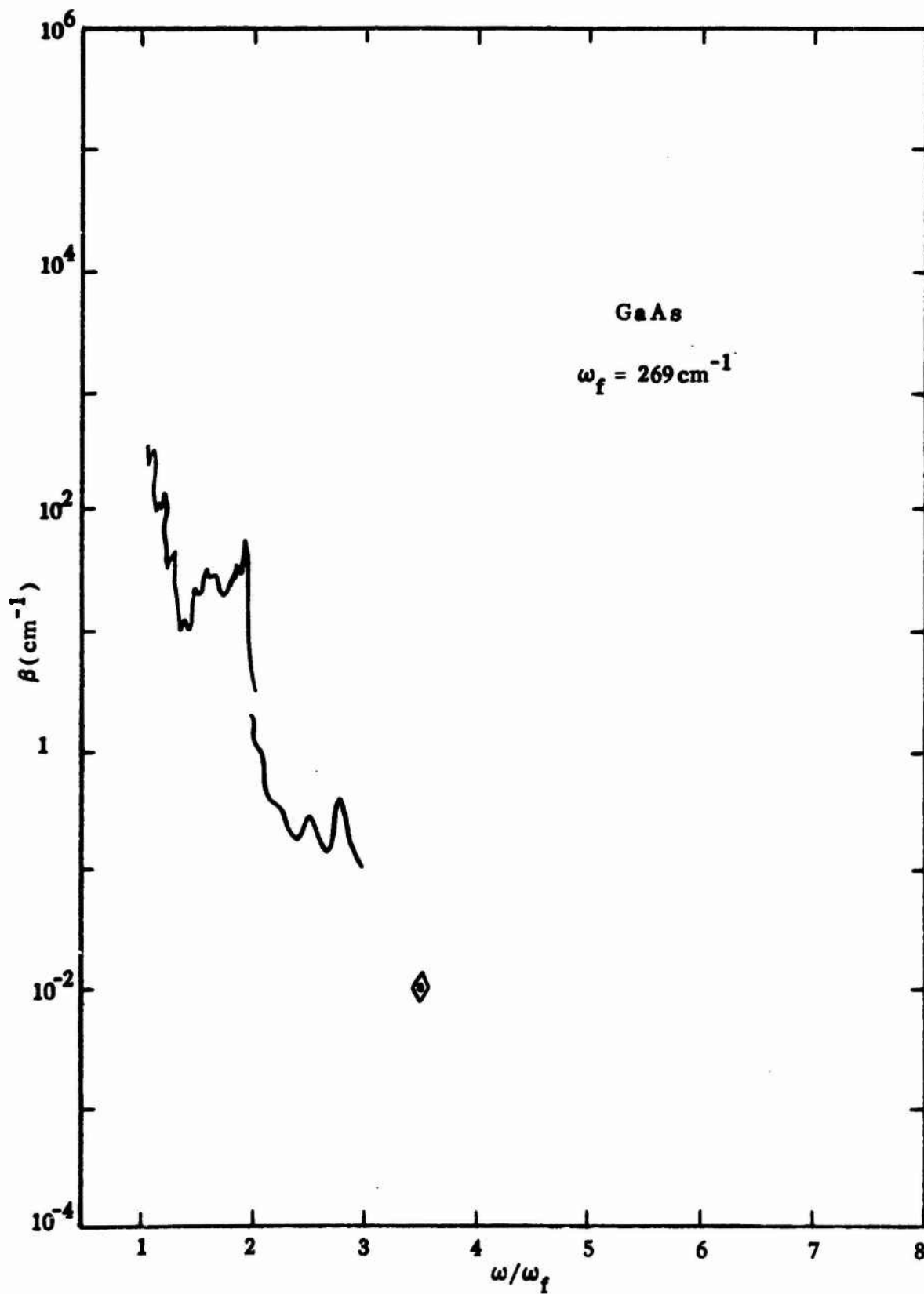


Fig. 10. Experimental frequency dependence of the infrared absorption coefficient β for GaAs after Johnson, Ref. 44.

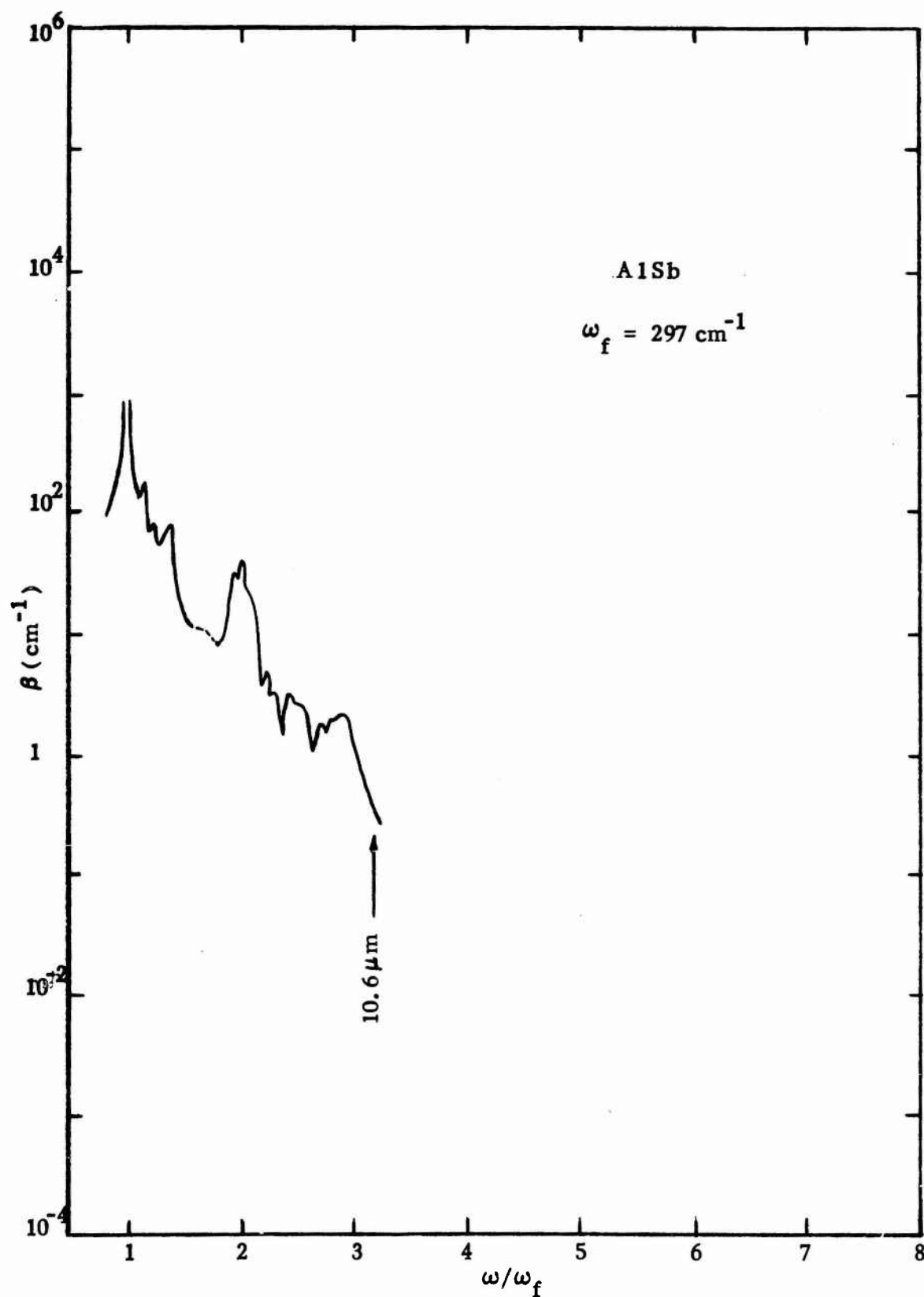


Fig. 11. Experimental frequency dependence of the infrared absorption coefficient β for AlSb after Turner and Reese, Ref. 45.

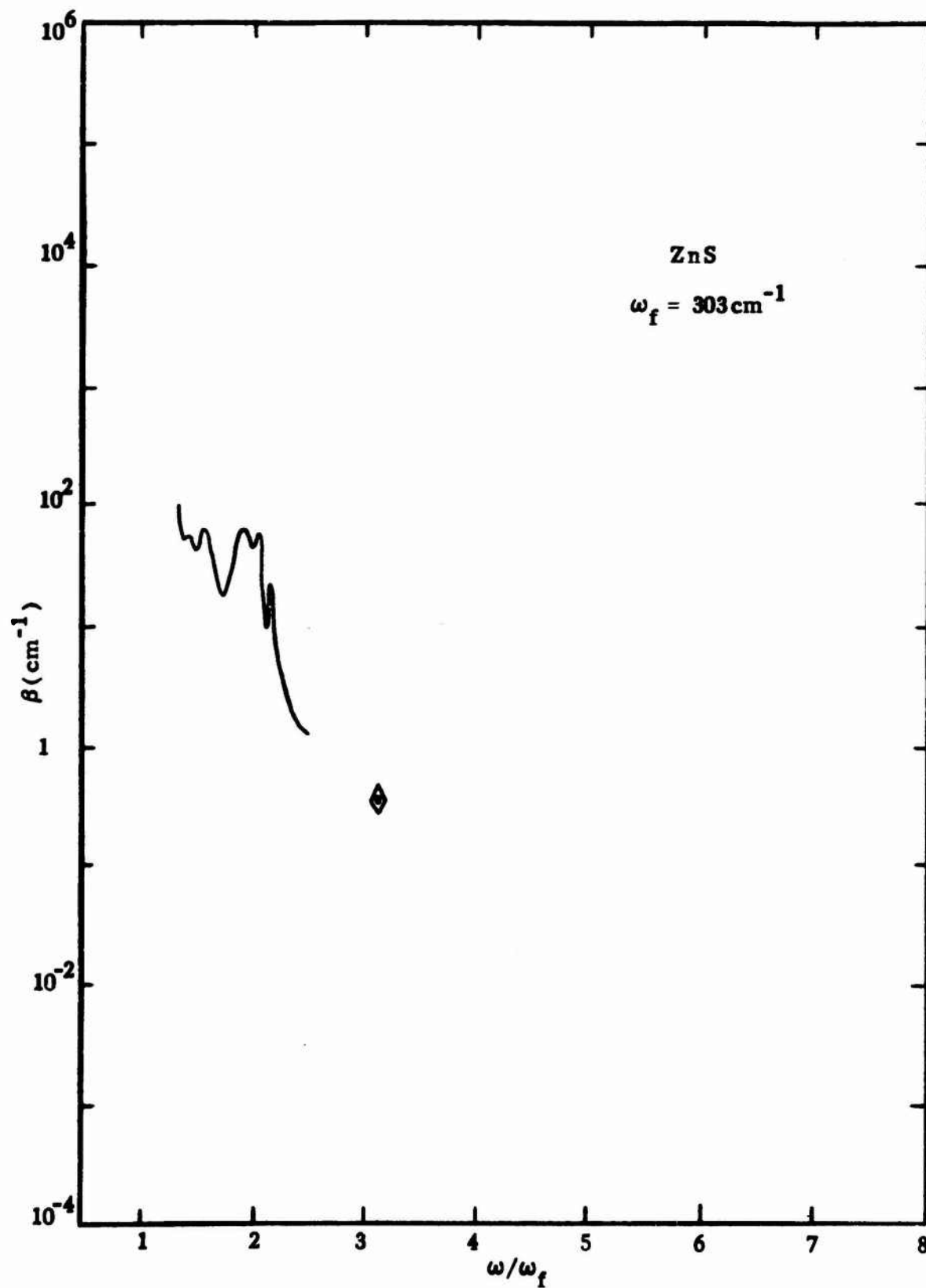


Fig. 12. Experimental frequency dependence of the infrared absorption coefficient β for ZnS after Deutsch, Ref. 46.

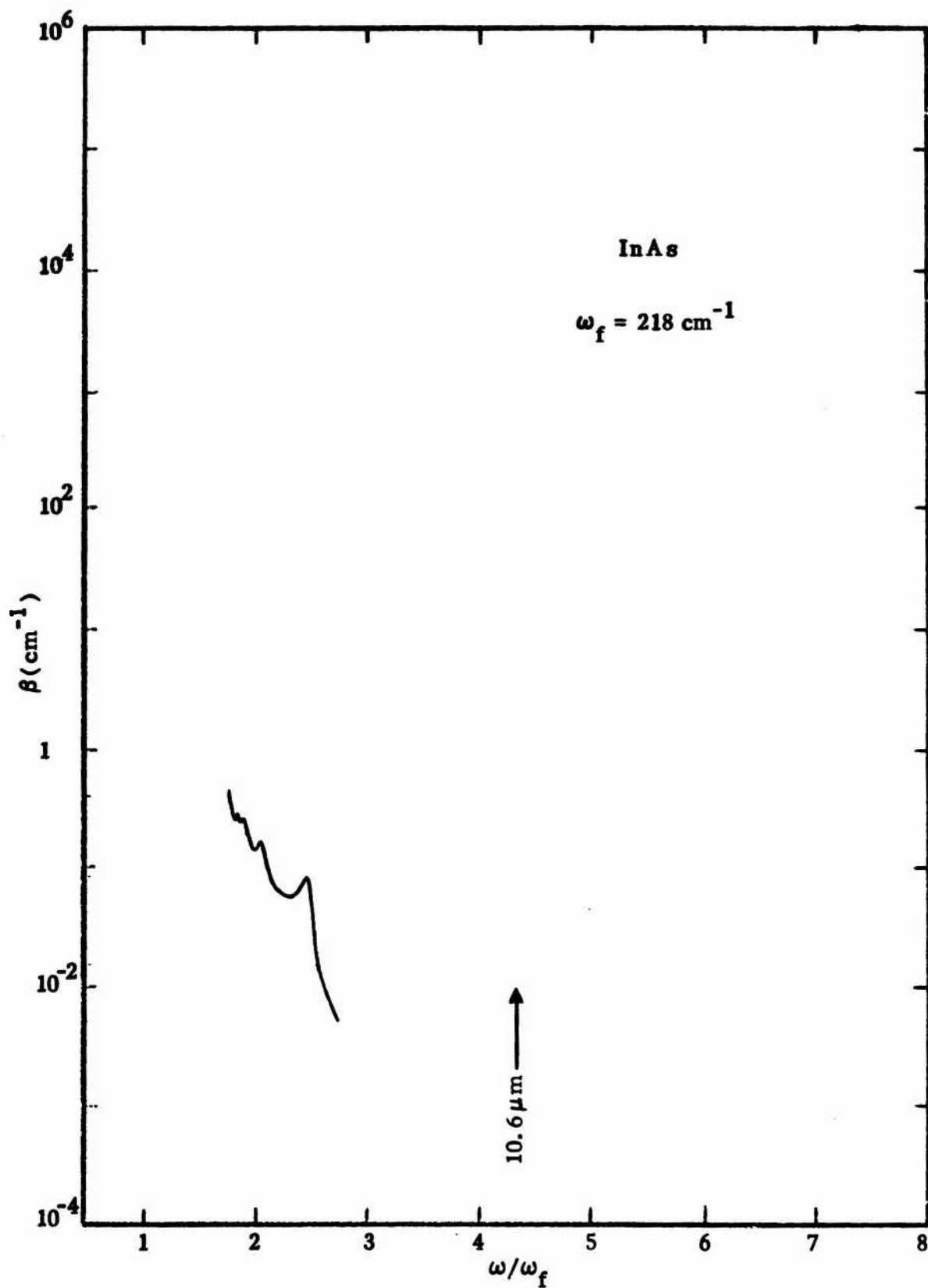


Fig. 13. Experimental frequency dependence of the infrared absorption coefficient β for InAs after Johnson, Ref. 44.

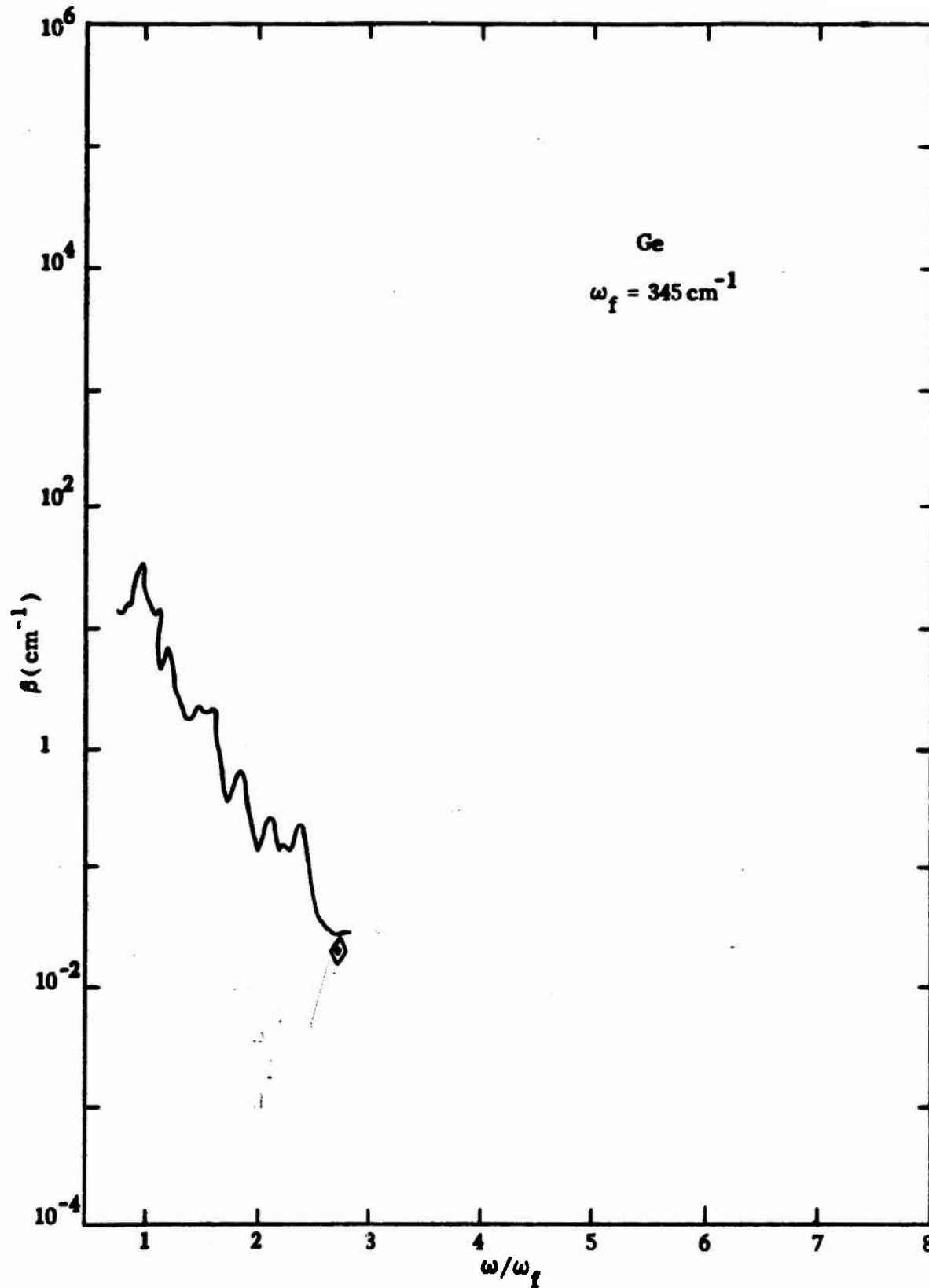


Fig. 14. Experimental frequency dependence of the infrared absorption coefficient β for Ge after Johnson, Ref. 44.

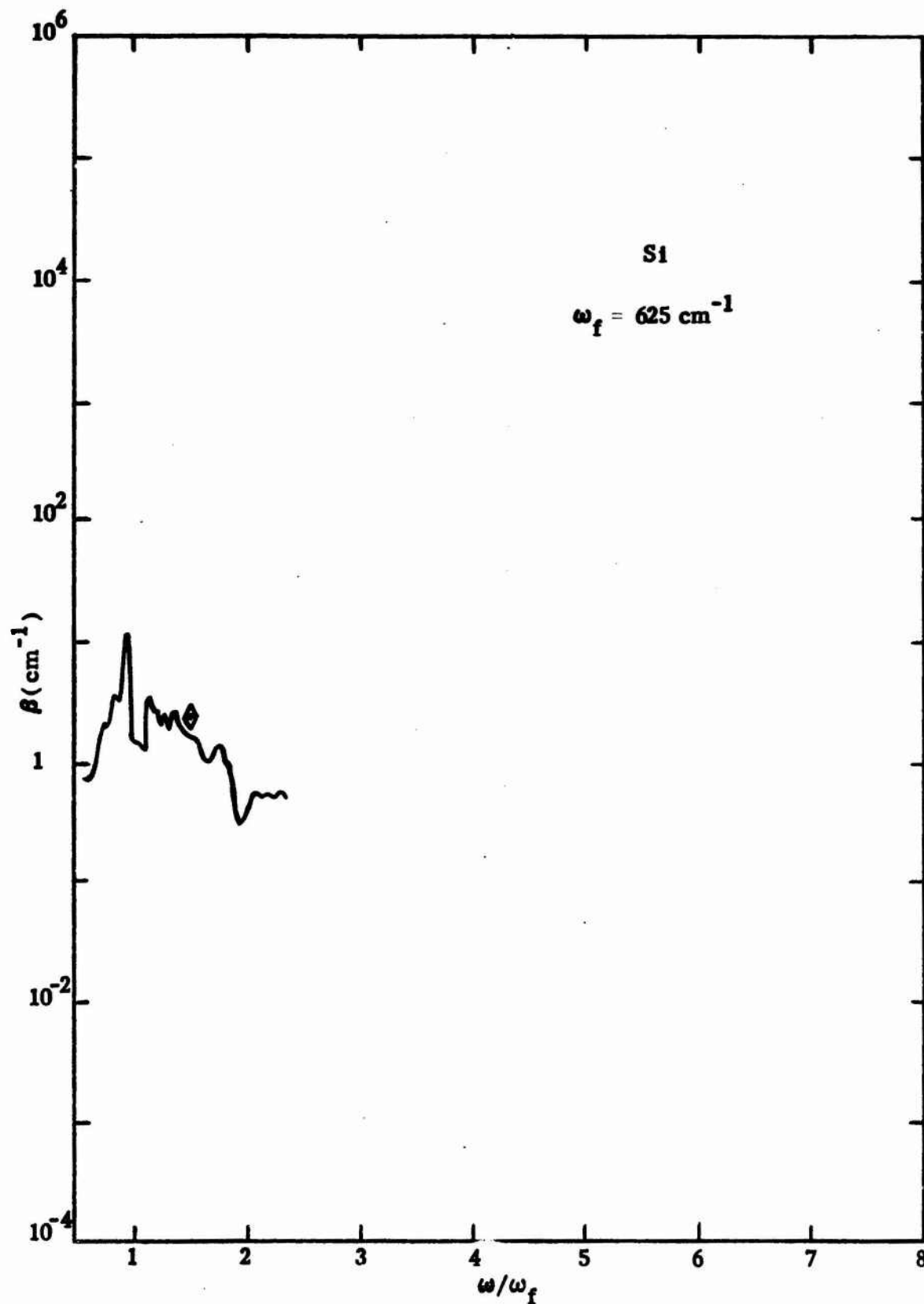


Fig. 15. Experimental frequency dependence of the infrared absorption coefficient β for Si after Johnson, Ref. 44.

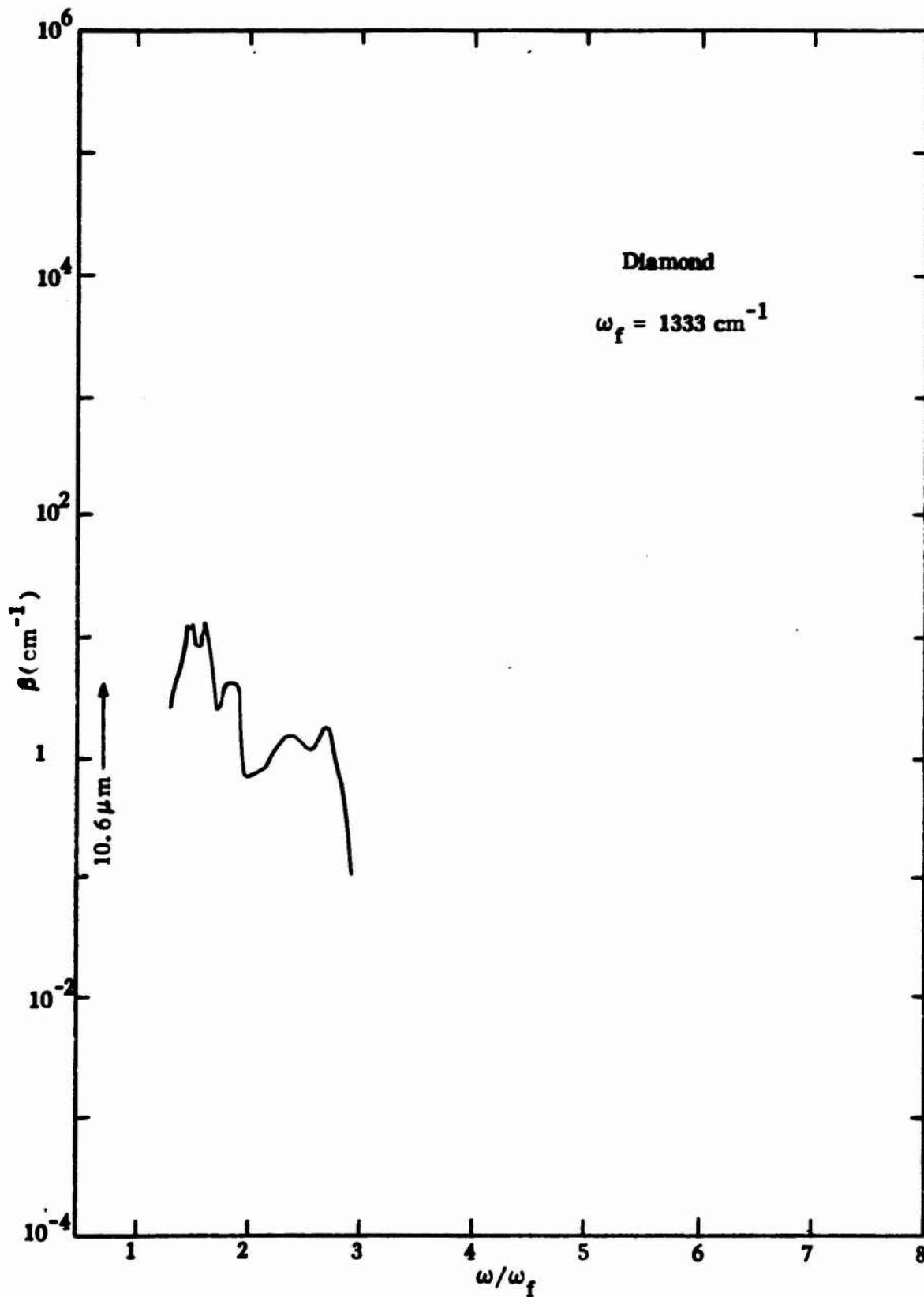


Fig. 16. Experimental frequency dependence of the infrared absorption coefficient β for diamond after Johnson, Ref. 44.

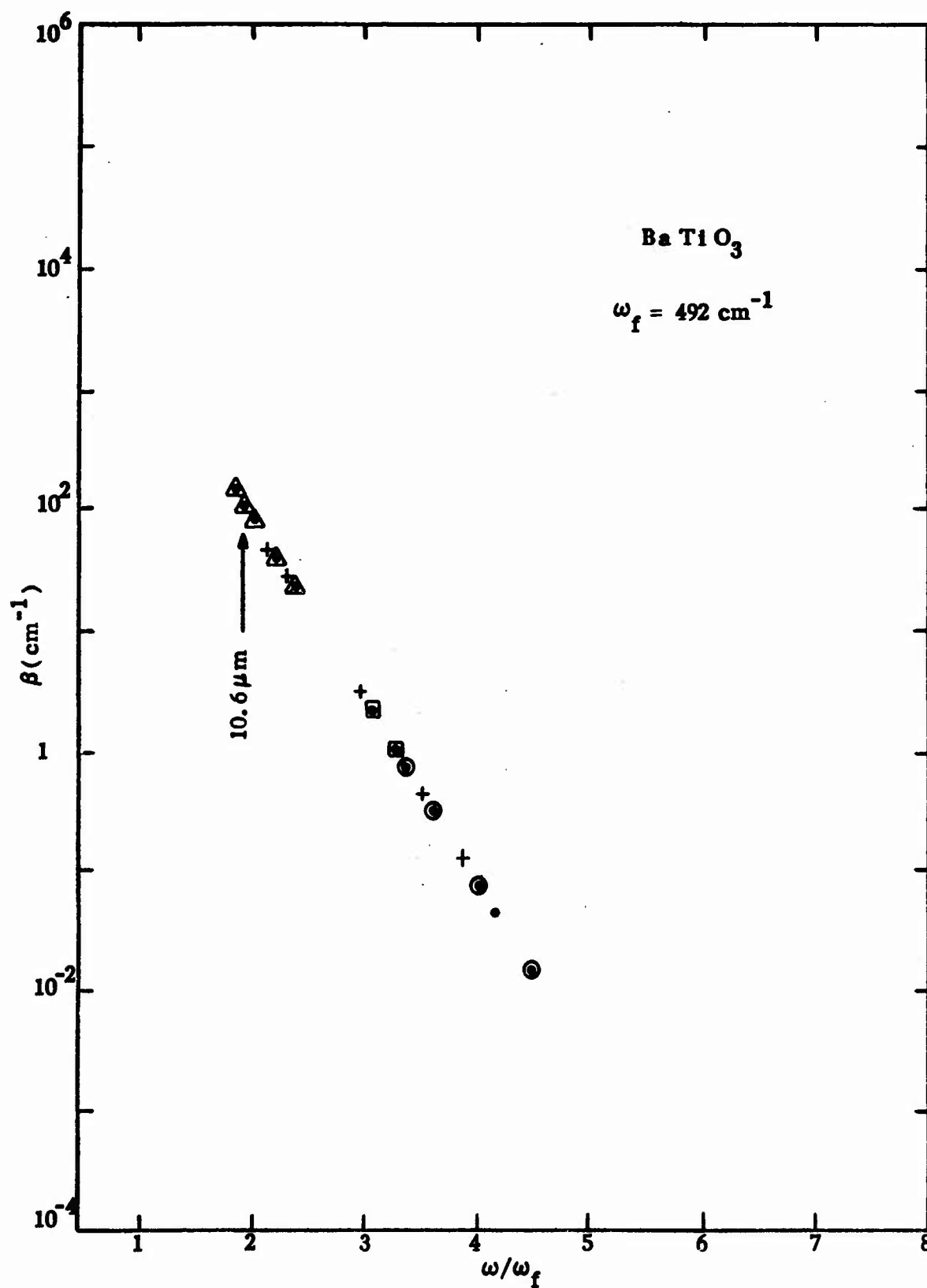


Fig. 17. Experimental frequency dependence of the infrared absorption coefficient β for BaTiO_3 after Rupprecht, Ref. 4.

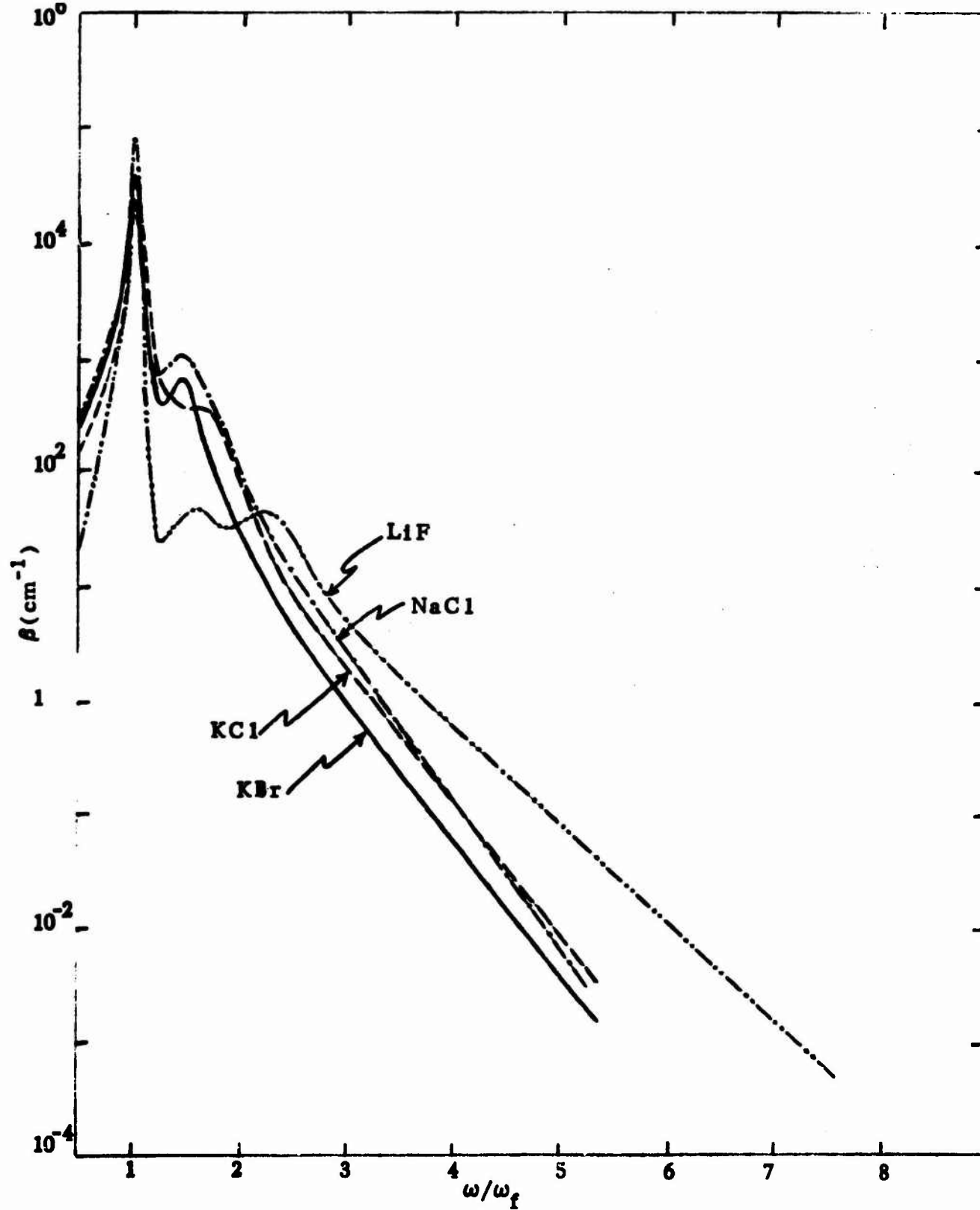


Fig. 18. Comparison of the absorption of the alkali halides, from Figs. 1-4. The curves here are smoothed curves through the loci of the lowest points in Figs. 1-4.

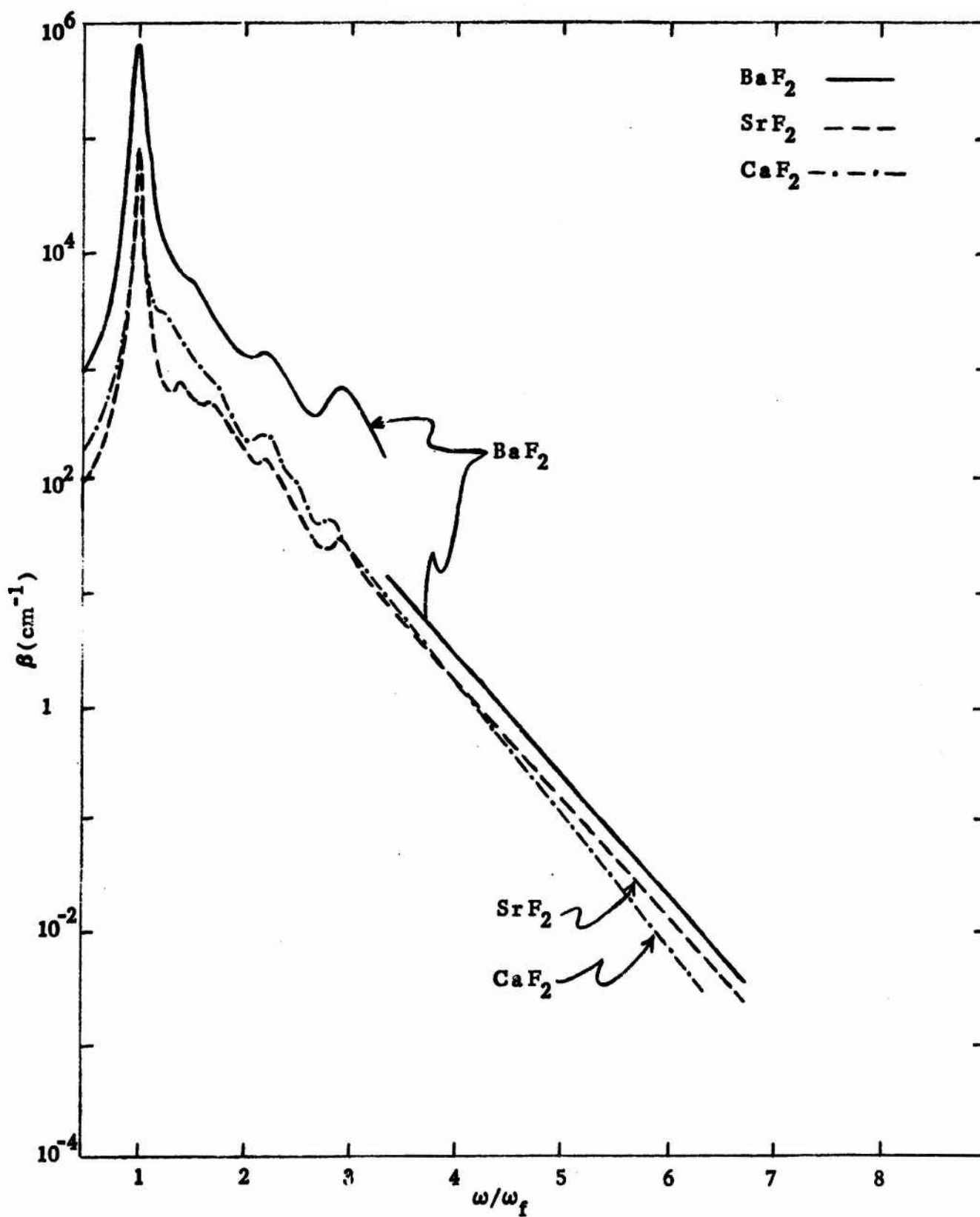


Fig. 19. Comparison of the absorption of the alkaline earth fluorides, from the curves in Figs. 5, 6, and 7.

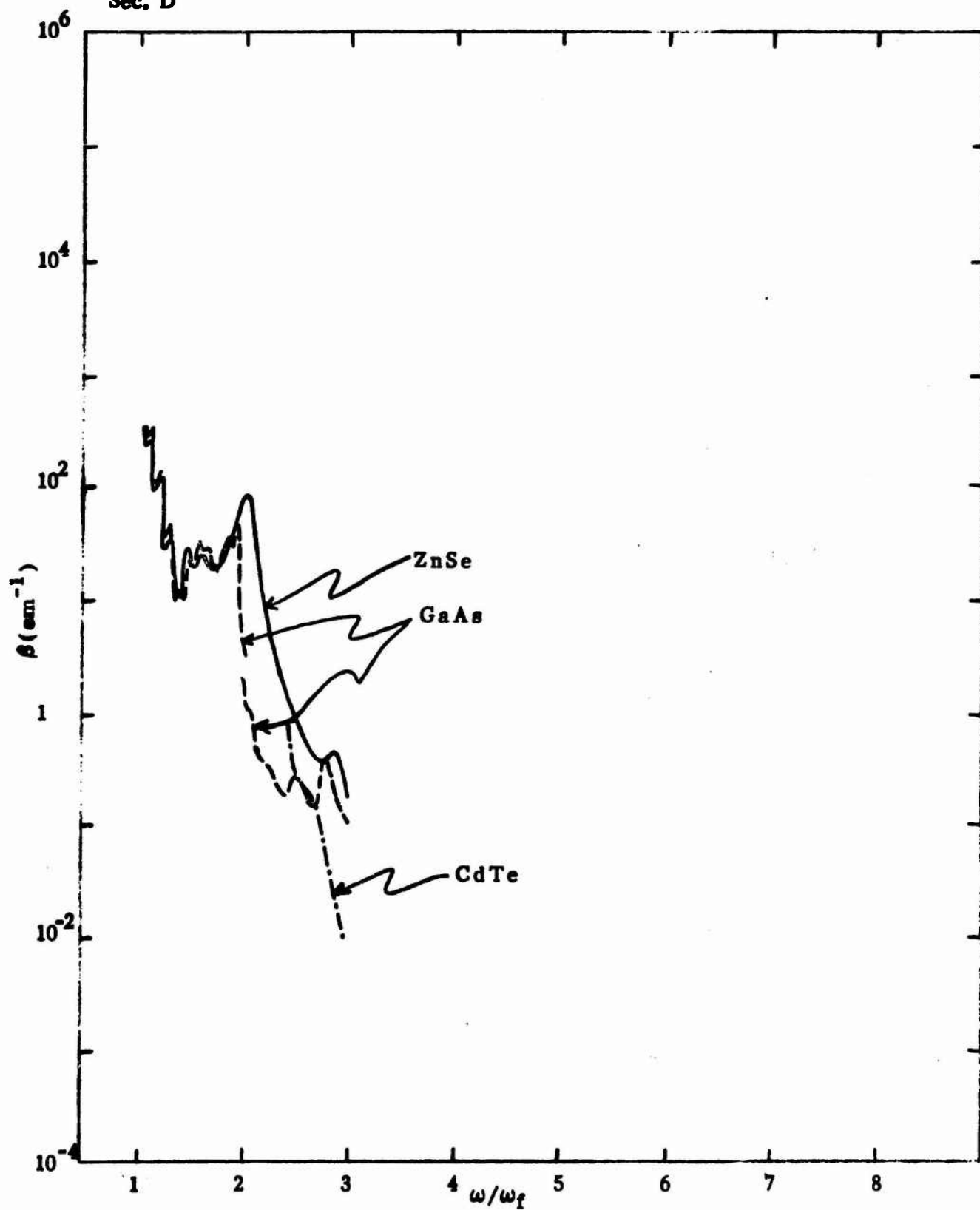


Fig. 20. Comparison of the absorption of zincblende structure semiconductors from the curves in Figs. 8-10.

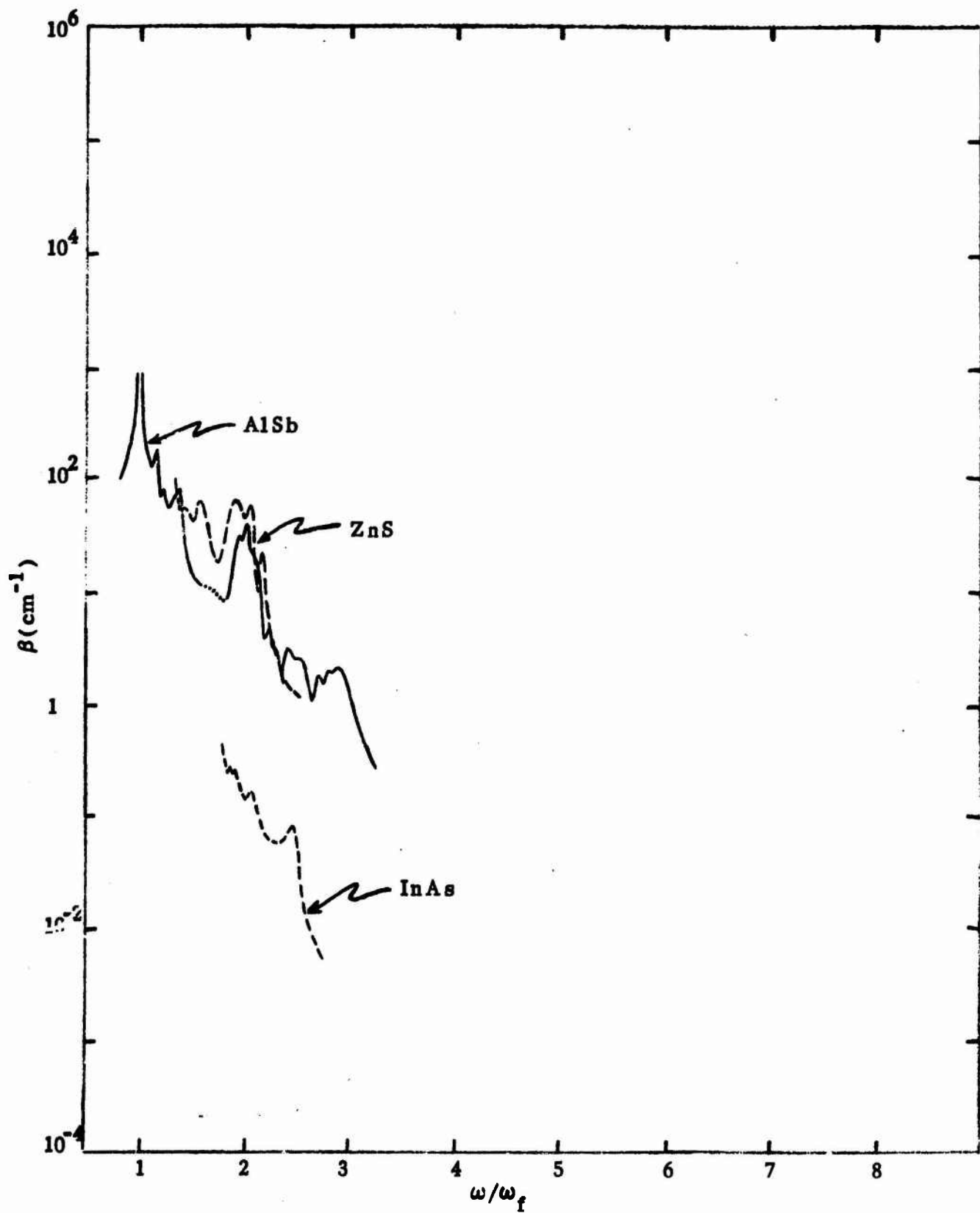


Fig. 21. Comparison of the absorption of zincblende structure semiconductors from the curves in Figs. 11-13.

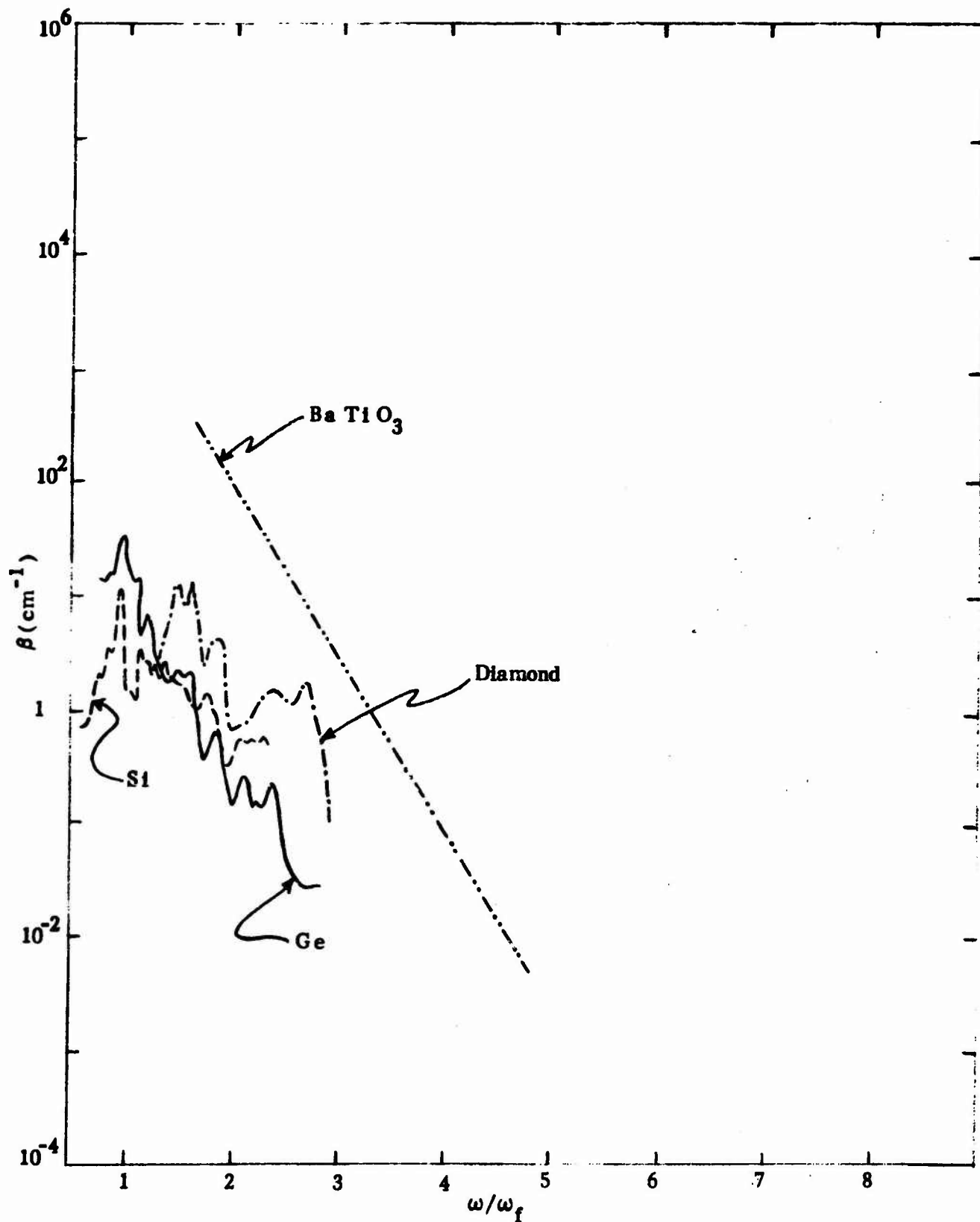


Fig. 22. Comparison of the absorption of type IV elemental semiconductors, from the curves in Figs. 14-17.

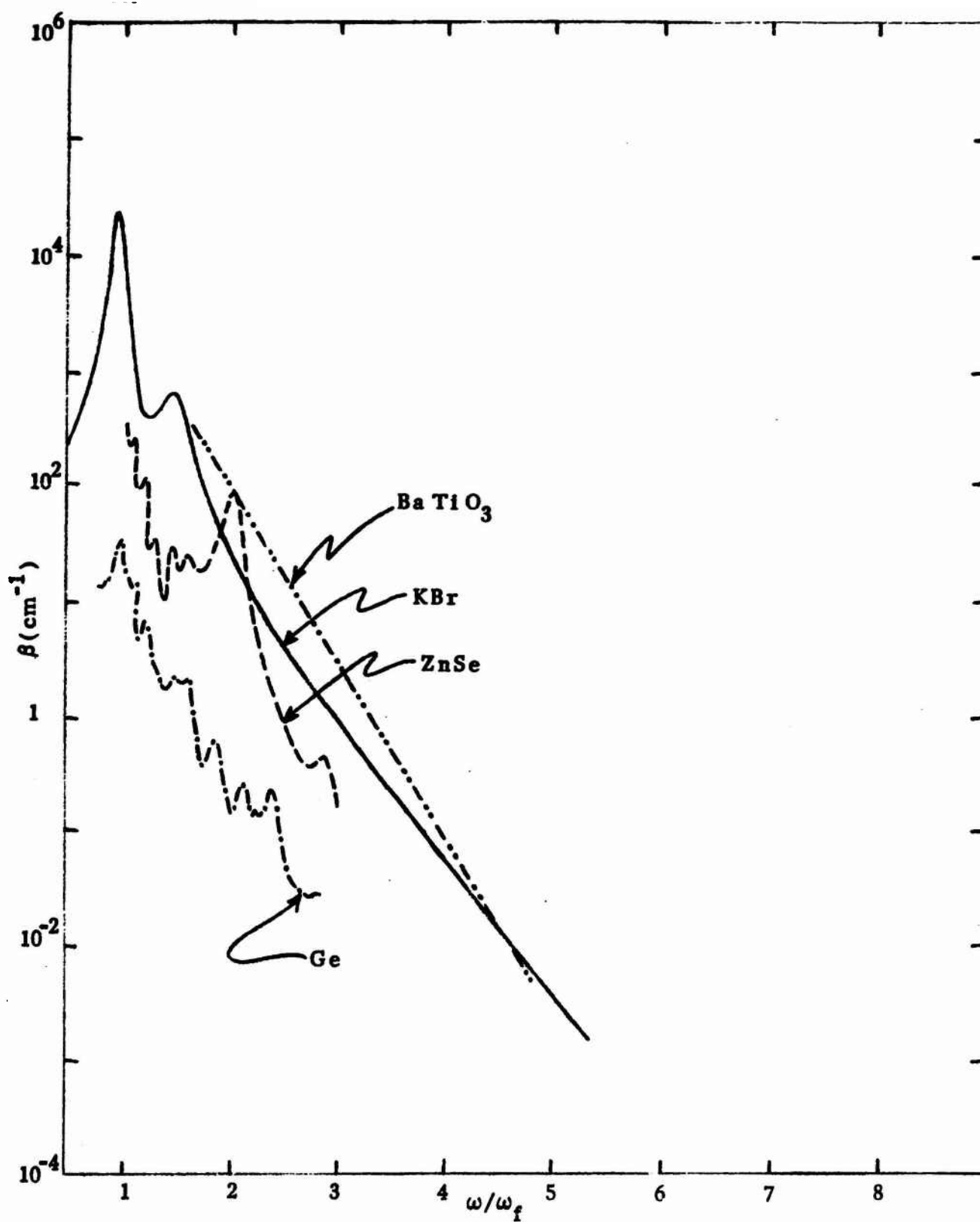


Fig. 23. Comparison of the absorption of one material from each group represented in Figs. 18-22.

E. REFERENCES TO PREVIOUS MULTIPHONON CALCULATIONS

The following references to multiphonon calculations are representative of the literature, but are not intended to be exhaustive. All of these references are concerned with the two-phonon region, with straightforward numerical analyses, or with formulations without numerical results.

1. R. B. Barnes, R. R. Brattain, and F. Seitz, "On the Structure and Interpretation of the Infrared Absorption Spectra of Crystals," *Phys. Rev.* 48, 582 (1935).
2. B. Bendow, "Correlation Function Theory of Multiphonon Absorption in Laser Window Materials," Conference on High-Power Infrared Laser Window Materials, Hyannis, Massachusetts, October 1972 (Proceedings to be published by Air Force Cambridge Research Laboratories).
3. E. Burstein, J. J. Oberly, and E. K. Plyler, "The Infrared Properties of Magnesium Oxide and Their Interpretation," *Proc. Indian Acad. Sci.* 28, 388 (1948).
4. E. R. Cowley, "Anharmonic Contributions to the Thermodynamic Properties of Sodium Chloride," *J. Phys. C: Solid St. Phys.* 4, 988 (1971).
5. E. R. Cowley, "The One-Phonon Green's Function and Dielectric Properties of Sodium Chloride," *J. Phys. C: Solid St. Phys.* 5, 1345 (1972).
6. E. R. Cowley and R. A. Cowley, "Anharmonic Interactions in Alkali Halides. I," *Proc. Roy. Soc. (London) A* 287, 259 (1965).
7. E. R. Cowley and R. A. Cowley, "Anharmonic Interactions in Alkali Halides. II," *Proc. Roy. Soc. (London) A* 292, 209 (1966).
8. P. Denham, G. R. Field, P. L. R. Morse, and G. R. Wilkinson, "Optical and Dielectric Properties and Lattice Dynamics of Some Fluorite Structure Ionic Crystals," *Proc. Roy. Soc. (London) A* 317, 55 (1970).

9. D. A. Kleinman, "Anharmonic Forces in the GaP Crystal," *Phys. Rev.* 118, 118 (1960).
10. M. Lax, "Quantum Relaxation, the Shape of Lattice Absorption and Inelastic Neutron Scattering Lines," *J. Phys. Chem. Solids* 25, 487 (1964).
11. M. Lax and E. Burstein, *Phys. Rev.* 97, 39 (1955).
12. R. Loudon, "General Space-Group Selection Rules for Two-Phonon Processes," *Phys. Rev.* 137, A 1784 (1965).
13. M. Mangir and R. Hellwarth, "Theory of Infrared Absorption by Crystals in the High Frequency Wing of Their Fundamental Lattice Absorption," *Bull. Am. Phys. Soc.* (1972).
14. A. A. Maradudin, E. W. Montroll, G. H. Weiss, and I. P. Ipatova, Theory of Lattice Dynamics in the Harmonic Approximation, Second Edition, Academic Press, New York (1971).
15. A. A. Maradudin and R. F. Wallis, "Lattice Anharmonicity and Optical Absorption in Polar Crystals: I. The Linear Chain," *Phys. Rev.* 120, 442 (1960).
16. S. S. Mitra, "Review of Absorption Mechanisms," Conference on High-Power Infrared Laser Window Materials, Hyannis, Massachusetts, October 1972 (Proceedings to be published by Air Force Cambridge Research Laboratories).
17. V. V. Mitskevich, "Dynamical Theory of NaCl-Type Ionic Crystals. II. Dielectric and Optical Properties," *Sov. Phys. - Solid State* 3, 2211 (1962).
18. V. V. Mitskevich, "Infrared Absorption and Dispersion in LiF and MgO," *Sov. Phys. - Solid State* 4, 2224 (1963).
19. G. Rupprecht, *Phys. Rev. Letters* 12, 1580 (1964).

20. B. Szigeti, "Polarisability and Dielectric Constant of Ionic Crystals,"
Trans. Faraday Soc. 45, 155 (1949).
21. B. Szigeti, "Compressibility and Absorption Frequency of Ionic Crystals,"
Proc. Roy. Soc. (London) A204, 51 (1950).
22. B. Szigeti, "Higher-Order Terms in the Dielectric Constant of Ionic
Crystals," Proc. Roy. Soc. (London) A252, 217 (1959).
23. B. Szigeti, "The Infra-Red Spectra of Crystals," Proc. Roy. Soc. (London)
A258, 377 (1960).
24. B. Szigeti, "Impurity Activated Infra-Red Absorption in Valency Crystals,"
J. Phys. Chem. Solids 24, 225 (1963).
25. V. S. Vinogradov, "Application of Green's Functions to the Calculations of
Infrared Adsorption in Ionic Crystals," Sov. Phys. - Solid State 4, 519 (1962).
26. L. A. Vredevoe, "Third-Order Anharmonic Interactions of Infrared Phonons
in the Alkali Halides," Phys. Rev. 140, A 930 (1965).

REFERENCES

In addition to the numbered references below, see the list of references to multiphonon calculations given in Sec. E and the list of publications and conference presentations prepared under the present contract (Sec. A).

1. M. Sparks and T. Azzarelli, "Theoretical Studies of High-Power Infrared Window Materials," Xonics, Inc. Quarterly Technical Progress Report No. 1, Contract DAHC15-72-C-0129.
2. F. A. Horrigan and T. F. Deutsch, "Research in Optical Materials and Structures for High-Power Lasers," Raytheon Research Division, Quarterly Technical Reports Nos. 1 and 2, Contract DA-AH01-72-C-0194, January and April 1972.
3. M. Sparks and T. Azzarelli, "Theoretical Studies of High-Power Infrared Window Materials," Xonics, Inc. Quarterly Technical Progress Report No. 2, Contract DAHC15-72-C-0129.
- 3a. Recent reviews of infrared absorption include: E. Burstein, Lattice Dynamics, Proc. Intl. Conference, Copenhagen, August 1963, Ed. R. F. Wallis (Pergamon Press, Inc.), p. 315; R. A. Cowley, Phonons in Perfect Lattices, Ed. R. W. H. Stevenson (Oliver and Boyd, Edinburgh and London, 1966); A. A. Maradudin, E. W. Montroll, G. H. Weiss, and I. P. Ipatova, Theory of Lattice Dynamics in the Harmonic Approximation, 2nd ed. (Academic Press, New York, 1971); D. H. Martin, Adv. Phys. 14, 39 (1965); W. G. Spitzer, Semiconductors and Semimetals, Optical Properties of III-V Compounds (1967). Also see Appendix A of Ref. 1.
4. G. Rupprecht, Phys. Rev. Letters 12, 580 (1964).
5. W. Kaiser, W. G. Spitzer, R. H. Kaiser, and L. E. Howarth, Phys. Rev. 127, 1950 (1962); P. Denham, G. R. Field, P. L. R. Morse, and G. R. Wilkinson, Proc. Roy. Soc. London A317, 55 (1970).
6. R. A. Cowley, Phonons in Perfect Lattices, Ed. R. W. H. Stevenson (Oliver and Boyd, Edinburgh and London, 1966). See Eq. (5.12), p. 192.
7. M. Lax and E. Burstein, Phys. Rev. 97, 39 (1955); M. Born, Rev. Mod. Phys. 17, 245 (1945).
8. M. Sparks, Ferromagnetic-Relaxation Theory, McGraw-Hill Book Co., New York (1964).
9. A. A. Maradudin, E. W. Montroll, G. H. Weiss, and I. P. Ipatova, Theory of Lattice Dynamics in the Harmonic Approximation, 2nd ed., Academic Press, New York (1971).

10. C. Kittel, Introduction to Solid State Physics, 4th ed., John Wiley and Sons, Inc., New York (1971).
11. R. Loudon, Phys. Rev. 137 A, 1784 (1965).
12. G. Raunio and S. Rolandson, Phys. Rev. B2, 2098 (1970).
13. A. Papoulis, Probability, Random Variables, and Stochastic Processes, McGraw-Hill Book Co., New York (1965).
14. A. M. Karo and J. R. Hardy, "Lattice Dynamics of Rocksalt-Structure Alkali Halides: Eigenvectors and Eigenfrequencies," University of California Lawrence Radiation Laboratory Report, AEC Contract No. W-7405-eng-48, April 1966.
- 14a. B. Szigeti, Lattice Dynamics, Proc. Intl. Conference, Copenhagen, August 1963, Ed. R. F. Wallis, Pergamon Press, Inc. (1965), p. 405.
15. M. Mangir and R. Hellwarth, "Theory of Infrared Absorption by Crystals in the High Frequency Wing of Their Fundamental Lattice Absorption," Bull. Am. Phys. Soc. 17, 1190 (1972).
16. B. Bendow, "Correlation Function Theory of Multiphonon Absorption in Laser Window Materials," Conference on High-Power Infrared Laser Window Materials, Hyannis, Massachusetts, October 1972 (Proceedings to be published by Air Force Cambridge Research Laboratories).
17. S. S. Mitra, "Review of Absorption Mechanisms," Conference on High-Power Infrared Laser Window Materials, Hyannis, Massachusetts, October 1972 (Proceedings to be published by Air Force Cambridge Research Laboratories).
- 17a. See references in Sec. A, p. 6.
18. M. Sparks, J. Appl. Phys. 42, 5029 (1971).
19. M. Sparks, "Optical Distortion by Heated Windows in High-Power Laser Systems," Rand Corporation Report No. R-545-PR, September 1971.
20. M. Sparks, "Physical Principles, Materials Guidelines, and Materials List for High-Power 10.6 μ Windows," Rand Corporation Report No. R-863-PR, August 1971.
21. H. V. Winsor, Air Force Weapons Laboratory, Kirtland Air Force Base, private communication (1970).
22. C. S. Sahagian and C. A. Pitha, Ed., Conference on High-Power Infrared Laser Window Materials, Air Force Cambridge Research Laboratories (1971); C. A. Pitha, Ed., Conference on High-Power Infrared Laser Window Materials, Air Force Cambridge Research Laboratories (1972).

23. G. Mie, *Ann. Physik* 25, 377 (1908).
24. H. C. Van de Hulst, *Light Scattering by Small Particles*, John Wiley and Sons, Inc., New York (1957).
25. For the case of $\Im m \epsilon \gg 1$, as for metals at infrared frequencies, the region of validity of using the single term a_1 is $ka \Im m \epsilon \ll 10$. See p. 290 of Ref. 24.
- 25a. J. A. Stratton, *Electromagnetic Theory*, McGraw Hill Book Co., Inc., New York (1941), p. 570.
26. W. Franz and K. Deppermann, *Ann. Physik* 10, 361 (1952).
27. K. Depperman and W. Franz, *Ann. Physik* 14, 253 (1954).
28. V. A. Fock, *J. Phys. USSR* 10, 130 (1946).
29. H. Siedentopf, *Z. Physik* 6, 855 (1905).
30. A. B. Scott, W. A. Smit, and M. A. Thompson, *J. Phys. Chem.* 57, 757 (1953).
31. W. T. Doyle, *Proc. Phys. Soc. (London)* 75, 649 (1960).
32. M. Sparks, "Stress and Temperature Analysis for Surface Cooling or Heating of Laser Window Materials," Parke Mathematical Laboratories Report No. 0142-TM-1, July 1971.
33. M. Sparks, "Temperature and Stress Analysis for Bulk- and Surface-Heated Slabs," Parke Mathematical Laboratories Report No. TM-2, August 1971.
34. M. Sparks, "Calculated Temperature Distributions in Slabs Heated in a Thin Surface Layer," Parke Mathematical Laboratories Report No. TM-3, September 1971.
35. J. D. Jackson, *Classical Electrodynamics*, John Wiley and Sons, Inc., New York (1962).
36. H. S. Carslaw and J. C. Jaeger, *Conduction of Heat in Solids*, 2nd ed., Oxford Clarendon Press, London (1959).
37. R. W. Hopper and D. R. Uhlmann, *J. Appl. Phys.* 41, 4023 (1970).
38. N. Bloembergen, to be published.
39. F. A. Horrigan and T. F. Deutsch, "Research in Optical Materials and Structures for High-Power Lasers," Raytheon Research Division, Final Technical Report, Contract DA-AH01-70-C-1251, September 1971.

40. L. Genzel, Fest Korper Probleme 9, 32 (1969).
41. C. Smart, G. R. Wilkinson, A. M. Karo, and J. R. Hardy, Lattice Dynamics, Proc. Intl. Conference, Copenhagen, August 1963, Ed. R. F. Wallis (Pergamon Press, Inc., 1965) p. 387.
42. P. Denham, G. R. Field, P. L. R. Morse, and G. R. Wilkinson, Proc. Roy. Soc. (London) A 317, 55 (1970).
43. F. A. Horrigan and T. F. Deutsch, "Research in Optical Materials and Structures for High-Power Lasers," Raytheon Research Division, Quarterly Technical Report No. 3, Contract DA-AH01-72-C-0194, July 1972.
44. F. A. Johnson, Progress in Semiconductors 9, 181 (1965).
45. W. J. Turner and W. E. Reese, Phys. Rev. 127, 126 (1962).
46. T. Deutsch, Proceedings of International Conference Physics of Semiconductors, Exeter, July 1962 (Inst. of Physics and Physical Society, 1962), p. 505